LA--12487-T

DE93 010255

A Study of Isospin Symmetry Breaking in Carbon 12 with 50 MeV Pions

*Joffa Michele Applegate**

**Guest scientist at Los Alamos Group MP-10.*
Department of Physics and Astronomy, Arizona State University, Tempe, AZ 85287-1504

Los Alamos
NATIONAL LABORATORY
Los Alamos, New Mexico 87545

ACKNOWLEDGMENTS

I would like to thank my advisor, Professor Barry Ritchie, for his support and understanding during my graduate career. He has been an excellent advisor and set a standard through his expectations that I was proud to work toward. I would also like to thank Dr. Chris Morris at LAMPF for all the time, support and advice he has given me in regards to this project.

I am indebted to Mr. Jim Beck for his invaluable help in the data analysis process, and to Mr. Doug Smith for his time and patience in furthering my understanding of the fitting routine.

I also gratefully acknowledge the assistance of Mr. Todd Averett, Mr. Chris Kormanyos, Mr. Byron McCloud, Dr. John McGill, Professor Fred Moore, Dr. John O'Donnell, Professor David Oakley, Mr. Herb Ward and Mr. Charles Whitley during the data taking phase of the experiment, and Mr. Aaron Vanderpool during the final stages of data analysis.

Professor Jerry Peterson and Mrs. Romell Ritchie put both time and professional expertise into the preparation of this manuscript that are greatly appreciated.

Finally, I would like to thank my committee members, past and present, for their support and advice: Professor Raghunath Acharya, Professor Ricardo Alarcon and Professor Bill Kaufmann.

Table of Contents

List of Tables

List of Figures

A STUDY OF ISOSPIN SYMMETRY BREAKING IN CARBON 12

WITH 50 MeV PIONS

by

Joffa Michele Applegate

ABSTRACT

In the first experiment to use the superconducting RF cavity at LAMPF known as the Scruncher, cross sections have been measured for the 1+ doublet in ^{12}C by 50 MeV $\pi^{\pm}$ scattering. The cross section ratio of the isoscalar to the isovector states was found to be 6.8 ± 1.3 for π^+ scattering and 3.9 ± 1.4 for π^- scattering. These ratios give an isospin mixing matrix element $\mathcal{H}_{01}$ of 119 ± 40 keV, in good agreement with the average value of 123 ± 26 keV deduced from previous pion-scattering data and with values deduced from other probes. The ratio of $\pi^+ + p$ to $\pi^- + p$ cross sections was determined experimentally to be 2.60 ± 0.11, in agreement with a theoretical value of 2.85. The agreement of these results indicates that the impulse approximation is valid at 50 MeV. Cross sections were also measured for the elastic and collective states in ^{12}C and were generally described well by distorted wave Born approximation calculations published previously.

Chapter 1

Introduction

One of the primary goals of meson production facilities such as LAMPF is to provide data to further the understanding of the pion-nucleus interaction, including the isospin-dependent components. Since isospin symmetry is conserved by the strong force, isospin T should be a good quantum number and nuclear states should be of nearly pure isospin. However, several experiments have demonstrated varying amounts of isospin symmetry breaking in nuclear states. It is the isospin dependence in the nuclear Hamiltonian that leads to this symmetry breaking. We will call this isospin dependent piece $\mathcal{H}_{01}$.

Pions exist in three isospin states and are thus useful in isospin studies. "Low energy" pions have energies below the Δ-resonance region where the $p_{3,3}$ partial wave dominates the interaction, as seen in Figure 1.1. These pions have a longer mean free path inside nuclear matter, as seen in Figure 1.2, which suggests they can probe deeper into the nucleus than pions with higher energies. This allows exploration of the nuclear interior, including the nuclear wave functions and transition densities.

Low energy pion experiments are complicated by the short lifetimes of the pions (26 ns). Consequently, any experimental apparatus for such experiments needs to have short path lengths for the pions to travel, and longer running times are generally necessary to accumulate amounts of data comparable to those of higher energy experiments. Because of the lack of low energy spectrometers with good energy resolution until recently (circa 1984, with the advent of the Clamshell spectrometer at LAMPF), experimental data for nuclear interactions involving pions with energies

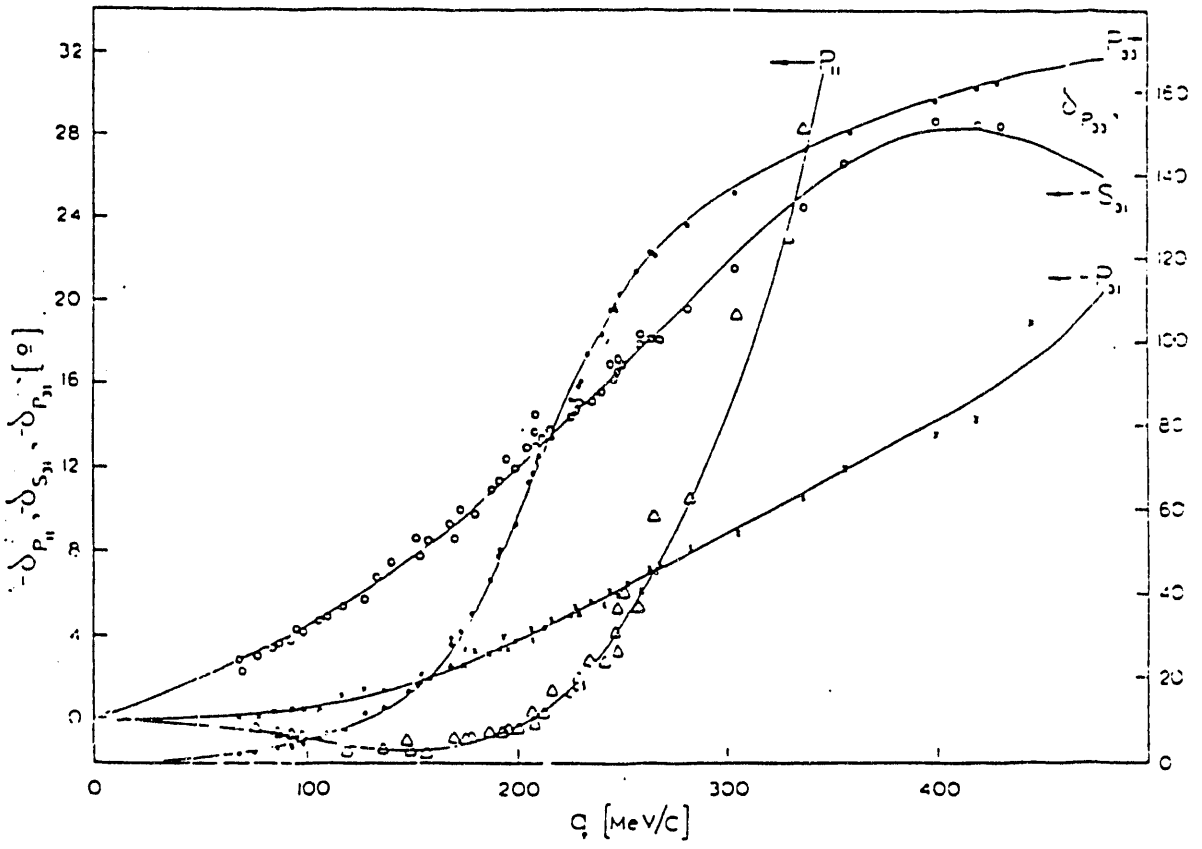

Figure 1.1: $S_{3,1}, P_{1,1}, P_{3,1}$ and $P_{3,3}$ pion-nucleon phase shifts given in degrees [Row 78]. Note the arrows giving the correct energy scale. The $p_{3,3}$ wave begins to dominate at about 100 MeV/c.

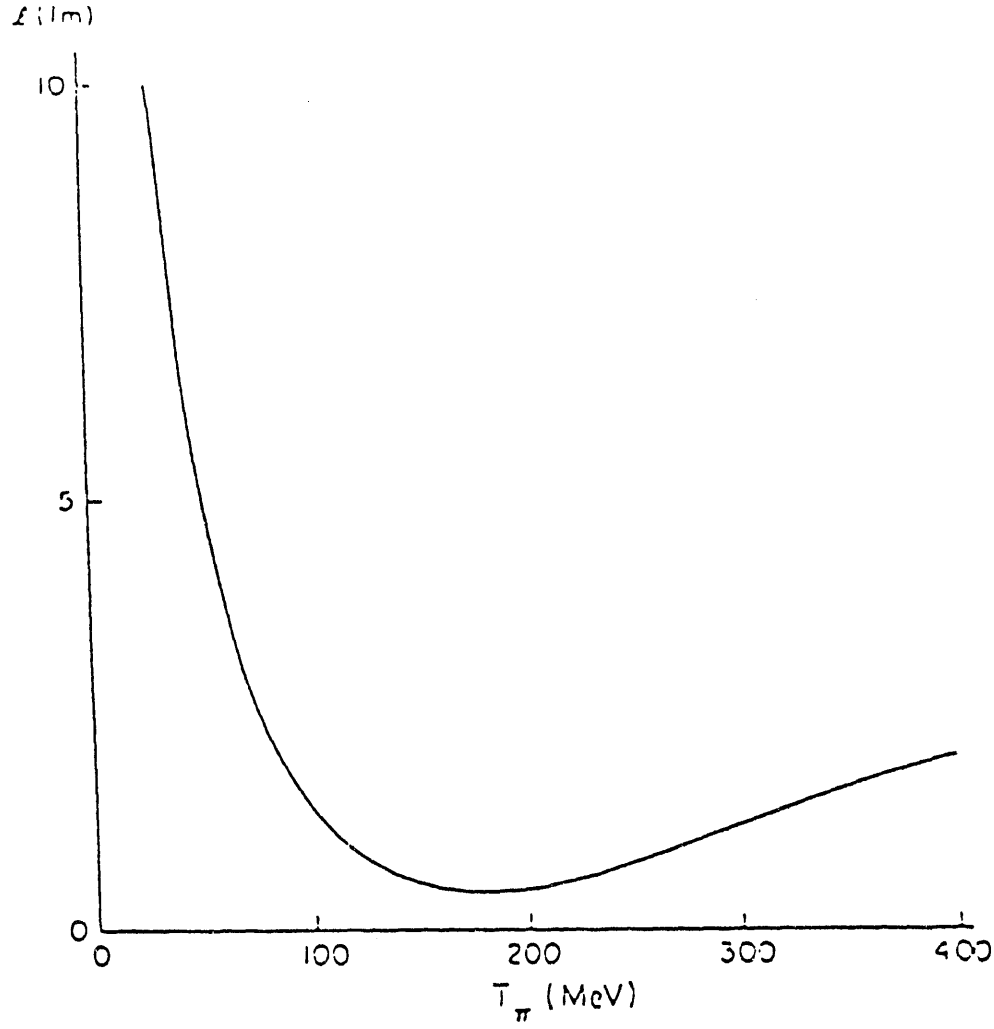

Figure 1.2: The mean free path of pions in nuclear matter, $\rho_o = .17$ fm^{-3}, as a function of energy [Eis 80]. The diameter of the ^{12}C nucleus is about 5 fm [DeV 87].

below 100 MeV are relatively scarce. Experiments conducted prior to 1984 were principally concerned with elastic scattering or isoscalar collective excitations.

^{12}C has been studied well at resonance energies with pions and other probes and has a well-known spectroscopy. The collective excitations of this particular nucleus are explained well by collective transition densities and other transitions by many models including particle-hole descriptions. The latter approach provides a theoretical basis in this work for an expression of the isospin mixing Hamiltonian.

For this work the two states in ^{12}C of interest occur at excitation energies of 12.71 MeV and 15.11 MeV; these states are dominantly $T = 0$ and $T = 1$, respectively, as shown in Figure 1.3. Using ratios of the cross sections for π^+ and π^- scattering to these two states, a two-state formalism is developed that yields the isospin mixing component of the nuclear Hamiltonian, H_{CD}. The ground state wavefunction is assumed to be filled neutron and proton $p_{3/2}$ shells. The impulse approximation, where we are considering only the effect of interactions with one nucleon, is implicit; the dominant wavefunction for the 1^+ doublet is represented by the spin-flip of a $p_{3/2}$ nucleon.

Data were obtained for laboratory angles of $30°, 45°, 60°, 75°, 90°$ and $103°$ with a 50 MeV π^+ incident beam, and for laboratory angles of $60°, 90°$ and $103°$ with a 50 MeV π^- incident beam. Values for the cross sections were determined by fitting the experimental spectra and obtaining areas under the excitation peaks. These areas were then included in an expression for the cross section including many correction factors and a normalization to previous data, as detailed in Chapter 4. Using these cross sections and the two-state formalism, values were obtained numerically for the isospin mixed state wavefunction amplitudes, α and β, in terms of the pure isospin basis. The isospin mixing matrix element, $\mathcal{H}_{01}$, was then calculated as a function of these parameters.

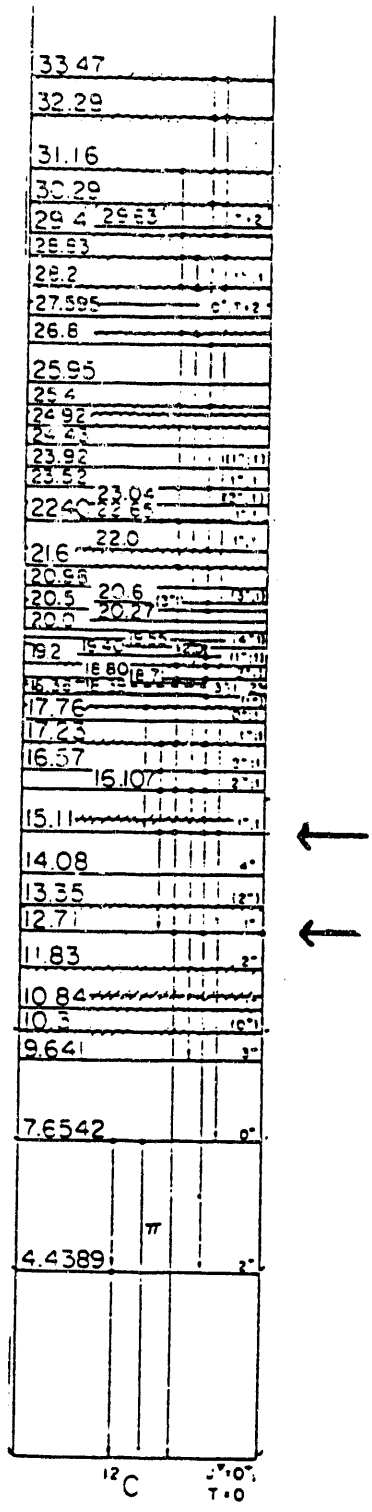

Figure 1.3: ^{12}C level scheme [Ajz 85]. Note the 1^+ doublet at energies 12.71 MeV and 15.11 MeV, which are of primary interest in this work.

Previous pion-scattering experiments conducted at 50 MeV and reported by Jaki *et al.* [Jak 90], Morris *et al.* [Mor 81] and Ritchie *et al.* [Rit 90] disagree on the value of $\mathcal{H}_{01}$, with experimental values ranging from 25 keV [Rit 90] to 157 keV [Jak 90]. The ratio of the $T = 0$ to $T = 1$ cross sections R is also of importance. Using isospin impulse approximation arguments explained in Chapter 2, the theoretical value of R at resonance energies will be seen to be 4. Previous experimentally determined values of R have been found to be about 1. The purpose of this experiment was to provide more data in order to determine the value $\mathcal{H}_{01}$ and the validity of the impulse approximation.

Chapter 2

Theory

2.1 Introduction

In this chapter, pertinent theoretical aspects of pion-nucleon scattering and the resulting isospin states will be discussed using the impulse approximation. The formalism for finding the isospin mixing matrix element $\mathcal{H}_{01}$ and the ratios of cross sections will also be discussed in detail.

2.2 Scattering of Pions with Nuclei

An incoming beam of pions can be represented as a plane wave of momentum $\hbar k$ traveling parallel to the z-axis. When this beam is scattered from a nucleus, the interaction potential between the pions and the nucleons creates scattered secondary spherical waves which interfere with the pion plane waves. The wave function of the elastically scattered beam of particles in the center of mass system is a superposition of the incident plane wave with the scattered spherical waves, given by

$$\Psi(r,\theta,\phi) = [e^{ikz} + \mathcal{F}(\theta,\phi,k)\frac{e^{ikr}}{r}]\chi,$$

where $\mathcal{F}(\theta,\phi,k)$ is the scattering amplitude and χ is the spin function of the nucleus. The differential cross section $d\sigma/d\Omega$ is a measure of the probability that particles will be scattered into a solid angle $d\Omega$. $d\sigma/d\Omega$ can be expressed in terms of $\mid \mathcal{F}(\theta,\phi,k) \mid^2$, which is averaged over initial spin states and summed over final spin states.

The 1^+ states can be modeled as single particle transitions, so pion-nucleon scattering is of primary interest. By using the impulse approximation, we now consider pion-nucleon scattering instead of pion-nucleus scattering. Since total angular momentum J, orbital angular momentum ℓ, and isospin T are all conserved, the scattering amplitude $\mathcal{F}$ can be written in terms of eigenfunctions of angular momentum, and expressed in partial waves [Kol 71]:

$$\mathcal{F}(\theta,\phi,k) = \frac{1}{k}\sum_{\ell,J,T}(2\ell+1)[a_{2T,2\ell-1}\Delta_{\ell,\ell-\frac{1}{2}} + a_{2T,2\ell+1}\Delta_{\ell,\ell+\frac{1}{2}}]P_\ell(\cos\theta).$$

$\Delta_{\ell,J}$ is the spin projection operator involving the Pauli spin vector σ, and for spin $\frac{1}{2}$ is given by:

$$\Delta_{\ell,\ell+\frac{1}{2}} = \frac{\ell+1+\sigma\cdot\mathbf{L}}{2\ell+1}$$

and

$$\Delta_{\ell,\ell-\frac{1}{2}} = \frac{\ell-\sigma\cdot\mathbf{L}}{2\ell+1}.$$

$a_{2T,2J}$ is a function of the phase shift, $\delta_{T,J}$, and is expressed as $a_{2T,2J} = e^{i\delta_{T,J}}\sin\delta_{T,J}$, and $P_\ell(\cos\theta)$ are the Legendre polynomials. Now [Gas 66]

$$\sigma\cdot\mathbf{L}P_\ell(\cos\theta) = i\sigma\cdot\hat{\mathbf{n}}P'_\ell(\cos\theta)\sin\theta,$$

where $\hat{\mathbf{n}}$ is the unit vector normal to the scattering plane, so $\mathcal{F}$ becomes

$$\begin{aligned}\mathcal{F}(\theta,\phi,k) = \frac{1}{k}\sum_{\ell,J,T}&[[\ell a_{2T,2\ell-1} + (\ell+1)a_{2T,2\ell+1}]P_\ell(\cos\theta)\\ &-i\sigma\cdot\hat{\mathbf{n}}[a_{2T,2\ell-1} - a_{2T,2\ell+1}]P'_\ell(\cos\theta)\sin\theta].\end{aligned}$$

This can be rewritten as a function of two scattering amplitudes,

$$\mathcal{F}(\theta,\phi,k) = f(\theta,k) - i\sigma\cdot\hat{\mathbf{n}}g(\theta,k),$$

where $f(\theta,k)$ is the non-spin-flip amplitude and $g(\theta,k)$ is the spin-flip amplitude.

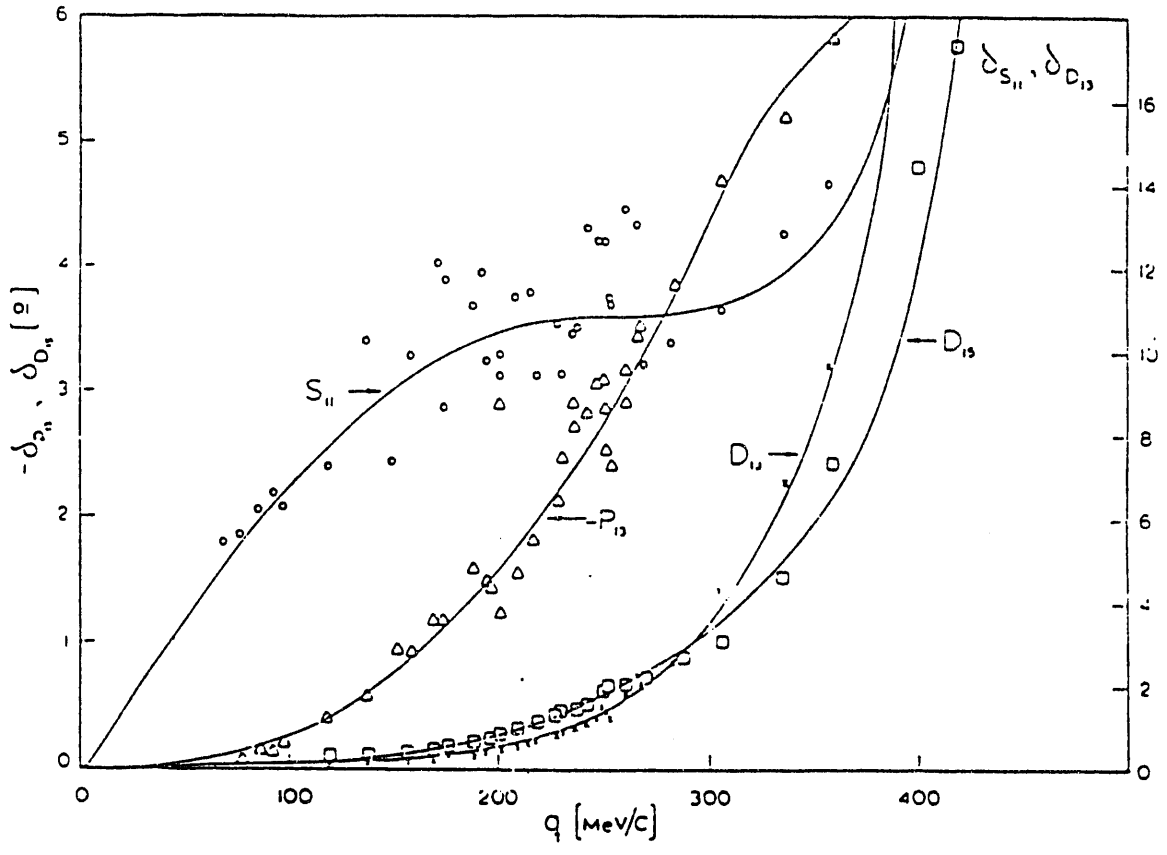

Figure 2.1: $S_{1,1}, P_{1,1}, D_{1,3}$ and $D_{1,5}$ pion-nucleon phase shifts given in degrees [Row 78]. Note the arrows giving the appropriate scale. At low energies the d waves are negligible compared to the s and p waves.

As apparent from Figures 1.1 and 2.1, at low energies the phase shifts for scattered d waves are negligible compared with those of scattered s and p waves. Considering only these s ($\ell = 0$) and p ($\ell = 1$) waves, and assuming that the s wave does not undergo a spin-flip transition, the two scattering amplitudes can be written as:

$$f(\theta, k) = \frac{1}{k}[a_{2T,1} + (a_{2T,1} + 2a_{2T,3})\cos\theta]$$

and

$$g(\theta, k) = \frac{1}{k}(a_{2T,1} - a_{2T,3})\sin\theta.$$

In terms of our partial wave amplitudes f and g, the differential cross section for unpolarized scattering is:

$$\frac{d\sigma}{d\Omega} = \mid f(\theta, k) \mid^2 + \mid g(\theta, k) \mid^2.$$

2.3 Pion-Nucleon Isospin States

The Coulomb force depends on the charge of the interacting particles and has infinite range, in comparison to the strong force which has a very short interaction range (on the order of 1 fm) and is independent of the charge of the interacting particles. The strong force, the dominant force in nuclear interactions, is generally assumed to be charge symmetric. Since protons and neutrons are thus seen as identical particles, called nucleons, by the strong force, a nucleon can be considered to be in a proton state or a neutron state. Isospin is the quantum number assigned to particles to differentiate between charge states and is expressed in terms of total isospin T and the isospin projection T_3. Table 2.1 gives some useful information about nucleons, pions and Δ-particles.

In this thesis, an isospin state is denoted as $\mid T, T_3\rangle$, and protons have isospin "up," $\mid \frac{1}{2}, +\frac{1}{2}\rangle$, and neutrons have isospin "down," $\mid \frac{1}{2}, -\frac{1}{2}\rangle$.

particle		mass (MeV)	lifetime (s)	charge (e)	spin	isospin T_z
nucleons	proton	938.272	∞	+1	$\frac{1}{2}$	$+\frac{1}{2}$
(T=$\frac{1}{2}$)	neutron	939.566	889.1	0	$\frac{1}{2}$	$-\frac{1}{2}$
pion	π^+	139.568	2.60×10^{-8}	+1	0	+1
(T=1)	π^o	134.974	8.4×10^{-17}	0	0	0
	π^-	139.568	2.60×10^{-8}	-1	0	-1
delta	Δ^{++}	1230.9	6.0×10^{-24}	+2	$\frac{3}{2}$	$+\frac{3}{2}$
(T=$\frac{3}{2}$)	Δ^+	1234.9	6.0×10^{-24}	+1	$\frac{3}{2}$	$+\frac{1}{2}$
	Δ^o	1233.6	6.0×10^{-24}	0	$\frac{3}{2}$	$-\frac{1}{2}$
	Δ^-	1234.9	6.0×10^{-24}	-1	$\frac{3}{2}$	$-\frac{3}{2}$

Table 2.1: Some useful quantities for nucleons, pions and Δ-particles [Hik 92].

Since pions occur in three charge states, pions have isospin $T = 1$. The three pion states are denoted as $\pi^+ = \mid 1, +1\rangle$, $\pi^o = \mid 1, 0\rangle$, and $\pi^- = \mid 1, -1\rangle$. An interacting system of a pion and a nucleon can combine to yield total isospin states of $T = \frac{3}{2}$ (parallel) and $T = \frac{1}{2}$ (antiparallel).

The pion-nucleon elastic scattering interactions are:

a. $\pi^+ + p \longrightarrow \pi^+ + p$,

b. $\pi^- + p \longrightarrow \pi^- + p$,

c. $\pi^+ + n \longrightarrow \pi^+ + n$ and

d. $\pi^- + n \longrightarrow \pi^- + n$.

Other reactions involve charge exchange, such as $\pi^- + p \longrightarrow \pi^o + n$.

The isospin mixing coefficients for the elastic scattering interactions are determined from the angular momentum coupling rules with the resulting Clebsch-Gordan coefficients. Using Table 2.2(a), we find the following combinations for the final state wavefunctions for the above reactions:

a. $\mid \frac{3}{2}, \frac{3}{2}\rangle$,

b. $\sqrt{\frac{1}{3}} \mid \frac{3}{2}, -\frac{1}{2}\rangle - \sqrt{\frac{2}{3}} \mid \frac{1}{2}, -\frac{1}{2}\rangle$,

a) $1 \times 1/2$

	3/2	
	-3/2	
-1 -1/2	1	

3/2	1/2	
-1/2	-1/2	

-1 -1/2	1/3	2/3
0 -1/2	2/3	-1/3

3/2	1/2	
-1/2	-1/2	

0 -1/2	2/3	1/3
-1 +1/2	1/3	-2/3

3/2		
-3/2		

-1 -1/2	1

b) $1/2 \times 1/2$

1	
+1	
+1/2 -1/2	1

1	0	
0	0	

-1/2 +1/2	1/2	1/2
-1/2 -1/2	1/2	-1/2

1	
-1	

-1/2 -1/2	1

Note: A $\sqrt{\ }$ is to be understood over every coefficient:

Notation:	j j ...
	M M ...
m_1 m_2	Coefficients
m_1 m_2	
. .	
. .	

Table 2.2: Clebsch-Gordan tables for coupling (a) a $T = 1$ particle with a $T = 1/2$ particle, and (b) a $T = 1/2$ particle with another $T = 1/2$ particle [Hik 92].

c. $\sqrt{\frac{1}{3}} \mid \frac{3}{2}, \frac{1}{2}\rangle + \sqrt{\frac{2}{3}} \mid \frac{1}{2}, \frac{1}{2}\rangle$ and

d. $\mid \frac{3}{2}, -\frac{3}{2}\rangle$.

In terms of the isospin amplitudes $\mathcal{M}_3$ and $\mathcal{M}_1$ for $T = \frac{3}{2}$ and $T = \frac{1}{2}$, the amplitudes for pion-nucleon elastic scattering interactions can be written as:

$$\mathcal{M}_a = \mathcal{M}_d = \mathcal{M}_3$$

and

$$\mathcal{M}_b = \mathcal{M}_c = \frac{1}{3}\mathcal{M}_3 + \frac{2}{3}\mathcal{M}_1.$$

The cross section σ is proportional to the square of the amplitude, and for our reactions can be written as:

$$\sigma_a = \sigma_d \propto \mid \mathcal{M}_3 \mid^2$$

and

$$\sigma_b = \sigma_c \propto \frac{1}{9} \mid \mathcal{M}_3 + 2\mathcal{M}_1 \mid^2.$$

As is apparent from Figures 1.1 and 2.1, at incident pion energies of about 100 MeV, the isospin $T = \frac{3}{2}$ amplitude dominates; this is referred to as Δ-dominance. In this case, $\mathcal{M}_3$ dominates, and the ratios of the amplitudes of the interactions are $\mathcal{M}_a : \mathcal{M}_c = \mathcal{M}_b : \mathcal{M}_d = 3 : 1$. The corresponding cross section ratio is 9:1 [Gri 87].

At energies below the Δ-resonance region, we cannot assume that $\mathcal{M}_3$ dominates, and we will need to use the scattering amplitude $\mathcal{F}$ to determine the cross section ratio, as discussed later.

2.4 Singlet and Triplet Isospin States

The ^{12}C nucleus can be represented as a ^{4}He configuration with additional filled neutron and proton $p_{\frac{3}{2}}$ shells. A nucleon in the $p_{\frac{3}{2}}$ shell can be excited to the $p_{\frac{1}{2}}$ shell, the $d_{\frac{5}{2}}$ shell, or higher, leaving a hole in the $p_{\frac{3}{2}}$ shell, as shown in Figure 2.2.

A nucleon hole can be created from a closed nucleon shell by the hole operator [Hey 90]:

$$\tilde{a}_{j,m,T,T_3} = (-1)^{j+m+T+T_3} a_{j',-m;T,-T_3},$$

which for nucleons in the $p_{3/2}$ shell can be written as:

$$\tilde{a}_{\frac{3}{2},\frac{1}{2};\frac{1}{2},T_3} = (-1)^{\frac{3}{2}+\frac{1}{2}+\frac{1}{2}+T_3} a_{\frac{1}{2},-\frac{1}{2};\frac{1}{2},-T_3},$$

or a particle in the $p_{1/2}$ shell can be created. Therefore a proton-hole state, $\bar{p}$, is $(-1) \mid \frac{1}{2}, -\frac{1}{2}\rangle$, and a neutron-hole state, $\bar{n}$, is $\mid \frac{1}{2}, \frac{1}{2}\rangle$. A particle-hole system can couple to $T = 0$ or $T = 1$, since both particle and hole have $T = \frac{1}{2}$. The three possible $T = 1$ states form an isospin triplet and the $T = 0$ state a singlet [Gri 87]. In the ^{12}C nucleus assuming no isospin mixing, the 12.71 MeV excitation energy

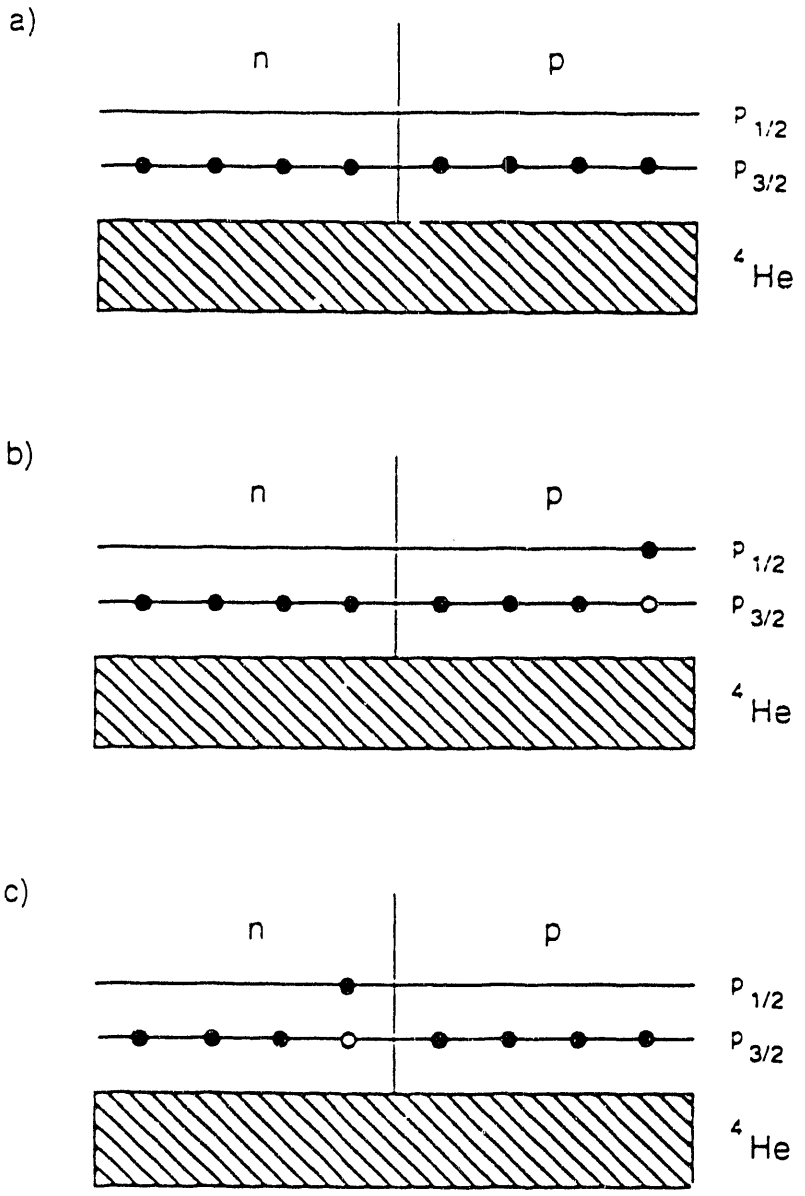

Figure 2.2: ^{12}C shell model configurations showing: (a) possible ground state, (b) a proton is excited to the $p_{1/2}$ shell, leaving a proton hole, $\bar{p}$, in the $p_{3/2}$ shell and (c) a neutron is excited to the $p_{1/2}$ shell, leaving a neutron hole, $\bar{n}$, in the $p_{3/2}$ shell.

state corresponds to the singlet ($T = 0$) state, and the 15.11 excitation energy state corresponds to the triplet ($T = 1$) state, with $T_3 = 0$.

Isospin symmetry should be approximately conserved in nuclear reactions since the strong force, which is independent of charge, is dominant. The full nuclear Hamiltonian H_N therefore should have both a charge-dependent part H_{CD}, and a charge-independent or isospin-conserving part H_{CI}: $H_N = H_{CD} + H_{CI}$.

Using Table 2.2(b) and the $\bar{p}$ and $\bar{n}$ phase conventions given above, we can obtain expressions for the proton and neutron particle-hole states:

$$| p\bar{p}\rangle = -\sqrt{\frac{1}{2}}(| 1,0\rangle + | 0,0\rangle)$$

and

$$| n\bar{n}\rangle = \sqrt{\frac{1}{2}}(| 1,0\rangle - | 0,0\rangle).$$

The isospin states can be expressed as:

$$| 0,0\rangle = -\sqrt{\frac{1}{2}}(| n\bar{n}\rangle + | p\bar{p}\rangle) \equiv | 0\rangle$$

and

$$| 1,0\rangle = \sqrt{\frac{1}{2}}(| n\bar{n}\rangle - | p\bar{p}\rangle) \equiv | 1\rangle.$$

If we consider two states $| A\rangle$ and $| B\rangle$ as linear combinations of $| 0\rangle$ and $| 1\rangle$, they would combine in the following manner:

$$| A\rangle = \alpha | 0\rangle + \beta | 1\rangle \tag{2.1}$$

and

$$| B\rangle = \alpha | 1\rangle - \beta | 0\rangle, \tag{2.2}$$

where $| \alpha |^2 + | \beta |^2 = 1$. (Flanz *et al.* [Fla 79] and Morris *et al.* [Mor 81] define the isospin mixed states slightly differently, which results in an overall phase factor of -1 in the isospin mixing matrix elements which is of no consequence in this work.)

When $\beta = 0$, there is no isospin mixing: $\mid A\rangle = \mid 0\rangle$ and $\mid B\rangle = \mid 1\rangle$. When $\alpha = \beta$, there is maximum isospin mixing: $\mid A\rangle$ is a pure proton particle-hole state and $\mid B\rangle$ is a pure neutron particle-hole state.

Rewriting the states again in terms of the neutron and proton particle-hole states yields:

$$\mid A\rangle = -\sqrt{\frac{1}{2}}[(\alpha - \beta) \mid n\bar{n}\rangle + (\alpha + \beta) \mid p\bar{p}\rangle]$$

and

$$\mid B\rangle = \sqrt{\frac{1}{2}}[(\alpha + \beta) \mid n\bar{n}\rangle - (\alpha - \beta) \mid p\bar{p}\rangle].$$

We previously noted that in the Δ-resonance region the π^+ is three times as likely to interact with a proton as with a neutron, and the π^- is three times as likely to interact with a neutron than a proton. Using these relations, we obtain the following expressions for the cross section ratios in the region of Δ-dominance:

$$\frac{\sigma_A^{\pi^+}}{\sigma_B^{\pi^+}} = \left|\frac{(\alpha - \beta) + 3(\alpha + \beta)}{(\alpha + \beta) - 3(\alpha - \beta)}\right|^2 = \left|\frac{(2\alpha + \beta)}{(\alpha - 2\beta)}\right|^2 \tag{2.3}$$

and

$$\frac{\sigma_A^{\pi^-}}{\sigma_B^{\pi^-}} = \left|\frac{3(\alpha - \beta) + (\alpha + \beta)}{3(\alpha + \beta) - (\alpha - \beta)}\right|^2 = \left|\frac{(2\alpha - \beta)}{(\alpha + 2\beta)}\right|^2. \tag{2.4}$$

If $\beta = 0$, the case of no isospin mixing, then the ratios of $\sigma_A^{\pi^+} : \sigma_B^{\pi^+}$ and $\sigma_A^{\pi^-} : \sigma_B^{\pi^-}$ are $4 : 1$. When $\alpha = \beta$, the case of maximum mixing, the ratio of $\sigma_A^{\pi^+} : \sigma_B^{\pi^+}$ is $9 : 1$ and that of $\sigma_A^{\pi^-} : \sigma_B^{\pi^-}$ is $1 : 9$, characteristic of pure proton and neutron states.

In the case of scattering with incident particles of energies lower than the Δ-resonance region, we need to consider the scattering amplitude $\mathcal{F}$. A nucleon in a closed $p_{\frac{3}{2}}$ shell being excited to a $p_{\frac{1}{2}}$ shell is required to undergo a spin-flip. Therefore the scattering amplitude can be expressed solely in terms of the spin-flip scattering amplitude, g. The isospin $T = \frac{1}{2}$ and $T = \frac{3}{2}$ amplitudes $\mathcal{M}_1$ and $\mathcal{M}_3$ discussed earlier now become:

$$\mathcal{M}_1 = a_{1,1} - a_{1,3}$$

and

$$\mathcal{M}_3 = a_{3,1} - a_{3,3}.$$

The ratio of the amplitudes $\mathcal{M}_a : \mathcal{M}_b$ is often called the spin-flip amplitude ratio and denoted as χ, where

$$\chi = \frac{3 \mid a_{3,1} - a_{3,3} \mid}{\mid a_{3,1} - a_{3,3} + 2a_{1,1} - 2a_{1,3} \mid}. \tag{2.5}$$

Since the amplitude $\mathcal{M}_b$ equals $\mathcal{M}_c$, we can also interpret χ as being the ratio of the amplitudes of $\pi^+ + p$ to $\pi^+ + n$, or $\pi^- + p$ to $\pi^- + n$.

In turn, the cross sections can be expressed generally in terms of χ. The expressions obtained above for the cross sections (Equations 2.3 and 2.4) are appropriate in the Δ-resonance region, where the ratio of $\mathcal{M}_a : \mathcal{M}_b$ is 3:1. This ratio is also expressed by χ. Replacing the 3 in Equations 2.3 and 2.4 for the cross section ratios by χ, the cross section ratios are expressed as:

$$\frac{\sigma_A^{\pi^+}}{\sigma_B^{\pi^+}} = \left| \frac{(\chi+1)\alpha + (\chi-1)\beta}{(\chi-1)\alpha - (\chi+1)\beta} \right|^2 \tag{2.6}$$

and

$$\frac{\sigma_A^{\pi^-}}{\sigma_B^{\pi^-}} = \left| \frac{(\chi+1)\alpha - (\chi-1)\beta}{(\chi-1)\alpha + (\chi+1)\beta} \right|^2. \tag{2.7}$$

Considering again our nuclear Hamiltonian, $H_N = H_{CD} + H_{CI}$, and the following eigenvalue relations:

$$H_N \mid A\rangle = E_A \mid A\rangle,$$

$$H_N \mid B\rangle = E_B \mid B\rangle,$$

$$H_I \mid 0\rangle = E_0 \mid 0\rangle \text{ and}$$

$$H_I \mid 1\rangle = E_1 \mid 1\rangle,$$

we can solve for $\mathcal{H}_{01}$. As shown in Appendix A, for the states $\mid A\rangle$ and $\mid B\rangle$ defined earlier, $\langle 0 \mid H_{CD} \mid 1\rangle = \mathcal{H}_{01}$, and that

$$\mathcal{H}_{01} = \alpha\beta(E_A - E_B). \tag{2.8}$$

E_A and E_B are the energies of the states $\mid A\rangle$ and $\mid B\rangle$, which in our case are the 12.71 and 15.11 MeV excitation energies respectively in the ^{12}C nucleus. The cross section ratios are expressed in terms of α, β and χ. From experiment we can measure the various cross section ratios, thus providing enough information to solve for α and β, and then for the isospin mixing matrix element $\mathcal{H}_{01}$.

Chapter 3

Experimental Technique

3.1 Introduction

The experiment was conducted at the Clinton P. Anderson Meson Physics Facility (LAMPF) in Los Alamos, New Mexico. The equipment used was in Experimental Area A using the Low Energy Pion Channel (LEP), the Scruncher, and the Clamshell spectrometer. Data acquisition was controlled via a computer in the LEP counting house. Figures 3.1 and 3.2 show the locations of these various components. This was the first experiment that used these components together, so each component will be described in some detail in this chapter.

3.2 The LAMPF Accelerator

The LEP channel is one of the beam lines using secondary particles generated by a primary production beam from an accelerator more than 800 meters in length. The primary production beams, both H^+ and polarized or unpolarized H^-, are generated by the LAMPF accelerator, which consists of three sequential accelerator sections.

The first section is the injector system consisting of three Cockcroft-Walton accelerators, each with an ion source producing one of three types of hydrogen ions, H^+, H^-, and polarized H^-. The ions are accelerated to an energy of 0.75 MeV, and released in carefully timed bunches. The next section of the machine is a drift tube linear accelerator consisting of a series of four cylindrical 201.25 MHz radio

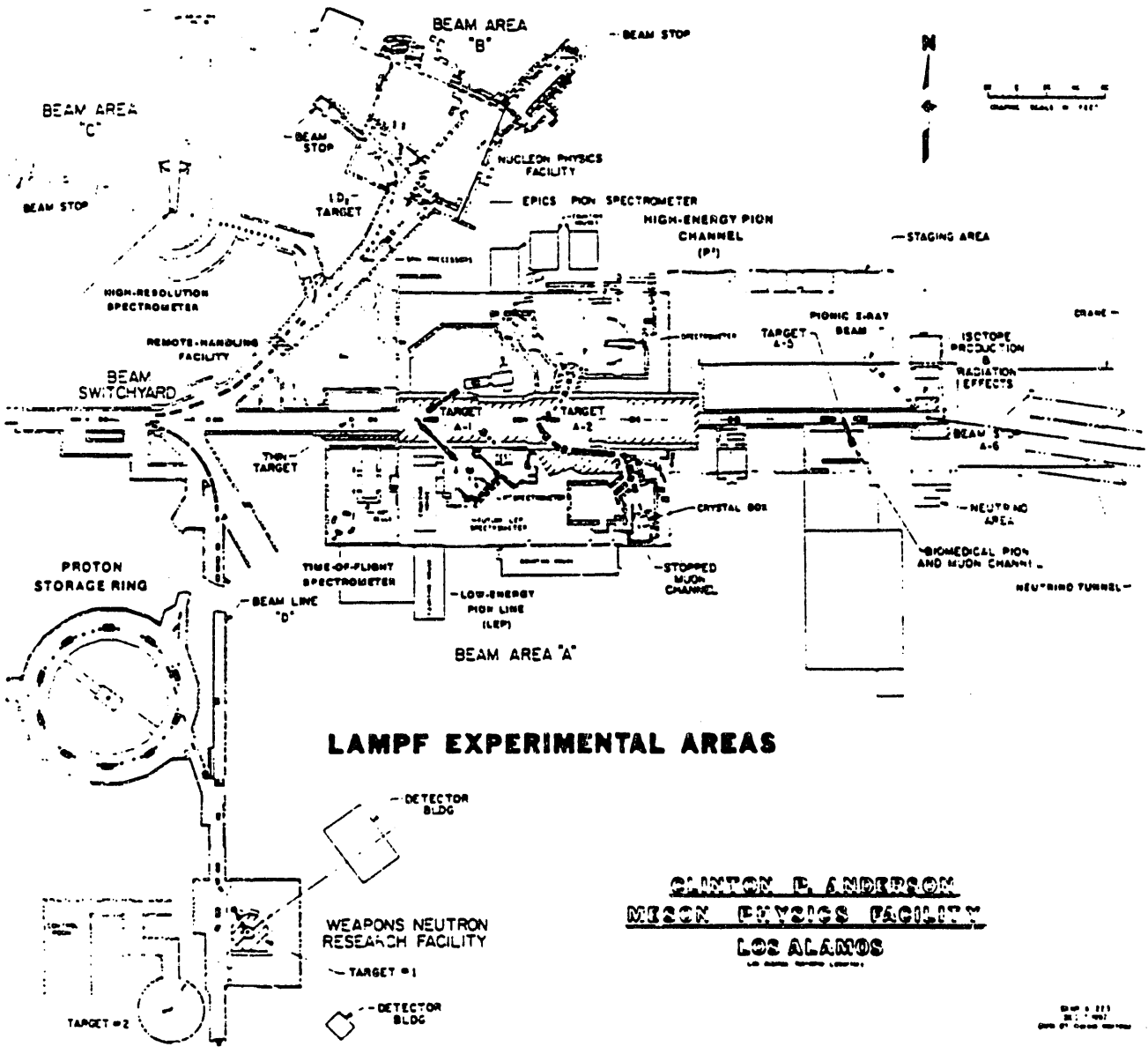

Figure 3.1: The LAMPF facility, showing the location of Experimental Area A.

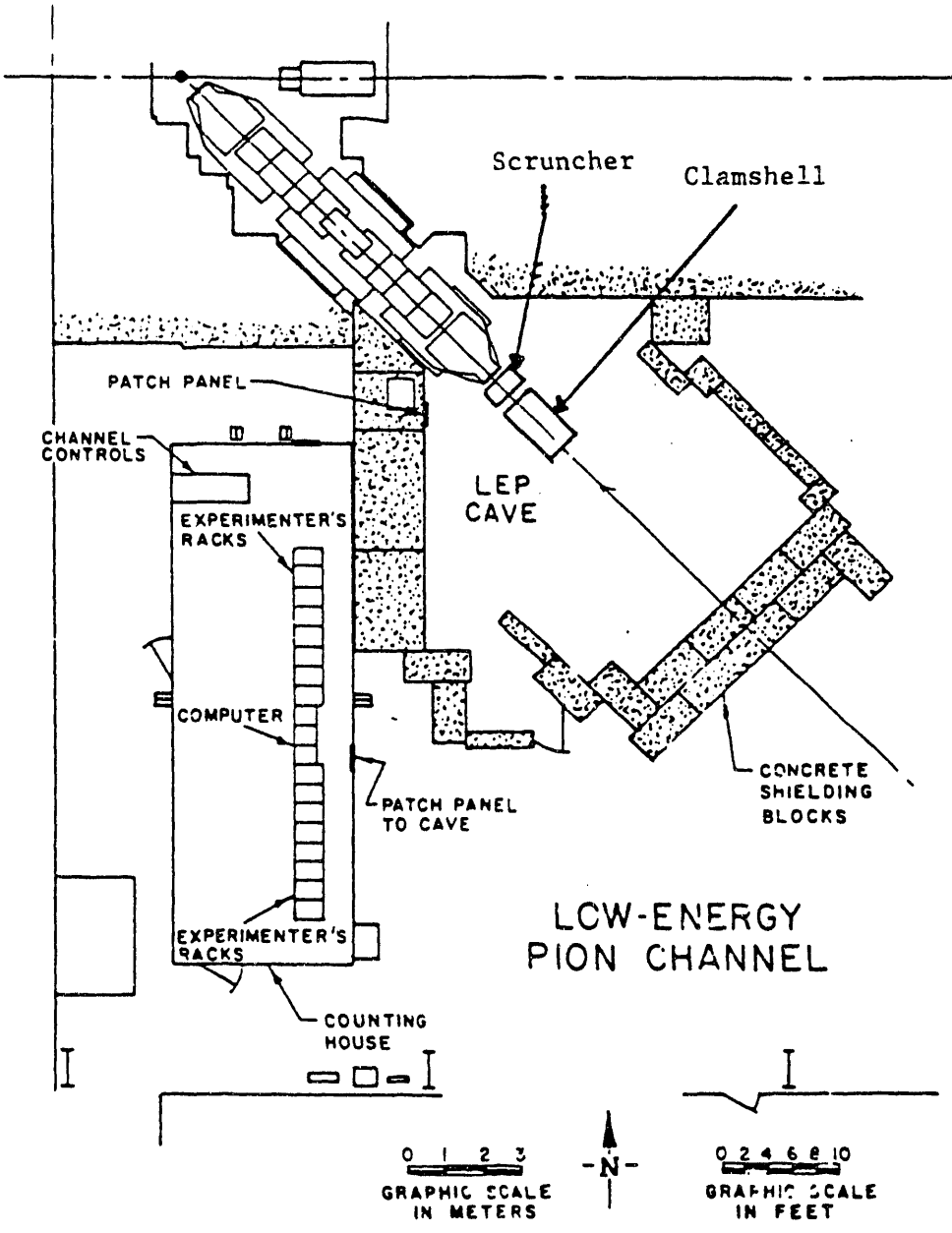

Figure 3.2: Equipment layout in the LEP cave.

frequency (RF) cavities totaling 62 meters long. Each bunch of particles enters this section at the appropriate moment in the RF cycle to be accelerated.

Each RF cavity in the drift tube linear accelerator, or linac, has an alternating electric field and contains drift tubes of increasing length. Positive ions are accelerated in the gaps between the drift tubes for the first half of the RF cycle, and then pass through the drift tubes shielded from the reverse electric field for the second half of the cycle. The drift tubes increase in length as the velocity of the accelerated particles increases. Meanwhile negative ions are accelerated in the gaps by the reversed electric field during the second half of the cycle, and pass through the drift tubes while the positive ions are being accelerated, as shown in Figure 3.3. In this way, two particle beams of different ions can be accelerated simultaneously. The ions leave the drift tube linac with energies of about 100 MeV.

The last section of the accelerator is a side-coupled-cavity linac, with an operating frequency of 805 MHz. The side-coupled-cavity linac is much like the drift tube linac but designed to be more efficient for accelerating higher energy beams, such as the 100 MeV beam coming from the drift tube linac. The particles reach their maximum energy of 800 MeV exiting the final sector of this linac. By turning off sections of the accelerator, different energies can be achieved for the H^+ and H^- beam [LUH 84].

Because the ions are released from the Cockcroft-Walton accelerators in pulses, the beam has a macro-time structure or bunch length ν and a repetition rate n. Typical values of ν and n are 900 ms and 122 bunches per second, respectively. Each bunch has a micro-time structure of 5 ns as a result of being accelerated through the drift-tube linac at a frequency of 201.5 MHz, as shown in Figure 3.4. The duty factor is $n\nu$, in this case equal to about 11%. This means that the beam is actually "on" only 11% of the time [Mit 87].

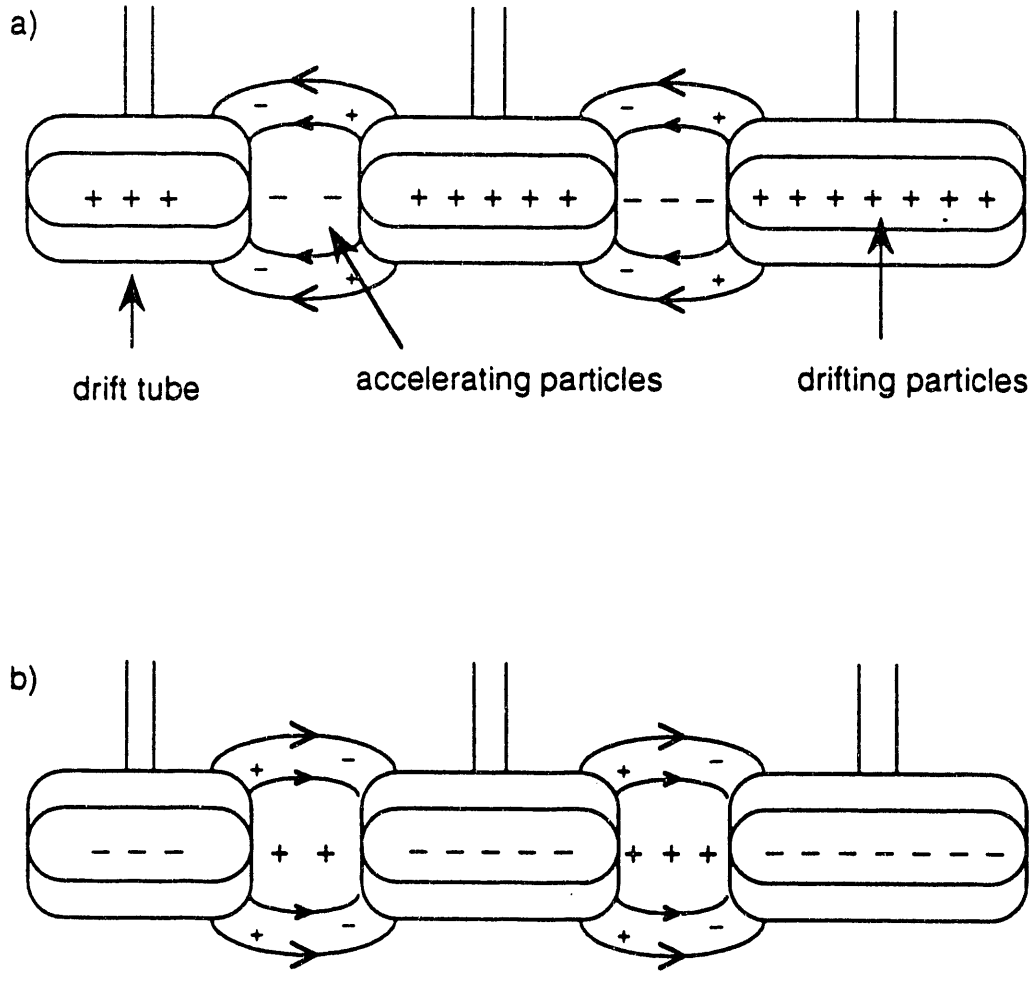

Figure 3.3: Cross section of the drift tube linac at LAMPF. (a) H^- particles are accelerated at this phase in the RF cycle, while H^+ particles are shielded in the drift tubes. (b) When the H^- reach the drift tubes, the RF reverses and the H^+ are accelerated while the H^- are shielded.

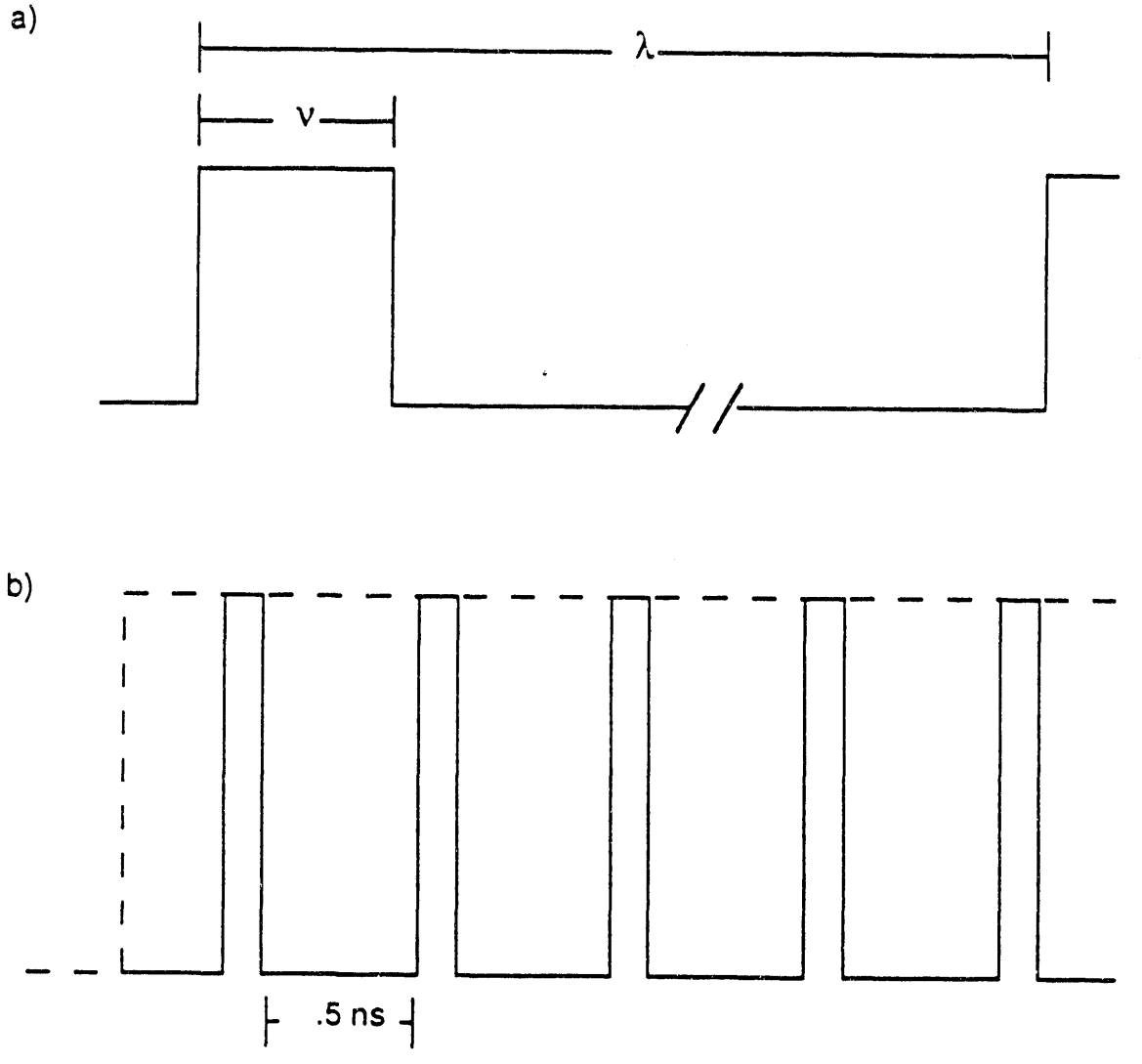

Figure 3.4: Time structure of the primary beam at LAMPF. (a) Macrotime structure where ν is the bunch length. The space between bunches, $\lambda - \nu$, is the time the beam is "off," which in this case was 89% of the total time. (b) Microtime structure of each bunch length, shown to be 5 ns.

At this point the beam enters a switchyard, as seen in Figure 3.1, which directs each beam to different experimental areas. In the case of this experiment, upon entering Experimental Area A, the H^+ beam strikes a graphite production target, the A-1 target, producing pions that enter the LEP channel and another channel.

3.3 The Low Energy Pion (LEP) Channel

A beam channel is a series of magnets and slits that selects particles of the desired momentum in the range available from the incoming particles produced at the production target. The LEP channel, shown in Figure 3.5, is relatively short in order to minimize the decay losses of low energy pions, which have a lifetime of 28 ns. The overall length of the channel is around 13.3 meters.

The first half of the LEP channel disperses the particles in the beam according to their momenta. Maximum momentum dispersion is desired at the center of the channel. The second half of the channel resembles the first half and, for the present experiment, refocuses the particle beam beyond the exit of the channel.

As the beam first enters the channel, a pair of moveable collimator jaws selects the channel solid angle, which can range from 0 msr (closed) to 17 msr (wide open). These collimator jaws also decrease the spread in particle beam momentum and the beam flux.

The first magnetic element of the channel is a quadrupole doublet consisting of two quadrupole magnets (QM01 and QM02). This quadrupole doublet focuses the pion beam onto the momentum slits at the center of the channel, which are discussed further. Between the quadrupole magnets is another pair of jaws, set to block the particles whose paths the first magnet caused to bend such that they would strike the walls of the second quadrupole.

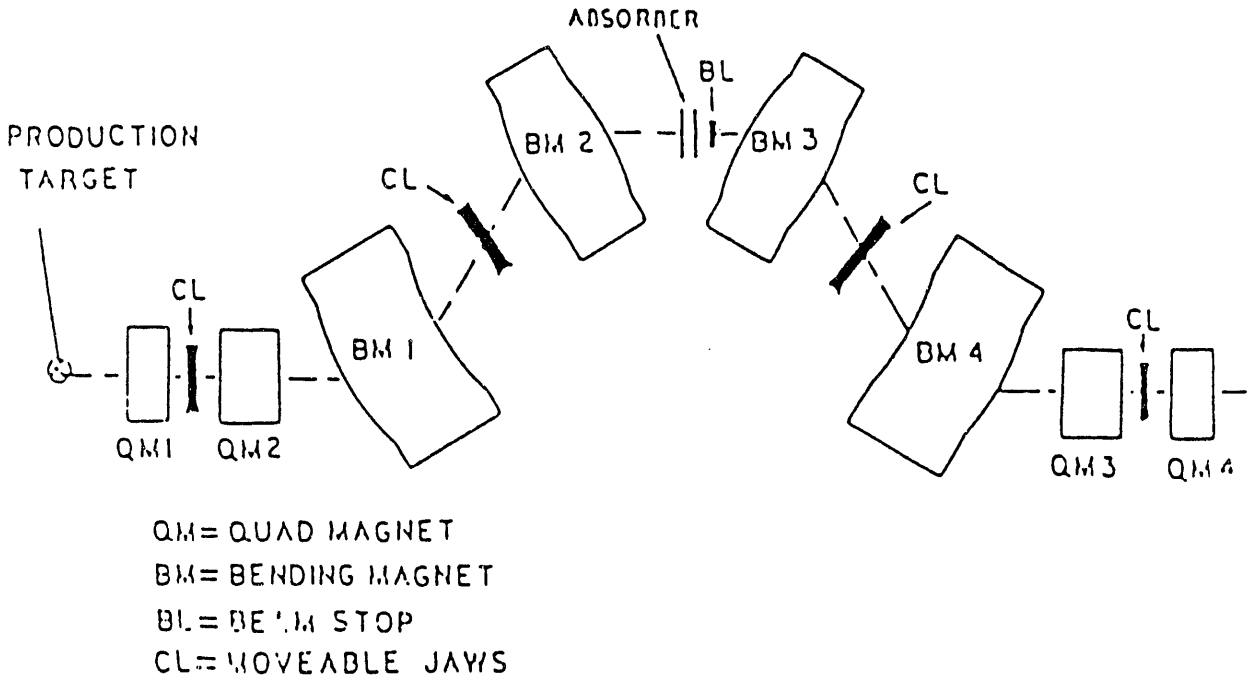

Figure 3.5: The LEP channel.

The dipole bending magnets (BM01 and BM02) bend the trajectories of the pions with the desired momentum so that they pass through the momentum slits at the center of the channel. The collimator jaws between these magnets again block particles with inappropriate trajectories.

The momentum slits at the center of the channel are used to select the momentum range of the beam. They can be moved to select a momentum range, $\Delta p/p$, from 0.05% to 2.8%. A large momentum range will give a high pion flux because the momentum jaws will pass more particles, but poorer channel momentum resolution will result. A small momentum range will give better resolution but a lower pion flux.

In the center of the channel before the momentum slits is a proton absorber assembly consisting of two four-position wheels, allowing for combinations of different absorbing materials. These materials slow down contaminate protons in the π^+ beam [LUH 84]. After passing through the absorber, these protons now have lower momenta than that desired for the pions and they strike collimators in the latter portion of the channel.

The beam then passes through another pair of bending magnets (BM03 and BM04) with collimator jaws, which bend the trajectories of the particles that pass through the absorbers with the correct momentum so that they pass through a final pair of collimator jaws, which selects the final particle acceptance. A quadrupole doublet (QM03 and QM04) refocuses the beam onto a point about one meter beyond the channel exit.

3.4 The Scruncher

For particle scattering spectrometers, the energy and momentum spread of the incident particle beam needs to be minimized. A particle incident on the target may travel a distance through the target material before interacting with a target nucleus. The resulting particles then travel a distance through the target material depending on where within the target material the incident particle interacts. This variation in travel distances, and thus energy losses of the resulting particles, results in a contribution to the energy resolution ΔE_{tgt}, which can be minimized by making the target very thin. However, the thinner the target, the lower the flux of the scattered particles to be analyzed by the spectrometer. The rate of interactions between incoming particles and the target nucleons is given by:

$$R = i \cdot n \cdot \frac{d\sigma}{d\Omega} \cdot d\Omega,$$

where i is the incoming beam flux, n is the target density, $d\Omega$ is the solid angle into which the particles are scattered, and $d\sigma/d\Omega$ is the interaction cross section.

The spectrometer itself has a fixed energy resolution ΔE_{spec} and solid angle $d\Omega$ due to the design and optics of the spectrometer. With only the channel present, $\Delta E_{beam} = \Delta E_{chan}$, where ΔE_{chan}, as mentioned before, is adjusted by the momentum slits in the center of the channel, with the resultant tradeoff between energy resolution and beam flux. The overall energy resolution ΔE of the beam/spectrometer system can be given in terms of the energy resolutions of the channel, target, and spectrometer by

$$(\Delta E)^2 = (\Delta E_{beam})^2 + (\Delta E_{tgt})^2 + (\Delta E_{spec})^2.$$

The Scruncher was developed to improve the energy resolution in the particle beam after it leaves the LEP channel without decreasing the beam flux. In the case of

this experiment then, ΔE_{beam} is also dependent on the Scruncher. This experiment was the first to utilize the Scruncher, so it will be described here in some detail. Further details may be found elsewhere [O'Do 92].

The Scruncher is a superconducting RF cavity that reduces the momentum spread in the pion beam. By using the Scruncher, the center momentum slits in the LEP channel can be opened wider, greatly increasing the pion flux for a given pion beam resolution ΔE_{beam}.

The Scruncher rotates the beam in phase space, or longitudinal coordinates of momentum and time. The beam envelope, the shape of the momentum dispersion of a bunch traveling through the channel, is a tilted ellipse plotted in the longitudinal coordinates, as seen in Figure 3.6. The more energetic or faster particles are in the front, or leading edge, of the envelope, and the slower, less energetic particles are in the back of the envelope. Because there is a correlation between time of flight and energy due to the underlying RF structure of the accelerator, the Scruncher can rotate the phase space of the beam. The field of the RF cavity is adjusted in phase and amplitude so that it decelerates the higher energy particles at the front of the envelope and accelerates the lower energy particles at the back of the envelope. The central momentum particles are unaffected. This results in a rotation of the ellipse in the phase space about the central momentum, which corresponds to focusing the particle beam on a desired momentum. In the present case, the single cell Scruncher RF cavity operating at 402.5 MHz (twice the frequency of the beam) reduces the momentum spread in a 100 MeV beam by a factor of about five, as shown in Figure 3.7. The Scruncher will not improve the flux of a lower energy beam by as much, since the added path length due to the Scruncher will decrease the survival fraction of the beam pions, therefore lowering the flux.

The superconducting cavity was 6 mm thick, made of niobium explosively bonded

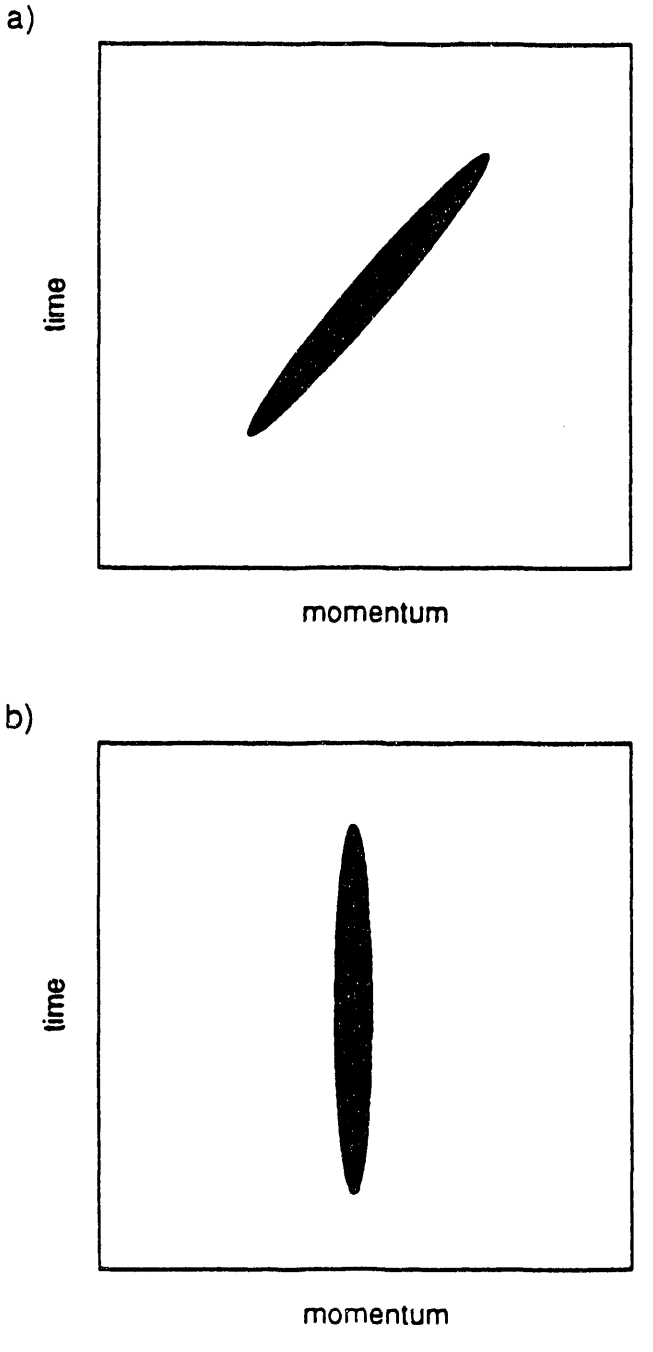

Figure 3.6: Beam momentum phase space envelope a) before Scruncher and b) after Scruncher. The Scruncher speeds up the particles traveling slower than the mean and slows down the particles traveling faster than the mean, resulting in a rotation of the beam momentum envelope in phase space.

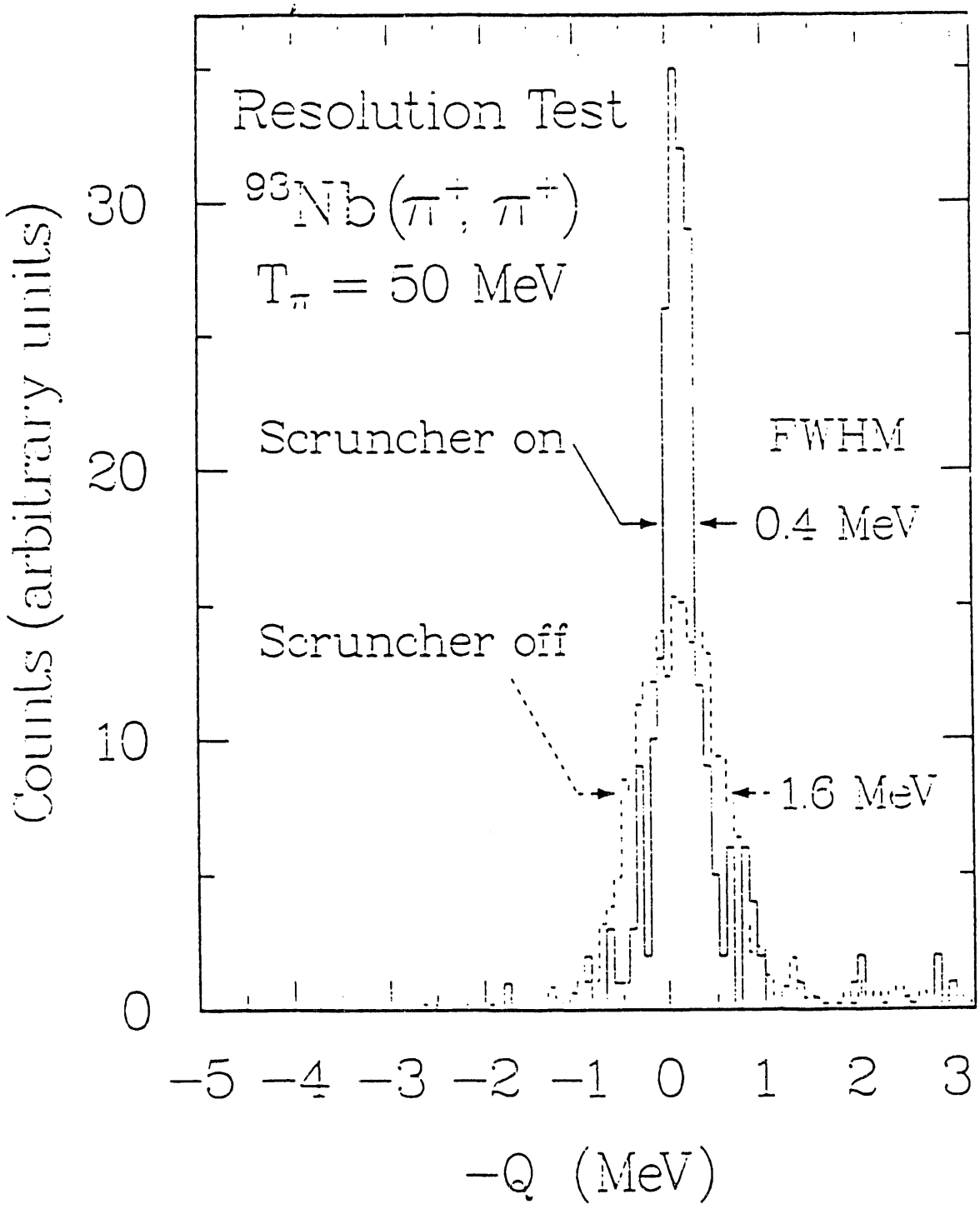

Figure 3.7: Scruncher resolution test comparing the 30° elastic peak for scattering of ^{93}Nb and 50 MeV π^+ with the Scruncher on (solid line) and off (dashed line).

to copper, and was housed in a cryostat cooled by liquid helium. (Figure 3.8) The pions enter and leave the cavity through two 75 μm mylar windows, which have little influence on the pion beam momentum spread.

The central or resonant frequency of the cavity was tuned by actually changing the cavity length with mechanical screws in series with piezoelectric crystals mounted external to the cryostat and controlled from the counting house. Because of vibrations induced by temperature fluctuations, the Scruncher needed to be fine-tuned often during operation to maintain the cavity at its resonance length of 402.5 MHz.

There are three control loops for the RF power system, as shown in Figure 3.9. The self-excitation feedback-loop sends power to the cavity and sets up the standing RF waves in the loop. This system ensures that there are an integral number of wavelengths traveling through the loop, yielding constructive interference in the cavity. If there is destructive interference, waveguide tubes of adjustable length known as "trombones" inserted into the loop to act as delay lines can be used to correct the overlap in the waves traveling through the loop.

The phase-lock control loop adjusts the phase of the cavity so that it corresponds to the phase of the pions coming through the LEP channel, which is set by the phase of the H^+ beam coming from the LAMPF accelerator. This is done through a feedback loop which controls the piezoelectric crystals previously mentioned. These in turn change the cavity length to keep the phase "locked" onto the beam phase. If the feedback loop can no longer control the cavity phase because the needed adjustments are out of its range, then the mechanical tuner can be controlled from the counting house.

The amplitude of the field inside the cavity determines how much the beam envelope will be rotated. The ideal orientation of the rotated envelope is vertical.

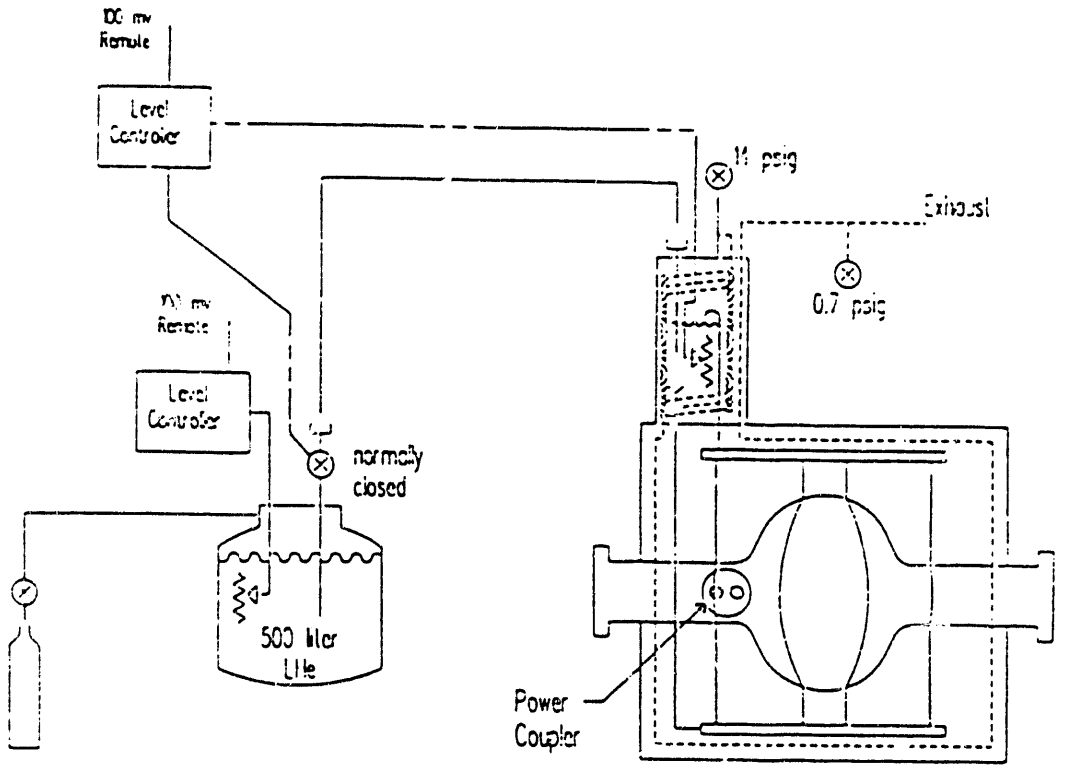

Figure 3.8: Cooling system for the Scruncher.

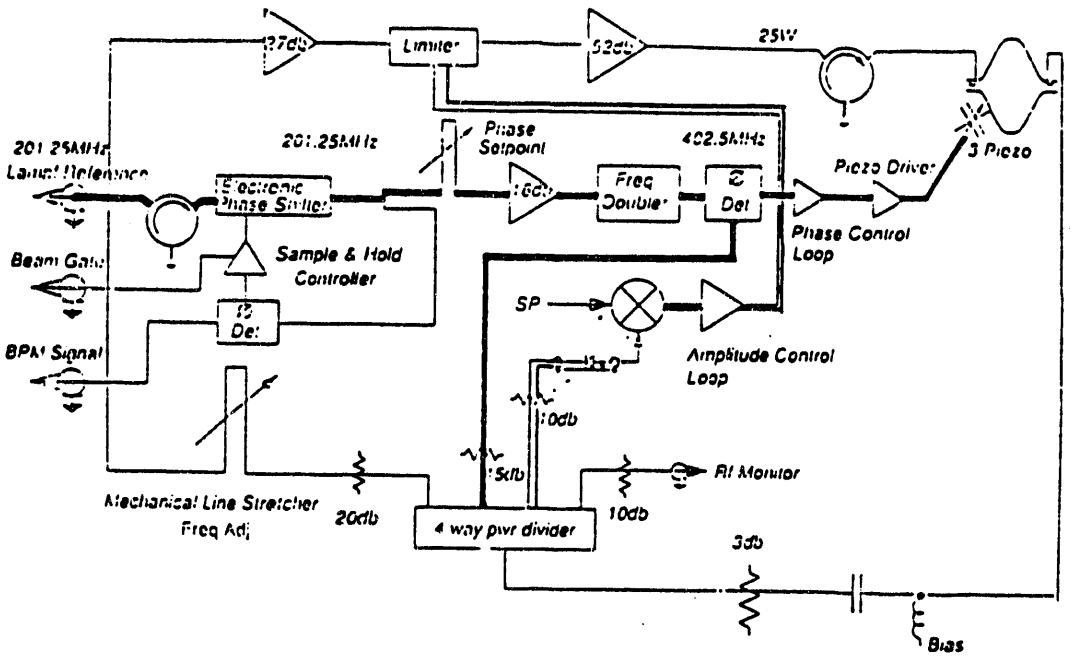

Figure 3.9: RF control circuit for the Scruncher. The bold line shows those elements of the circuit unique to the phase-lock control loop, and the double line shows those elements unique to the amplitude control loop.

If the cavity field amplitude is set too low, the beam envelope will not be rotated enough; too high an amplitude will rotate the beam too much. For this experiment the amplitude was set at 3.5 MV/m, determined by examining the MMCT histogram discussed in the next chapter. In this histogram, the tails correspond to pions traveling faster or slower than those of the desired momentum. The Scruncher amplitude is adjusted until these tails are negligible. The amplitude control loop adjusts the amplitude of the field in the cavity to be consistent with this optimal setting. If necessary, a limiter on this loop reduces or increases the amount of power sent through the self-excited loop to the cavity in order to correct the amplitude.

3.5 The Clamshell Spectrometer

The Clamshell spectrometer analyzes the products from reactions induced on the target by determining the energy and position of these reaction particles.

The device is a single dipole magnet with non-parallel pole faces, as shown in Figure 3.10(a). This pole face configuration creates a non-uniform magnetic field inside the spectrometer that focuses particles onto the median plane, thus increasing the spectrometer solid angle to about 40 msr. The Clamshell also has a relatively short path length of 1.8 m to minimize pion decay loss, and can be moved through a wide range of scattering angles, -20° to 140°. With the Scruncher in place however, there was only space to move the spectrometer such that the maximum angle attainable was 103°.

The scattering chamber, located between the Scruncher and the entrance to the spectrometer, contained a target assembly that could be controlled from the counting house. The chamber was kept at vacuum with a sliding seal port connecting the chamber and spectrometer. The scattering chamber could thus remain stationary

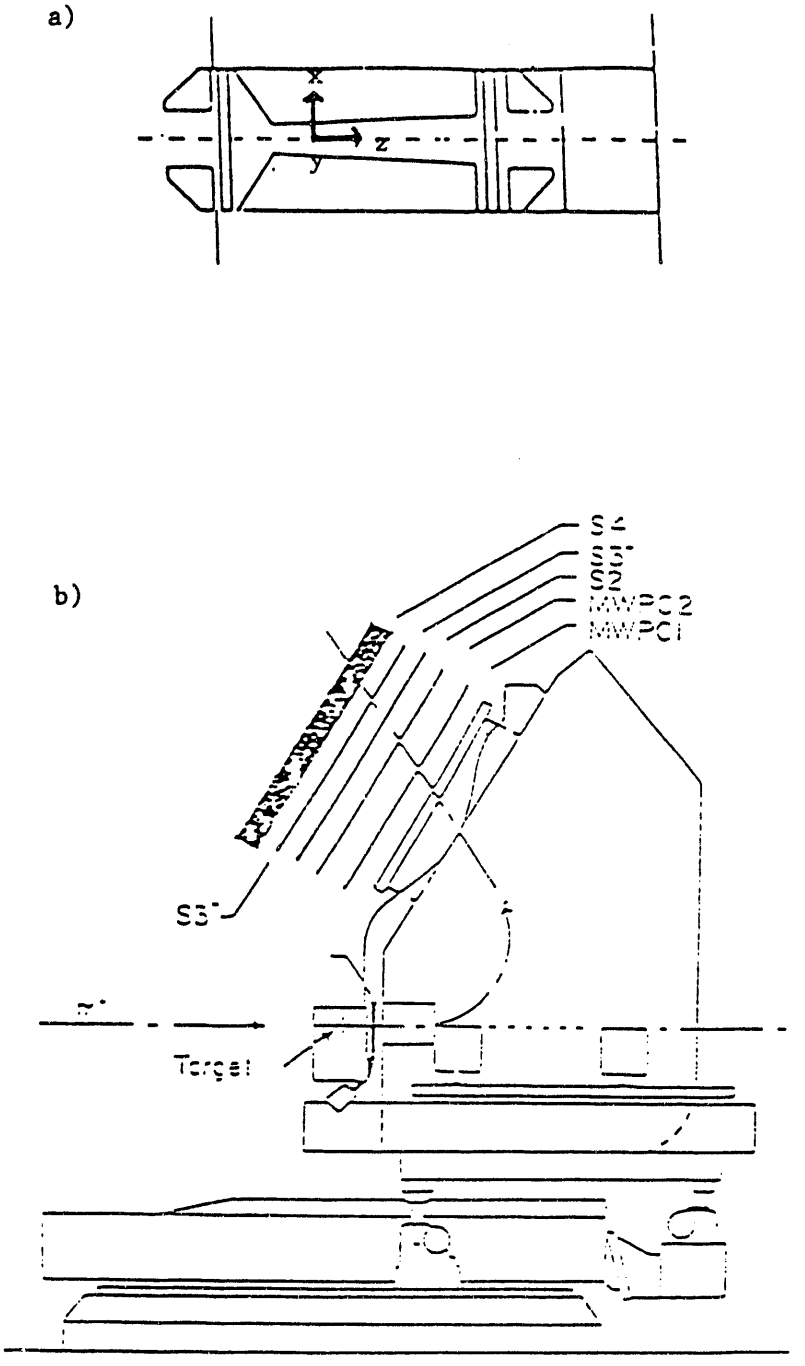

Figure 3.10: The Clamshell spectrometer. (a) Cross section of the Clamshell magnet showing the non-parallel pole faces and alignment of the coordinate system axis. (b) Clamshell spectrometer and detector arrangement.

when the spectrometer was moved to collect data at different scattering angles. The targets were about 5 cm^2 in size. For this experiment, a target of natural ^{12}C with a thickness of 262.8 mg/cm^2 was used. The entrance and exit of the scattering chamber consisted of thin mylar windows.

The path of particles through the Clamshell magnetic system is analogous to light through an optical system. If we consider a coordinate system, as shown in Figure 3.10(a), with the direction of the beam as z, the dispersion direction along the median plane as y, and the nondispersion direction (perpendicular to the field) as x, we can define a set of variables that describe the position of the particles at the target. These variables are x, $dx/dz \cong \theta$, y, $dy/dz \cong \phi$, ℓ = path difference from the central ray, and $\delta_{spec} = (p - p_o)/p_o$, where p_o is the central momentum, the momentum selected by the channel magnets. Considering these variables as a six-dimensional vector, another six-dimensional vector can be constructed consisting of the coordinates x', θ', y', ϕ', ℓ', and δ'_{spec}, representing the position of the particle upon exiting the spectrometer to first order. These two vectors are related by a 6×6 transport matrix M that describes the optics of the clamshell system. After M has been determined, it can be inverted to find the unprimed vector from the primed vector. In the present case, this technique was extended to include higher order terms by expanding each of the unknown terms, such as δ'_{spec}, in a Taylor series polynomial in measured quantities. The coefficients were measured by using ^{12}C elastic scattering, where the final and initial positions of the scattered pions were known [Mor 92].

Normally, the LEP channel focuses the particle beam into a tight beam spot on the Clamshell target. In this experiment however, the Scruncher was placed between the exit of the channel and the target, so the beam was not focused on the target, but rather a meter beyond the channel exit. This resulted in a much

larger beam spot than usual on the target, an ellipse 2.5 cm high and 4 cm long. This means that the initial particle position could have been anywhere within an area of about 7.9 cm^2. Thus, for this experiment, a front strip cathode readout wire chamber A11 was placed between the exit of the target chamber and the entrance of the spectrometer to measure the initial particle position with a precision of better than 0.5 mm.

A set of focal plane detectors at the exit of the system provided the information necessary to determine the primed variables. The detectors were two sets of x-y delay line readout drift chambers and plastic scintillator counters S2, S3, S4, S5, S6, and S7, as shown in Figure 3.10(b). (The scintillator S1 normally in position immediately after the target was replaced by A11 for this experiment because of the uncertainty in the initial position due to the Scruncher.)

The drift chambers determined the position of a particle that passed through them to a precision of about 200 μm. The drift chambers together provided information on x, y, x' and y'. A11 was 6 cm by 4 cm with the long axis mounted vertically. The focal plane drift chambers were 90 cm by 30 cm. The latter were mounted with their long axis along the dispersion direction.

The focal plane chambers consisted of two layers of anode wires, one in the x-direction and one in the y-direction, sandwiched between two cathode planes as shown in Figure 3.11. The anode and cathode wires were spaced 8 mm apart. A positive voltage on the anode creates a logarithmic electric field. Electrons excited and freed by passing particles drift toward the anodes at a velocity which is nearly independent of the electric field. Positive ions drift toward the cathodes. The high electric fields near the anodes cause the electrons to accelerate, thus producing a chain reaction where the electrons excite other electrons which in turn excite more electrons, a process known as avalanching. The electrons reach the anode and

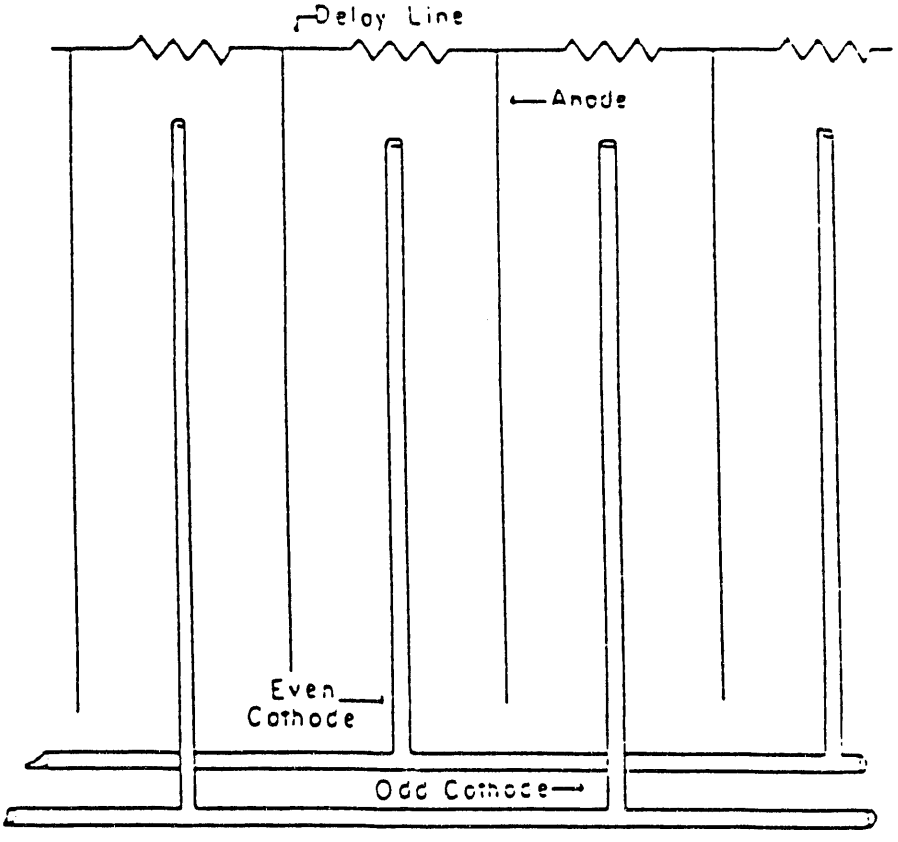

Figure 3.11: A one-dimensional drift chamber. A particle passes through the drift chamber at point X, ionizing the atoms in the gas. The freed electrons drift toward the positively charged anodes, and the positively charged ions drift toward the negatively charged cathodes. Even and odd cathodes help eliminate LR ambiguity, and delay lines correct for the difference in the drift times of the electrons and ions.

produce a strong negative signal. The anodes were connected to a delay line of 2.5 ns/cm, to account for the electrons moving faster than the ions. This delay line is referenced to S2 so that when a particle passes through S2, a start signal is given to the wire chamber and both ends of the delay line are read. The time difference between the arrival of the signal from the left end of the delay line and the arrival of the signal from the right end of the delay line gives the position of the anode wire closest to the passing particle, and the sum of these times gives the particle's drift time.

There are also two sets of cathode wires bussed together alternately. One set of cathode wires was designated as "odd" and the other "even". The two types of cathode wires helped to determine from which side of the anode layers a signal came, since a stronger signal on one of the two indicates that the particle passed closer to that cathode. This resolves the "left-right ambiguity" in that it assigns the drift distance to one side or the other of the anode wire.

The chambers were filled with a mixture of argon, isobutane, and alcohol at atmospheric pressure from the gas handling system in another beam channel. Argon is a noble gas and therefore requires the lowest electric field intensity for avalanche formation. Isobutane helps to prevent the avalanche from spreading by absorbing UV light without ionizing. The alcohol prevents the isobutane polymers from accumulating on the wires [Leo 87].

The scintillator counters provided information to determine the type and energy of the incident particle. S2 and S3 were 15 cm by 80 and 90 cm respectively, and were 6.4 mm thick [Esc 89]. Their long axes were aligned in the dispersion direction (x-direction), and each had photomultiplier tubes at both ends.

When a particle passes through the scintillator, it excites atomic electrons in the scintillating material which de-excite by emitting photons. These photons are

transmitted by total internal reflection toward the ends of the scintillator where they strike the photocathodes in the photomultiplier tubes (Figure 3.12). The signal from the scintillator is amplified in the photomultiplier tubes when the incident photons absorbed by the photocathode convert to electrons through the photoelectric effect. These electrons cascade through the tube from dynode to dynode, releasing more electrons at each level. A 65 MeV pion deposits about 2.7 MeV in excitation energy in the scintillator which in turn creates about 30 electrons from the photocathodes of the photomultiplier tubes [Leo 87]. Typical photomultiplier gains are about 10^6 to 10^7.

If the point the particle passes through the scintillator is closer to one end, the closer photomultiplier tube will receive a stronger signal than the farther one because more photons will reach that photomultiplier tube. By using two photomultiplier tubes, mean pulse heights of the signals can be determined so that the strength of the signal is independent of the position on the scintillator through which the pion passes.

The detector plane was not parallel to the optical focal plane of the spectrometer, but was rotated by 19° about the x-axis. This made the incident angle of the particles to the detectors closer to normal, and moved the first wire chamber from the fringe field at the exit of the spectrometer.

3.6 Electronics

Raw signals from the drift chambers and scintillators were sent to the counting house via signal cables properly impedance-matched to their signal sources. Once in the counting house, the signals were sent to various NIM modules (nuclear instrumentation modules) and to a modular data acquisition instrumentation system

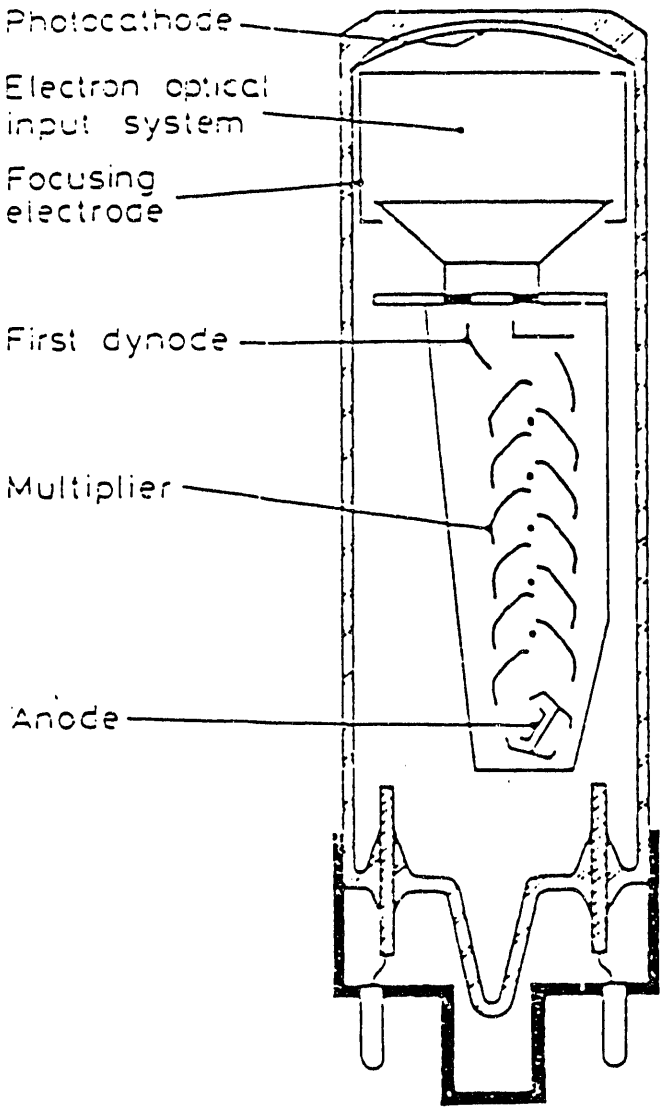

Figure 3.12: Interior of a photomultiplier tube. If one electron is incident on the first charged plate in the tube, it excites two electrons, which in turn excite two electrons each on the second charged plate, producing a cascade effect which "multiplies" the initial electron.

in CAMAC (computer automated measurement and control). The NIM modules were contained in NIM bins, which are simply power sources for standard modules (coincidence units, discriminators, meantimes, level shifters, linear and logic fan-in/fan-outs, etc). The CAMAC modules were in CAMAC crates, which act as both a power source and as a dataway for communication between modules [such as analog-to-digital converters (ADCs), time-to-digital converters (TDCs), and scalers (counters)] in different crates.

The analog signals coming into the counting house from the scintillators and the delay lines of the wire chambers were sent to discriminators for timing information, linear fan-in units for summing, and ADCs for pulse-height determination. The electronic signals from the wire chambers only had a 1-3 mV amplitude and were amplified by about a factor of 100 to match the pulse heights of the scintillator signals, which had amplitudes of about 100-500 mV [Mit 87].

Also used was a hardware trigger, an implementation in hardware of a set of logical conditions which must be met to signal that a valid event occurred. This minimizes the number of bad events written to tape. For this experiment, a spectrometer event was defined as the coincidence of a logic signal from both the discriminators of S2 and S3, along with a signal from the wire chambers (any two delay lines) indicating that a particle had passed through the spectrometer. This condition can be expressed as:

$$Event = S2 \cdot S3 \cdot anytwodelaylines.$$

A $\overline{veto}$, or "not veto" logic signal, was added for the trigger:

$$\overline{veto} = \overline{computerbusy} \cdot \overline{beamgate} \cdot \overline{rungate}.$$

$\overline{Computerbusy}$ ("computer not busy") was a signal generated by the computer used for data aquisition to indicate when it was ready to accept signals. $\overline{Beamgate}$ ("not

beamgate") meant that there was secondary beam entering the experimental area. When the software system was ready for acquisition, this generated the run signal; $\overline{rungate}$ meant that this signal was being generated and a data taking run was in progress. The actual conditions for the trigger can be written as:

$$Trigger = Event \cdot \overline{veto}.$$

When there is an event trigger, a signal is sent to a special CAMAC module known as the LAMPF Trigger Module (LTM). The LTM signals a primitive computer, the Micro-Programmable Branch Driver (MBD), that an event has occurred. The MBD has been programmed to interact with CAMAC crates and to pass their data to the experiment computer, which for this experiment was a Micro-Vax II. There may be several types of events, and the MBD is programmed to process each of these. The LTM indicates to the MBD which event has occurred. Besides the spectrometer event discussed above, another possible event is an EOR (end of run) event, which occurs when the Micro-Vax signals the LTM that a data taking run is completed. Another event type is a scaler, or pulse counter, event, where all the scalers are read out to prevent any of them from exceeding the 2^{24} maximum value they may have. Each event results in a stream of data words being funneled from the CAMAC crates to the Micro-Vax via the MBD, as demonstrated in Figure 3.13.

Data such as pulse heights and timing information for a spectrometer event and scaler values for a scaler event, are sent to the Micro-Vax to be studied and manipulated on-line ("real time") by the appropriate experiment-specific software called an analyzer. This analyzer, described in the next section, will generally process data only if the computer is not busy ("may process" mode), but can be forced to process data ("must process" mode) if the computer busy signal is received. All data are immediately passed to magnetic tape for off-line processing

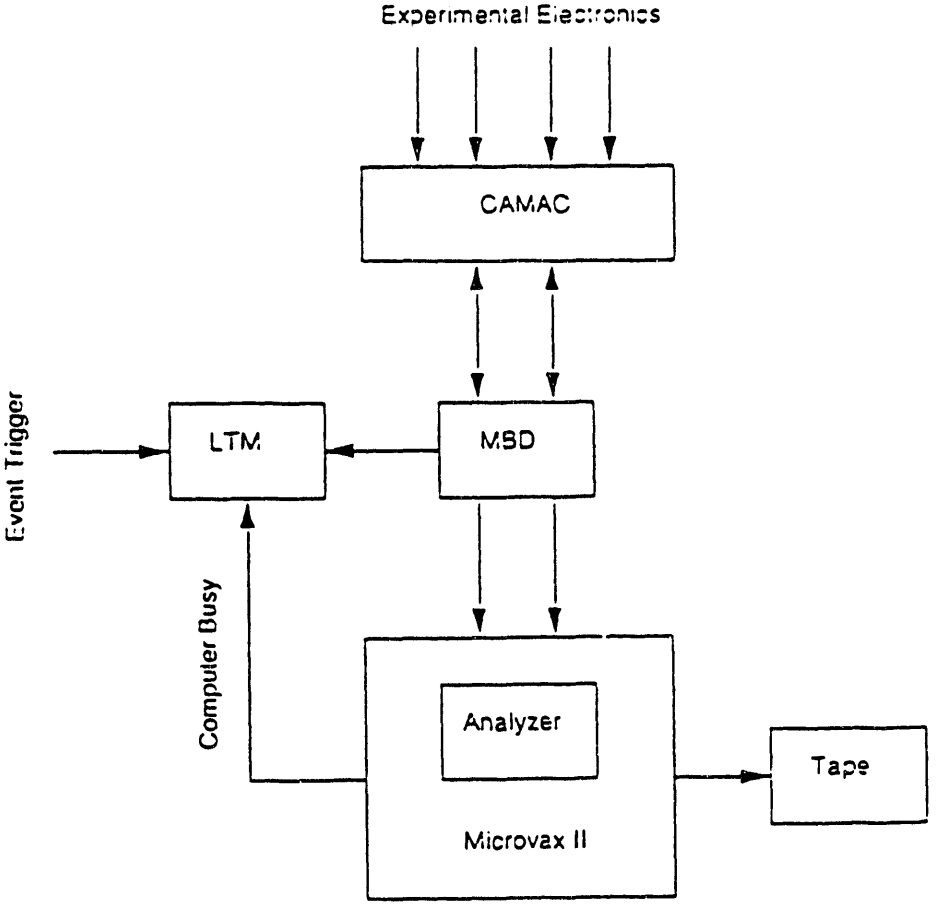

Figure 3.13: Data acquisition flow chart.

by the analyzer. Since some data passed to magnetic tape do not go to the analyzer on-line if the computer is busy, more data are written to tape than are analyzed on-line. On-line analysis therefore has an additional factor, computer livetime, that needs to be taken into consideration. Other deadtimes, such as the instrumental deadtime arising due to the logical signals having a typical width of 50 ns, and devices such as the wire chambers having intrinsic resolution times on the order of 100 ns, are implicitly corrected in the hardware logic.

3.7 The Q-System Data Acquisition and Analysis Software

The Q-system is a collection of software programming tools for data aquisition and analysis running under the VAX operating system VAX/VMS. The software package is a flexible system that can be modified to suit each experiment. The major Q subsystems are acquisition/replay control and information, histogramming, data testing, and the dynamic parameter array. (Figure 3.14)

The experiment specific analyzer task carries out analysis to be done on data acquired either from the CAMAC crates (while a run is in progress) or from tape (through replaying the data). The acquisition process is controlled using various standardized FORTRAN commands and procedures, such as accessing tape drives for writing or reading, compiling MBD code, and starting, suspending or stopping a run.

The histogram package allows the user to access both stored and on-line histograms, save and retrieve histograms, and create, increment and delete histograms based on tests and the analyzer.

The test package is closely linked to the histogram package. The test package performs arithmetic and logical tests on the data and can perform logical tests of

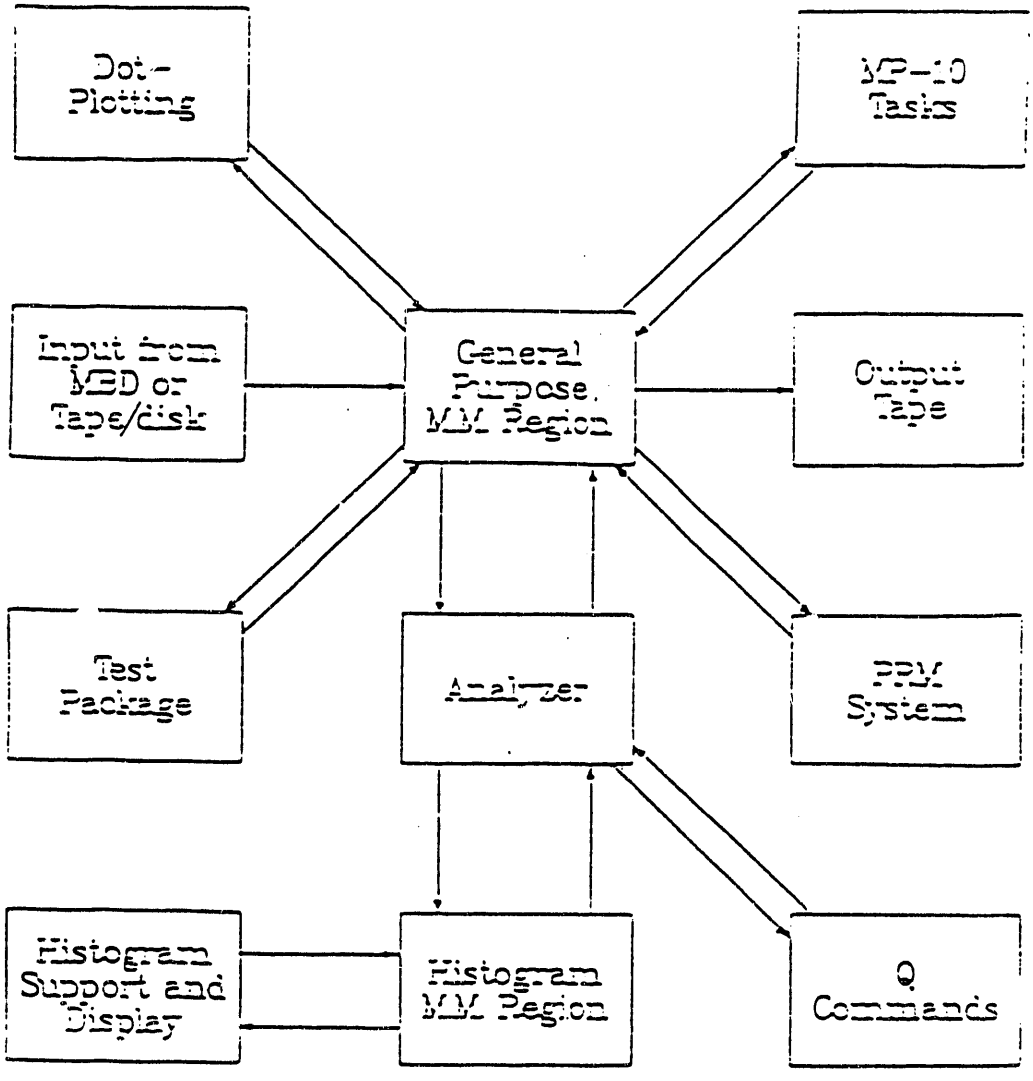

Figure 3.14: Q-system flow chart.

previous tests. The test package also provides a counter for each test over an entire run, and these counter values are stored in a histogram file. The user may also create, execute, retrieve and save sets of tests to be applied to the data. The results of the test package can be used to control histogram entry, such as restricting one histogram to only include a specific peak from another histogram.

The parameter subsystem provides dynamically adjustable parameters, such as interaction energies, scattering angles and magnetic field values that can be adjusted during a run. These in turn can be used by the analyzer program to calculate new values and run new tests. The parameter subsystem also supports definitions of synonyms for both individual variables and groups of arrays.

Chapter 4

Data Reduction and Analysis

4.1 Introduction

The procedure used for reducing data for this experiment involved replaying the data with various tests and conditions using the Q-System in order to remove as much background from the histograms as possible. Sources of this background can be contaminates in the target or its frame, from the mylar windows, or accidentals. Next, the reduced data were scanned for peaks, and the areas of the peaks were determined using a peak-fitting routine. In the last step, cross sections were determined based on a normalization to previous data. Each of these steps used standard procedures for analyzing data taken at LAMPF, and each step will be discussed in detail in this chapter.

4.2 Replay

As described in the preceeding chapter, the Q-system allows FORTRAN variable names to be assigned as labels to specific data words of interest obtained from the CAMAC modules. For example, TOR1 was the software label associated with the hardware data word for the number of counts recorded in the scaler for the first production beam monitor, a torodial counter located near the A-1 production target. IS5R was the software label associated with the hardware data word for the pulse height coming from the right end of the fifth scintillator detector on the Clamshell

focal plane. The Q-system also allows manipulation of these data words to produce calculated data words or combinations of these. For example, the variable SESUM is the data word that labels the sum of the energies deposited in all the scintillator detectors by a single particle, which in turn was calculated from the pulse heights obtained from the scintillator photomultiplier tubes.

The Q-system's histogram package allowed plotting various data words individually or correlated with each other, and could also include logical tests on the data words. The histograms used most often in this experiment, described in turn below, were those for the data words corresponding to: corrected time-of-flight, whose histogram was named CT; energy difference, named ED; missing mass, named MM; and missing mass optimized, named MMOP.

CT was the histogram of corrected time-of-flight. Time-of-flight was the time taken for a particle to pass through the channel and the spectrometer to the focal plane detectors. Since muons, protons, postitrons and pions with the same momentum travel at different speeds through the system, they have different times-of-flight. The corrected time-of-flight was calculated time-of-flight adjusted so that the elastically scattered pion time-of-flight through the spectrometer is at channel 0 on the CT histogram. As shown in Figure 4.1, a peak was observed centered on channel 0, but also some counts below the central peak. Those counts below the peak were pions that scattered inelastically, therefore losing some of their energy and taking longer to travel through the spectrometer. A test, or gate, was set on the CT histogram around the region of the pion peak to include elastically and inelastically scattered pions.

ED was the histogram of energy transfered to the target nucleus, known as energy difference. ED was adjusted so that elastically scattered pions are at channel 0. Energy difference was defined as

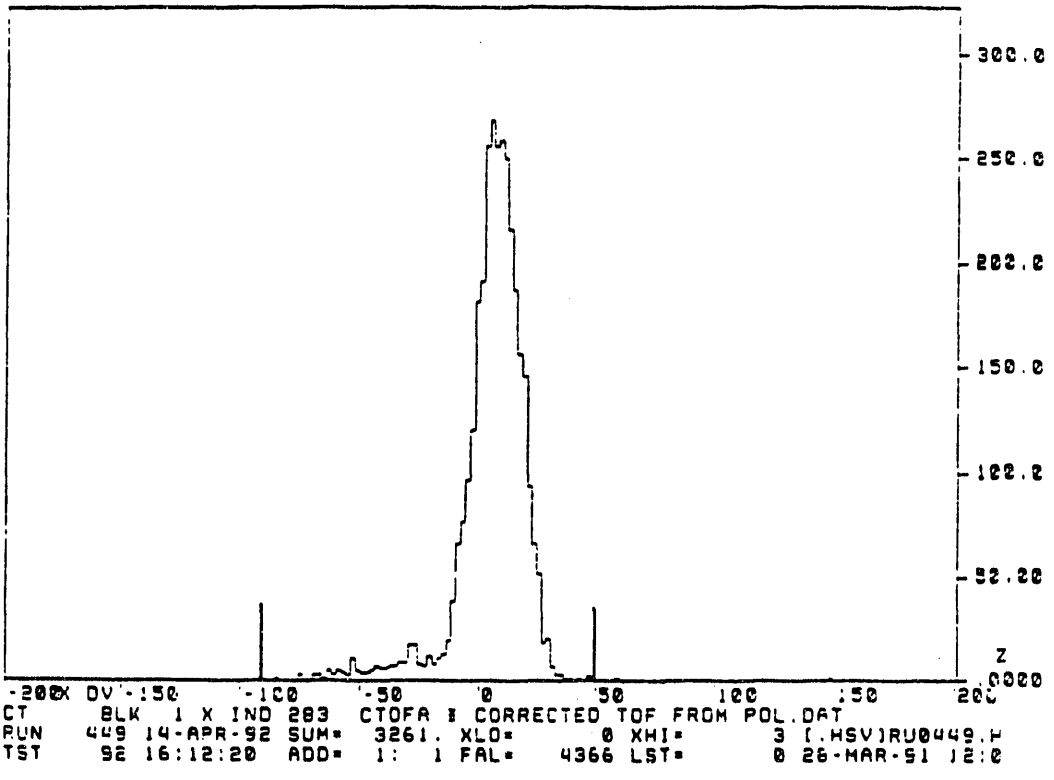

Figure 4.1: CT histogram for lab spectrometer angle of 60°, ^{12}C 50 MeV π^+ scattering. There is a gate set on the pion peak which includes both the elastic and inelastically scattered pions. The time scale is from -2 ns to 2 ns.

$$ED = T_\pi\text{-}SESUM,$$

where T_π is the incident pion kinetic energy. As seen in Figure 4.2, the elastically scattered pions were centered at channel 0 because most pions were elastically scattered and lost almost no energy in the scattering process. Thus, their kinetic energy was deposited in the scintillators, because the focal plane scintillator array was thick enough to stop 50 MeV pions. Therefore SESUM equals the pion kinetic energy. The inelastically scattered pions lost energy in the scattering process, so SESUM was less than T_π, and yielded a positive ED. The counts to the right of the central peak on the ED histogram were therefore also identified as pions. If the momentum of a muon p_μ is equal to the pion momentum p_π, then the muon kinetic energy is greater than T_π. Therefore muons were located to the left of the central peak because they deposit an energy more than T_π into the scintillators. Like CT, a gate was set on ED to distinguish the pions from other particles.

In the case of an incoming π^- beam, the π^- particles are often stopped by the scintillating material and create pionic atoms. In this case, the pion is absorbed and SESUM also incorporates the pion rest energy. Thus SESUM is greater than the kinetic energy of the incoming beam and the gates are set "wide open" to include all events in the ED spectra, with both positive and negative values of ED.

Missing mass corresponded to the excitation energy of the ^{12}C nucleus, and the MM histogram (Figure 4.3) was the spectrum of excitation energy. Missing mass, Q, is given by:

$$(Q + m_{^{12}C})^2 + p_{^{12}C}^2 = (SESUM + m_\pi - \sqrt{p_{^{12}C}^2 + m_{^{12}C}^2} + m_{^{12}C})^2.$$

The unknown quantity in this expression, $p_{C^{12}}$, can be determined using wire chamber information, since position on the focal plane is dependent on the pion momentum and its scattering angle. Using the appropriate values for scattering angle

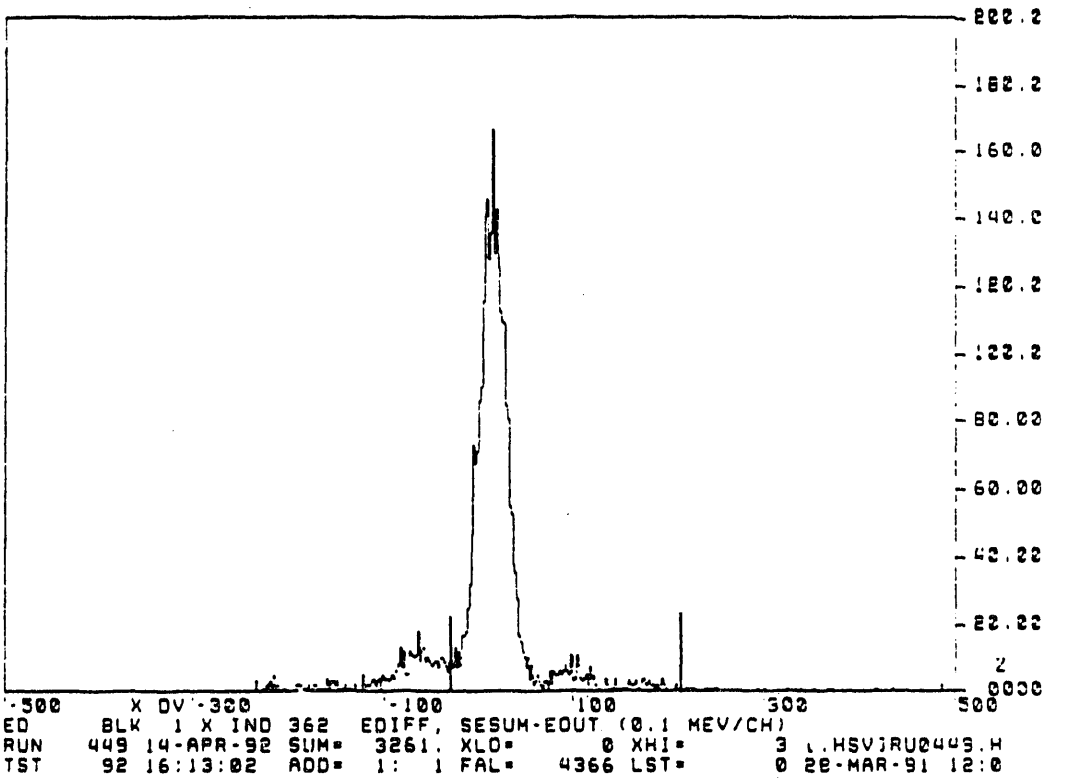

Figure 4.2: ED histogram for lab spectrometer angle of 60°, ^{12}C 50 MeV π^+ scattering. There is a gate set on the pion peaks to distinguish them from those of other particles. Particles to the left of the central peak, elastically scattered pions, are inelastically scattered pions having positive values of ED. The scale is 1 MeV per 10 channels.

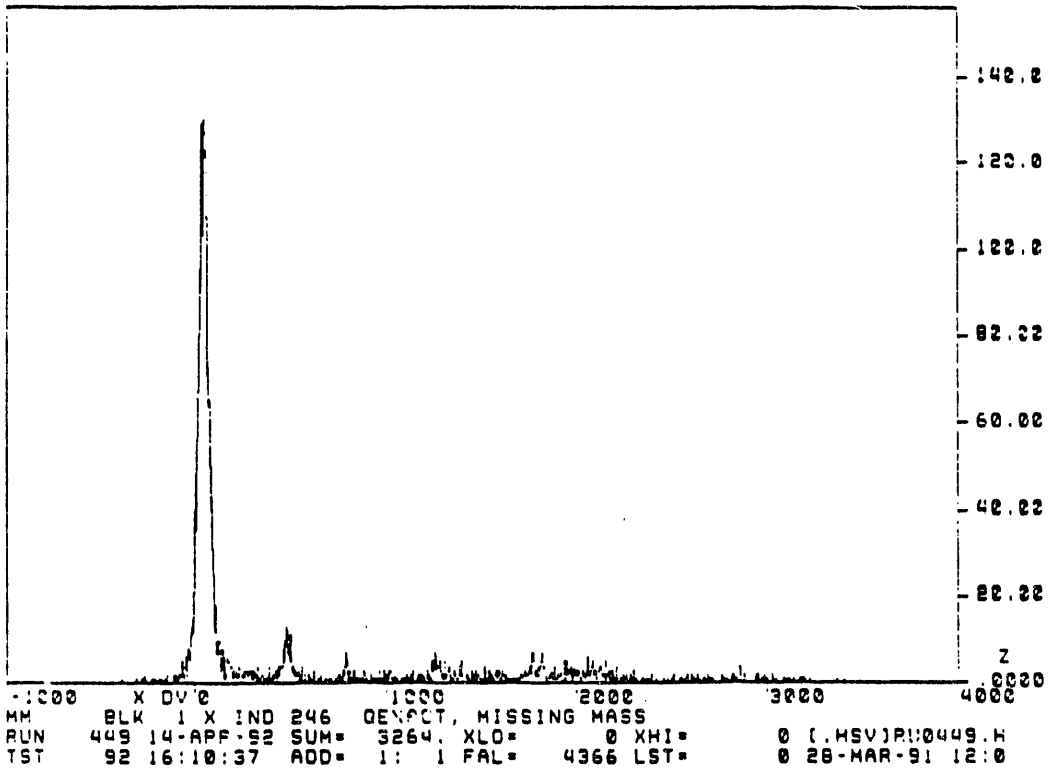

Figure 4.3: MM histogram for lab spectrometer angle of 60°, ^{12}C 50 MeV π^+ scattering. The peaks correspond to ^{12}C excitation levels. 1 MeV corresponds to 100 channels.

and momentum for a given event, $p_{C^{12}}$ can be calculated using two-body kinematics; this was done with CALKIN, a kinematics program used by the analyzer. Q=0 corresponded to channel 0 in the MM histogram, which is pion elastic scattering. The other energy peaks correspond to excitation levels in the ^{12}C nucleus. Nominally the correlation between channel and MeV is 100 channels/MeV [Esc 89].

Using two or more of these histograms together helped establish which peaks corresponded to which particles. If there are two large indistinguishable peaks on an ED histogram, consulting the CT histogram may provide a clue that will distinguish one peak as pions and the other a contaminant particle.

MMCT (Figure 4.4) is a two-parameter histogram of MM versus CT. The pion elastic events form a vertical line in this histogram because the pion peak is nearly centered on channel 0 in the MM histogram, while spread from about channel 0 and lower in the CT histogram. The line formed by the muon events is diagonal because the correlation between the muon energy and time of flight is different across the focal plane.

MMOP is the MM histogram subjected to several logical conditions. In the histogram setup file, MMOP has been assigned two tests based on the gates set on the CT and ED histograms. If a particle falls within the gates in CT and ED, then the particle is histogrammed in MMOP. By these tests, the particles plotted in MMOP are primarily restricted to pions.

MMOP is also correlated to MM, CT, and the data word SCPH, representing the Scruncher phase at the time of the event. If the Scruncher phase is perfectly "locked," then the Scruncher does not affect the central momentum. (At times, thermo-acoustic vibrations introduced random phase errors as large as 10°.) The resulting error in beam energy can be corrected by using the phase error signal from the RF circuit which was read and called SCPH. The correlation coefficients were

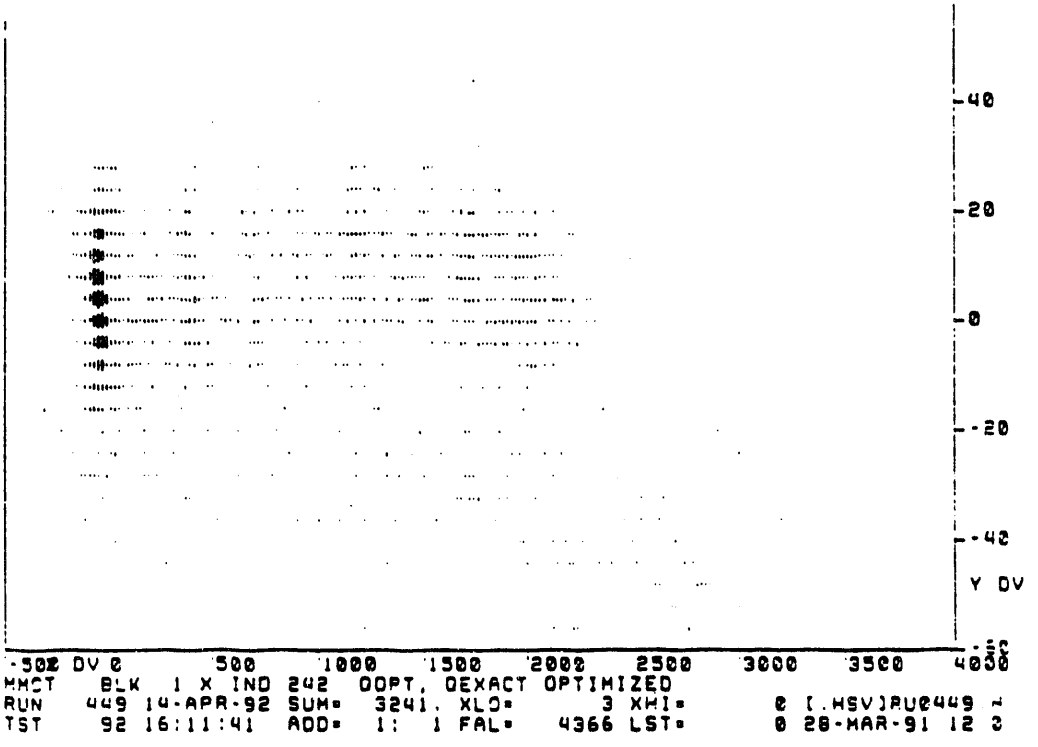

Figure 4.4: MMCT histogram for lab spectrometer angle of 60°, ^{12}C 50 MeV π^+ scattering. The vertical line is the elastic pion events, centered on 0 on the MM scale and spread about 0 and lower on the CT horizontal scale.

determined using the RAY routine discussed later. For this experiment with 50 MeV positive pions for example,

$$\text{MMOP}=(-1.87)+\text{MM}-(.795)\times\text{SCPH}-(.67)\times\text{CT}.$$

These correlations adjust the channel positions of the various peaks. Like the MM histogram, the peak in channel 0 is the elastic scattering, and the other peaks correspond to excitation levels in the ^{12}C nucleus. Comparing Figure 4.5(a) with Figure 4.5(b), in the MMOP histogram, the elastic peak is seen to be narrower, with a FWHM of about 0.44 MeV as opposed to about 0.65 MeV for the MM elastic peak, and the other peaks are better defined in the MMOP histogram.

Because of nonuniformities in the magnetic field of the Clamshell due to saturation of field lines on the pole faces, the calculated positions of the histogram peaks did not always correspond to the known positions of the energy peaks, and the ratio of channels/MeV is not necessarily 100. Using a least squares fitting routine called PWRFIT, a polynomial was found for each of the spectra that correlated the known energy values with the locations of the peaks in the fit spectra. Typical χ^2 values for these polynomial were less than one. For instance, for the 60° spectra the following polynomial with a χ^2 of 0.116 was used:

$$X = 1.65 \times 10^{-3} + 1.005 \times Y + 2.249 \times 10^{-5} \times Y^2,$$

where X is the channel number for the energy Y in MeV. Using this energy calibration scheme, all the peaks, particularly the 12.71 and the 15.11 MeV peaks, were located with certainty.

During replay, the Q-system recalculates the values of the data words event by event, taking into consideration any changes made in the software such as gate settings. A polynomial file needs to be created that is used to calculate the kinematics of the system. The calculated data words such as MM depend on the primed and

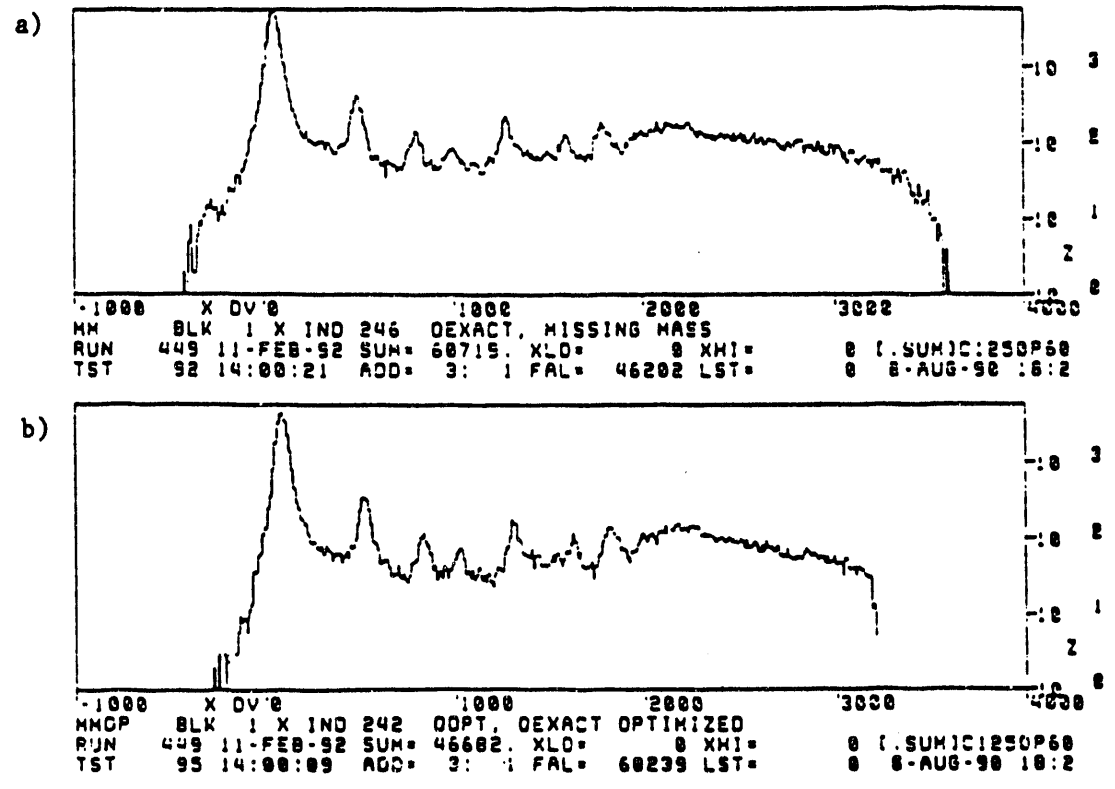

Figure 4.5: MM (a) and MMOP (b) histograms for a laboratory scattering angle of 60° for 50 MeV π^+ scattering from ^{12}C. Note the logarithmic scale. The peaks are seen more clearly in the MMOP histogram. FWHM for the elastic peak in the MM histogram is about 0.65 MeV, while FWHM for the elastic peak in the MMOP histogram is about 0.44 MeV.

unprimed variables mentioned in the last chapter. Some data words are correlated to others, as noted above. The degree of correlation between data words was determined by a program called RAY. If a correlation was suspected, RAY was invoked while replaying a run and restricting events to only elastic events. This restriction ensured that events of known energy were considered. RAY traced the path of each particle through the spectrometer, determining a ray for each particle by calculating the transport matrix M and inverting it. These matrix elements determine the path of the particle through the spectrometer by relating initial and final positions. After a number of rays have been traced (about 1000), RAY analyzed the rays and generated an output indicating the degree of correlation by creating a gaussian peak representing the calculated elastic peak. This process is repeated using fewer and fewer rays until the χ^2 comparing the calculated elastic peak and the actual run elastic peak did not change significantly. The correlation polynomial was then written into a polynomial file used by the analyzer in the kinematic calculating programs. The values of the matrix elements varied slightly from energy to energy, so this process was repeated for each beam energy used.

4.3 Peak Fitting

A fitting program called NEWFIT [Mor 90] was used to determine the areas of the peaks in the MMOP histograms. A gaussian peak shape folded with three exponential tails was fit to the elastic peak in each spectra (Figure 4.6). The peak shape obtained for the elastic peak was used as the typical, or reference, peak shape for fitting all the peaks in the spectra.

The peak shape found by NEWFIT for the elastic peak did not have a tail long enough to account for all the background in the spectra. The background

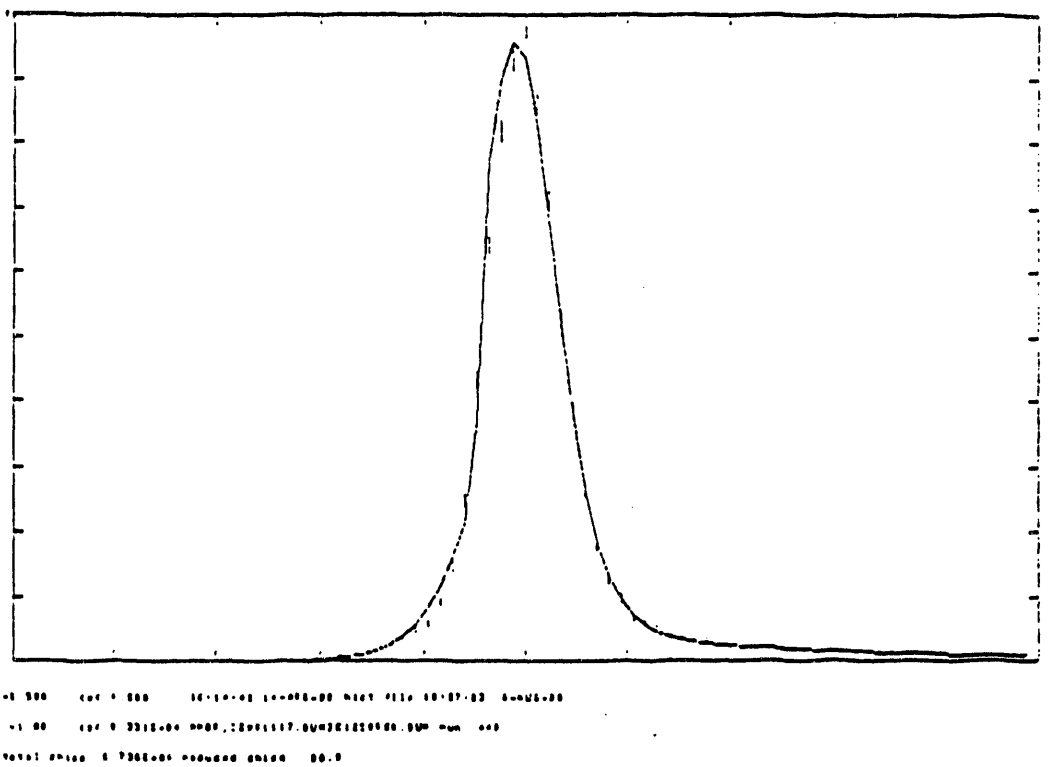

Figure 4.6: Reference peak for lab spectrometer angle of 60°, ^{12}C 50 MeV π^+ elastic scattering. FWHM for this peak is .44 MeV. The scale is from -2.5 MeV to 4.2 MeV, and each horizontal division corresponds roughly to .67 MeV.

arises from many sources, some poorly determined. Since the background shape was different for different regions of the spectra, the MMOP spectra at each angle was divided into three parts, as shown in Figure 4.7. Divisions were made between the elastic and the 4.44 MeV peaks, and the 9.65 and the 12.71 MeV peaks, since the background took on a different character in each of these regions, as shown in Figure 4.8. The elastic region had an almost negligible background, and the middle region had a monitonically decreasing background, primarily from the elastic tail. The final region had an almost constant background, due the sum of the tails of all the peaks and perhaps to excitations to the three-alpha breakup state in ^{12}C [Ajz 85].

Some consideration needed to be given to the 10.3 and the 15.4 MeV states in the ^{12}C spectrum. These two states are very broad with FWHMs of 2.5 MeV and 1.5 MeV respectively [Ajz 85]. When fit, the 10.3 MeV state was consistently found to be negligible. However the 15.4 MeV peak, a 2^+ state, has an effect on the 15.11 MeV peak and careful consideration was given to this effect. The 15.4 MeV peaks found by NEWFIT were almost negligible for scattering angles of 45°, 60°, and 75°. However, as found in previous work [Jak 90], the 15.4 MeV cross sections are consistent with those of the 4.44 MeV cross sections scaled by a factor. At the angles mentioned, the 2^+ state cross sections are at a minimum, and therefore negligible. The effects of the 15.4 MeV state are more pronounced for scattering angles of 30°, 90°, and 103°, and the Clamshell spectrometer does not have the resolution to distinctly identify the state at these angles. Therefore the only scattering angles taken into consideration when calculating the ratios of the 1^+ states are those of 45°, 60°, and 75°, where the cross sections for the 15.11 MeV state can be determined with certainty.

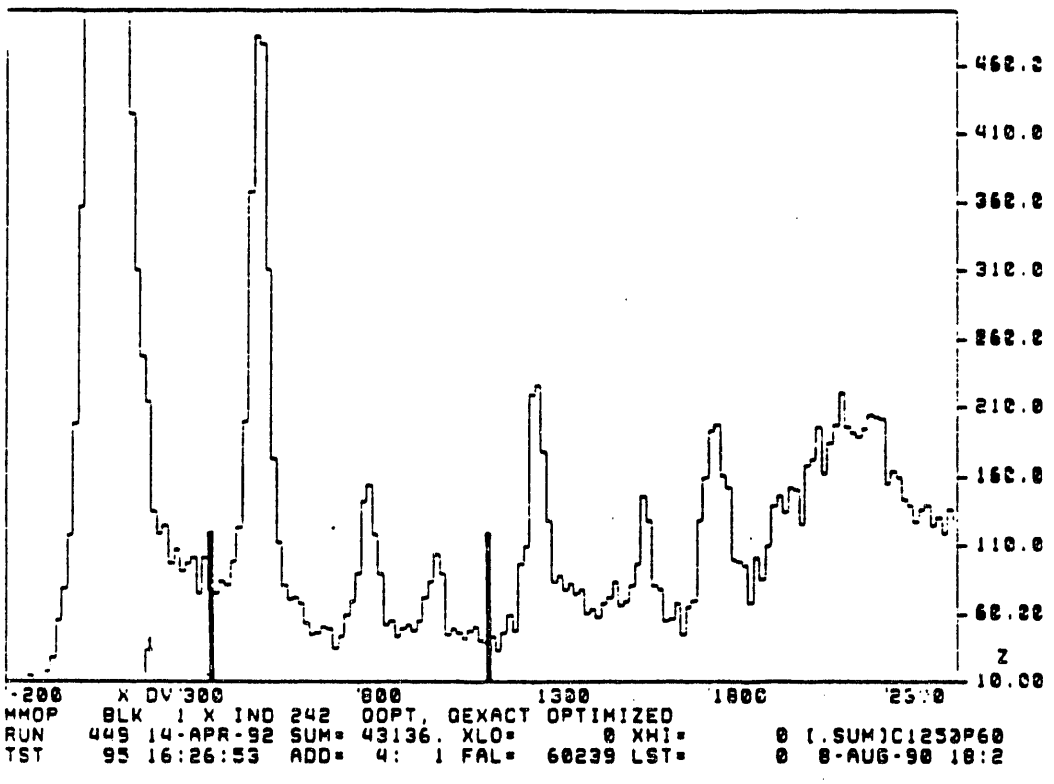

Figure 4.7: MMOP histogram for lab spectrometer angle of 60°, ^{12}C 50 MeV π^+ scattering, showing where the divisions were made in fitting the spectra.

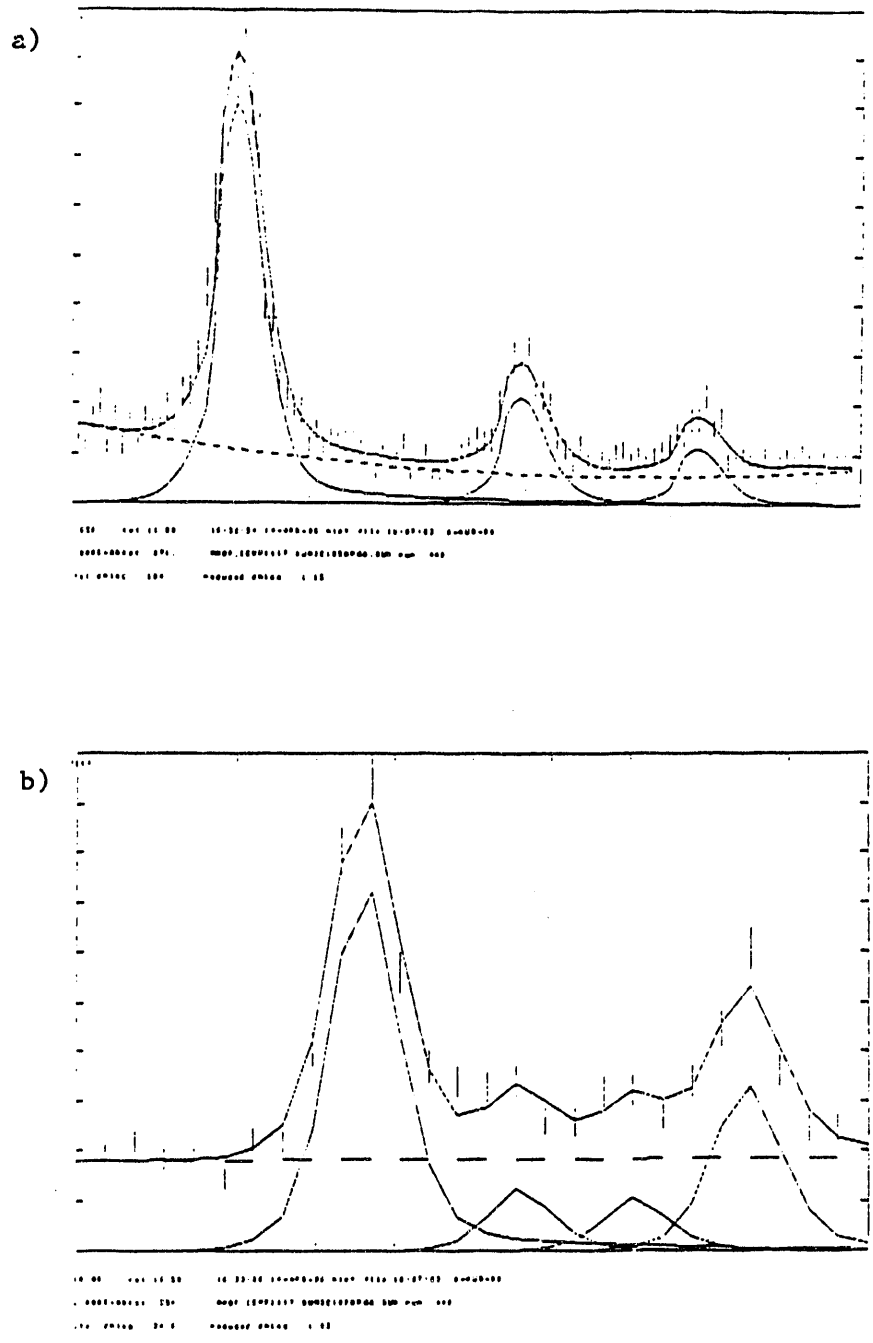

Figure 4.8: Fits of (a) second and (b) third regions of the MMOP spectra for lab spectrometer angle of 60°, ^{12}C 50 MeV π^+ scattering. The first region is the elastic peak, shown in Figure 4.7.

4.4 Analysis

The center of mass cross sections for particles scattered from a target into the Clamshell spectrometer can be expressed generally in terms of experimental variables as:

$$\frac{d\sigma}{d\Omega} = \frac{Area \cdot CF \cdot Jac \cdot \rho_{tgt} \cdot N_A}{SF \cdot \eta_{fp} \cdot \alpha d\Omega \cdot \cos\theta_{tgt} \cdot A}.$$

Area is the peak areas, or the number of counts in a peak. CF is a correction factor that contains all the information about hardware efficiencies such as computer livetime and wire chamber efficiencies. Jac is the Jacobian, which relates the solid angle $d\Omega$ in the lab to the solid angle in the center of mass. α is the number of incident pions per relative monitor count. SF is the survival fraction, a correction made for pions which enter the spectrometer but decay before reaching the target.

η_{fp} is the focal plane acceptance, a function of δ, the position of an energy peak relative to the central momentum on the spectrometer focal plane. During tune-up for the experiment, a series of runs known as a δ-scan was conducted in order to determine the efficiency across the focal plane. The magnetic field and hence the position of the central momentum of the spectrometer was varied to sweep the ^{12}C elastic peak across the focal plane from $\delta = -30\%$ to 15%. A value of η_{fp} was then calculated for each event at a different δ. η_{fp} is given by:

$$\eta_{fp} = \frac{Area}{TOR1}\frac{CF}{SF}.$$

η_{fp} is then plotted against δ and the points are fit to provide a polynomial expression for η_{fp} as a function of δ, shown in Figure 4.9.

The actual solid angle of the Clamshell $d\Omega$ and the actual number of incident pions in the LEP channel α are unknown. Therefore a normalization factor, $\alpha d\Omega$,

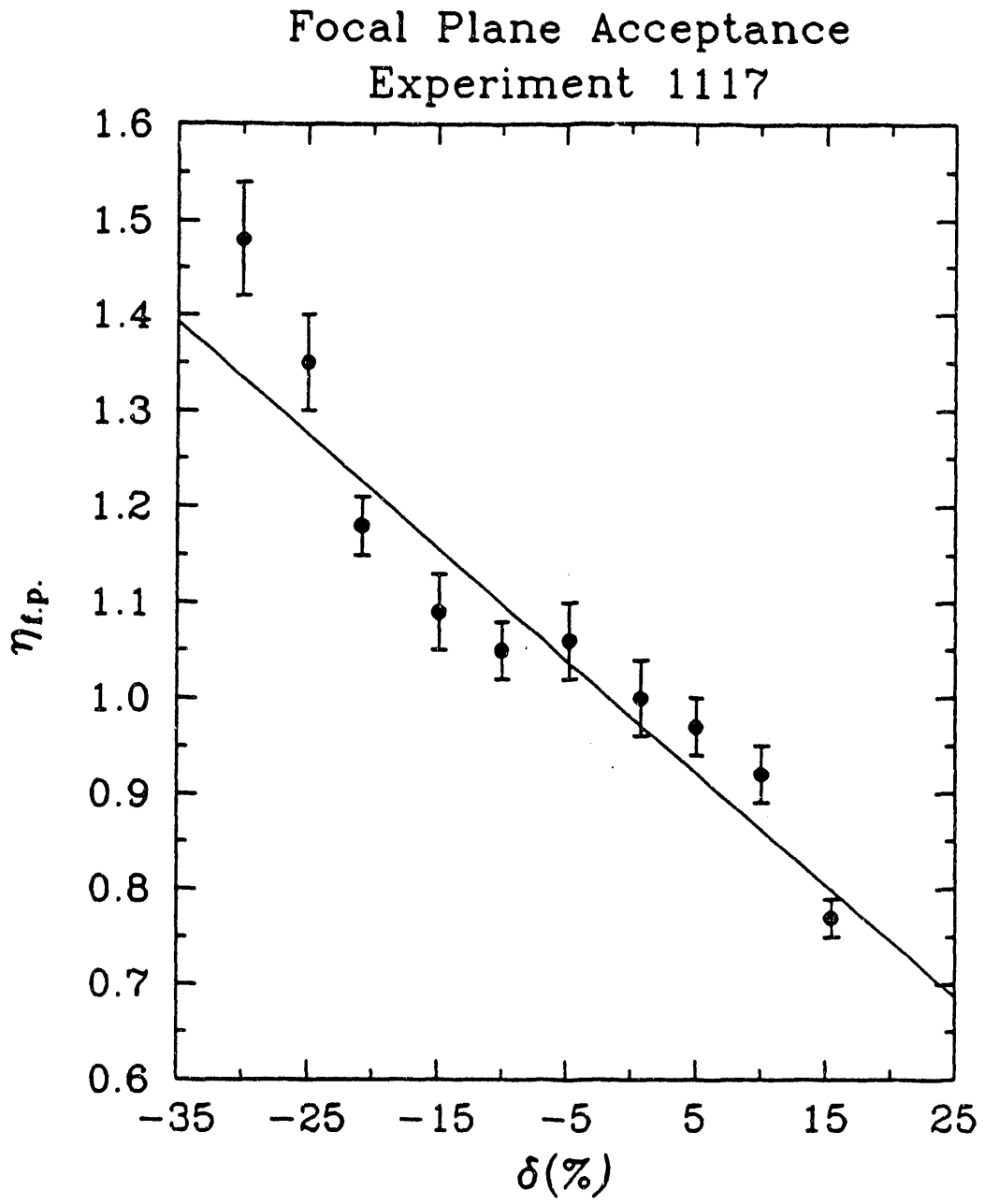

Figure 4.9: Delta-scan results for this experiment.

is required to account for these quantities. The remaining expression,

$$\frac{\rho_{tgt} \cdot N_A}{\cos\theta_{tgt} \cdot A},$$

is the number of nucleons/area in the target. N_A is Advogadro's number, A is the atomic number, and θ_{tgt} is the angle the target makes with the beam, set to one half the spectrometer scattering angle for this experiment. This target angle minimizes energy loss through particles traveling through the target material.

The values $Area, Jac, SF$, and η_{fp} are unique to each inelastic peak, but the number of target nucleons, CF, and $\alpha d\Omega$ are the same for all peaks for a given angle and energy. By taking the ratio of two peaks in the same spectra, the common factors can be eliminated. Thus, values for the differential cross sections were obtained by the following expression:

$$\left.\frac{d\sigma}{d\Omega}\right|_e = \frac{N_e}{N_o}\left.\frac{d\sigma}{d\Omega}\right|_o \frac{SF_o}{SF_e}\frac{\eta_o}{\eta_e}\frac{Jac_e}{Jac_o},$$

which is derived by taking the ratio of the cross section for a particular angle and energy, $d\sigma/d\Omega\ |_e$, to the 4.44 MeV 2^+ cross section for the same angle and energy, $d\sigma/d\Omega\ |_o$. For this work, values for the 2^+ cross sections were obtained through a least-squares fit to the experimental values of the 2^+ cross sections from Ritchie *et al.* [Rit 90] and Sobie *et al.* [Sob 84], which are in excellent agreement, as seen in Figure 4.10. These values of the 4.44 MeV cross sections for each angle were used for the absolute normalization. The total absolute normalization uncertainties are estimated to be less than 10%. The cross sections were also corrected for finite solid angle and angle bin size, using the formalism explained in detail in Escalante's thesis [Esc 89].

The uncertainty considered in the cross section calculations arose from those for the areas of the 4.44 MeV peaks and from the determination of η_{fp}, where

$$\sigma_{\eta_{fp}} = \sqrt{\sigma_a^2 + \sigma_b^2 \cdot \delta^2}.$$

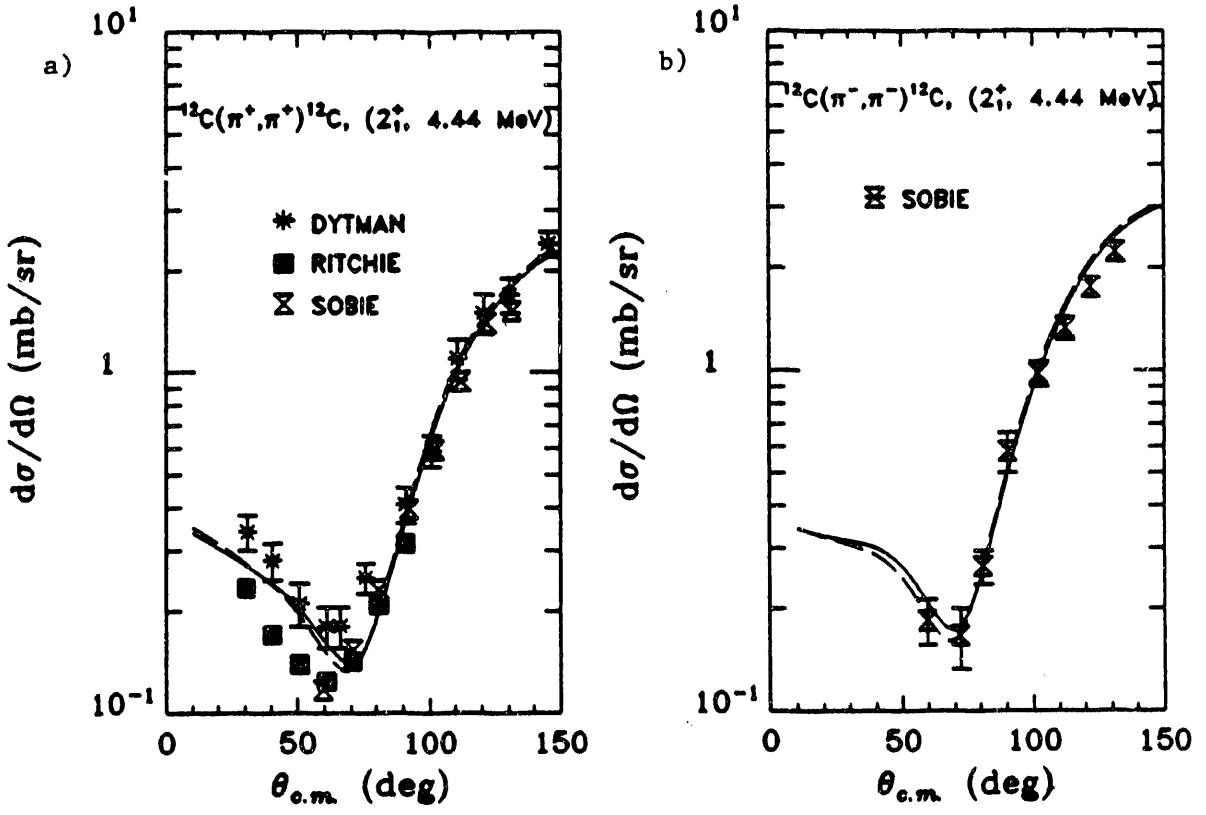

Figure 4.10: Cross sections for the excitation of the 4.44 MeV state in ^{12}C for (a) 50 MeV π^+ showing Dytman *et al.* [Dyt 79], Ritchie *et al.* [Rit 90] and Sobie *et al.* [Sob 84] data, and (b) 50 MeV π^- showing Sobie *et al.* data. The solid and dashed lines are results of theoretical calculations and are explained in the next chapter.

The quantities σ_a and σ_b are determined from the correlation matrix for the coefficients of the least squares polynomial fit determined from PWRFIT. The correlation matrix element σ_{ab} was negligible. Uncertainties in the SF and the Jac variables were also negligible. The total uncertainty in the cross section was determined by:

$$\sigma_{\frac{d\sigma}{d\Omega}} = \frac{d\sigma}{d\Omega} \cdot \sqrt{(\frac{\sigma_N}{N})^2 + (\frac{\sigma_{\eta_{fp}}}{\eta_{fp}})^2}.$$

Systematic uncertainties such as those of the areas of the elastic peaks and those of the normalizing elastic cross sections were less than 10%.

Chapter 5

Results

5.1 Introduction

The values obtained for the ^{12}C scattering cross sections are given for an incident 50 MeV π^+ beam in Table 5.1 and for an incident 50 MeV π^- beam in Table 5.2. These values are plotted in Figures 5.1-5.12 with data from experiments conducted by Dytman *et al.* [Dyt 79], Sobie *et al.* [Sob 84], Jaki *et al.* [Jak 90] and Ritchie *et al.* [Rit 88, Rit 90]. The Dytman *et al.* data have been included for completeness; however these data have been superseded by the more recent work, and detailed comparisons to that data will not be made.

The curves plotted on the $2^+, 0^+$ and 3^- figures are theoretical curves from two models. The solid line is a one-step (OS) calculation, and the dashed line is a coupled-channels (CC) calculation, both discussed in detail by Ritchie *et al.* The curves plotted on the 1^+ state figures were found using ALLWRLD [Car 81], and

θ_{lab} (deg)	Elastic (mb/sr)	4.44 MeV (mb/sr)	7.65 MeV (μb/sr)	9.64 MeV (μb/sr)	12.71 MeV (μb/sr)	15.11 MeV (μb/sr)
30.0	8.67(5)	0.222(12)	65(8)	10(6)	40(7)	-
45.0	4.52(2)	0.155(5)	31(3)	14(3)	49(3)	8(2)
60.0	2.05(1)	0.124(4)	32(2)	16(2)	55(3)	7(2)
75.0	3.19(2)	0.167(6)	45(3)	35(3)	51(4)	8(3)
90.0	4.68(2)	0.321(5)	59(3)	75(3)	26(2)	-
103.0	5.86(2)	0.573(9)	81(5)	141(5)	20(4)	-

Table 5.1: Cross sections for π^+ scattering from ^{12}C at 50 MeV.

θ_{lab} (deg)	Elastic (mb/sr)	4.44 MeV (mb/sr)	7.65 MeV (μb/sr)	9.64 MeV (μb/sr)	12.71 MeV (μb/sr)	15.11 MeV (μb/sr)
60.0	3.28(3)	0.193(9)	32(4)	24(4)	57(5)	15(5)
90.0	5.98(6)	0.488(19)	64(10)	133(11)	-	-
103.0	8.76(5)	0.942(17)	91(8)	251(10)	-	-

Table 5.2: Cross sections for π^- scattering from ^{12}C at 50 MeV.

normalized to the data from this experiment by a factor of 0.1066. The ALLWRLD routine determines cross sections using the Born approximation.

5.2 Results for Collective Transitions

For 50 MeV π^+ elastic scattering, as shown in Figure 5.1, the data from this experiment is in agreement with Ritchie *et al.* and Sobie *et al.* except for this 60° point which appears considerably low. All data follow the trend of the theoretical predictions as do those of Ritchie *et al.* and Sobie *et al.*

For 50 MeV π^+ scattering exciting the 2^+ level at 4.44 MeV, as shown in Figure 5.2, the data from this experiment are in agreement with that of Ritchie *et al.* at all spectrometer angles, which is expected since these data were normalized to the Ritchie *et al.* and Sobie *et al.* 4.44 MeV cross sections. These cross sections are slightly higher than that of Jaki *et al.*, but the angular dependence indicated by the Jaki *et al.* data are consistent with that from this experiment. However, this angular dependence is steeper at forward angles than that suggested by the theoretical curves.

For 50 MeV π^+ scattering exciting the 0^+ level at 7.65 MeV, as shown in Figure 5.3, the data from this experiment are in agreement with that of Ritchie *et al.* at all spectrometer angles. The trend suggested by the Ritchie *et al.* data are

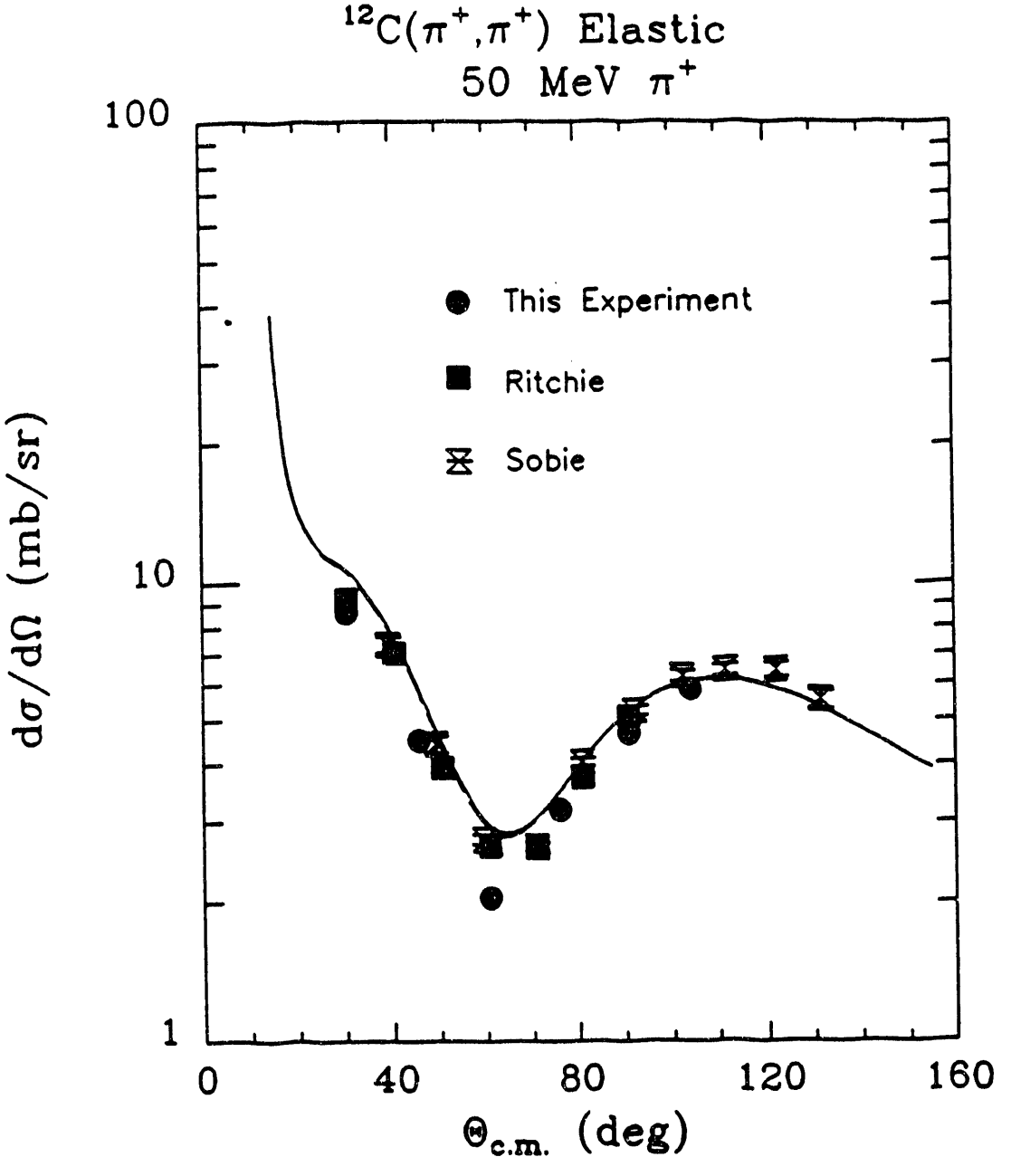

Figure 5.1: π^+ scattering elastic differential cross sections for ^{12}C at 50 MeV. Data are from this work and that of Ritchie *et al.* [Rit 90] and Sobie *et al.* [Sob 84]. The solid line indicates the result of a one-step calculation, which is indistinguishable from the coupled-channels calculation, both of which are explained in detail in Ritchie *et al.*

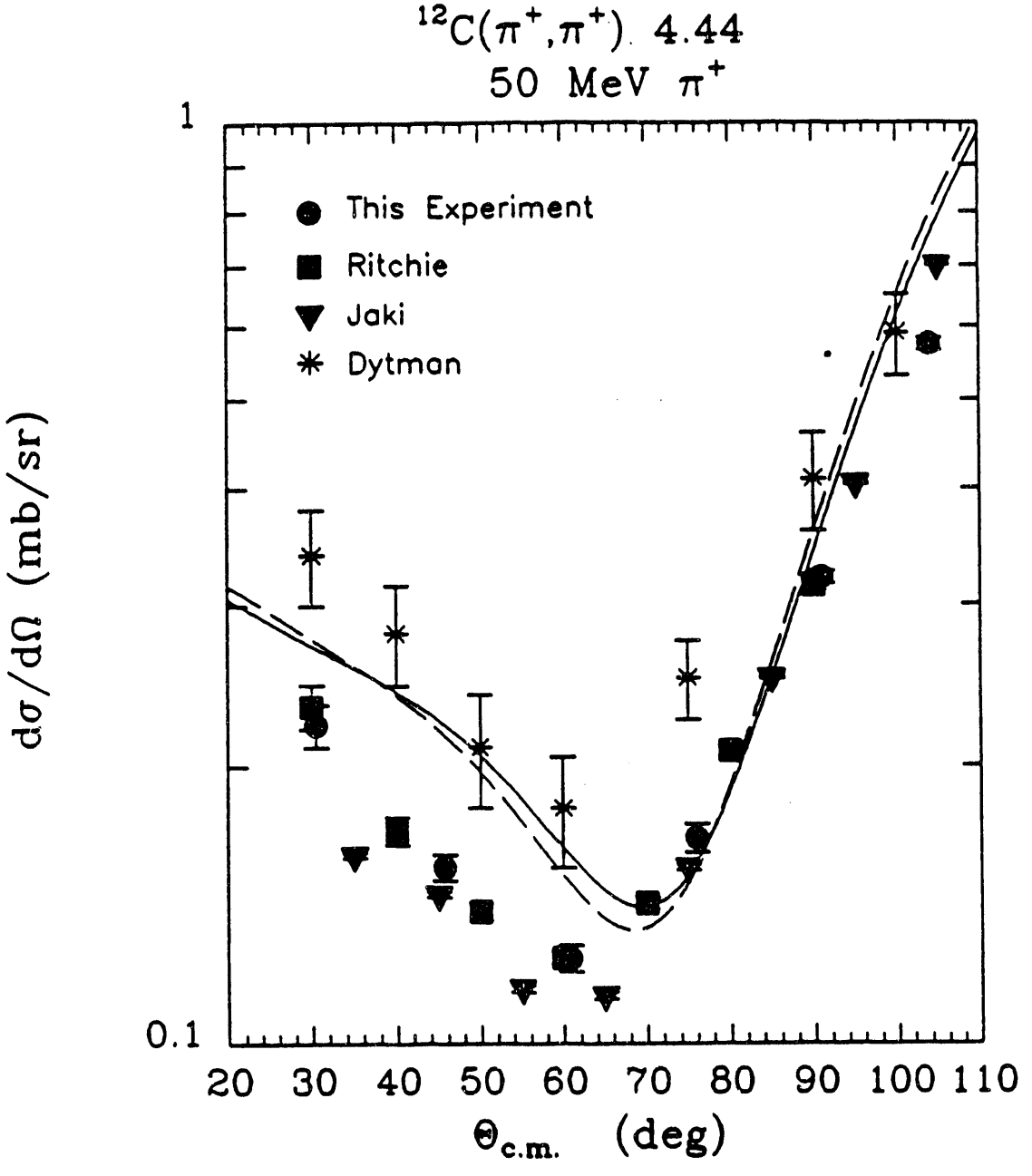

Figure 5.2: 4.44 MeV 2^+ differential cross sections for π^+ scattering from ^{12}C at 50 MeV. Data are from this work and that of Dytman *et al.* [Dyt 79], Jaki *et al.* [Jak 90] and Ritchie *et al.* [Rit 90]. The solid line indicates the result of a one-step calculation, and the dotted line indicates the results of a coupled-channels calculation, both of which are explained in detail in Ritchie *et al.*

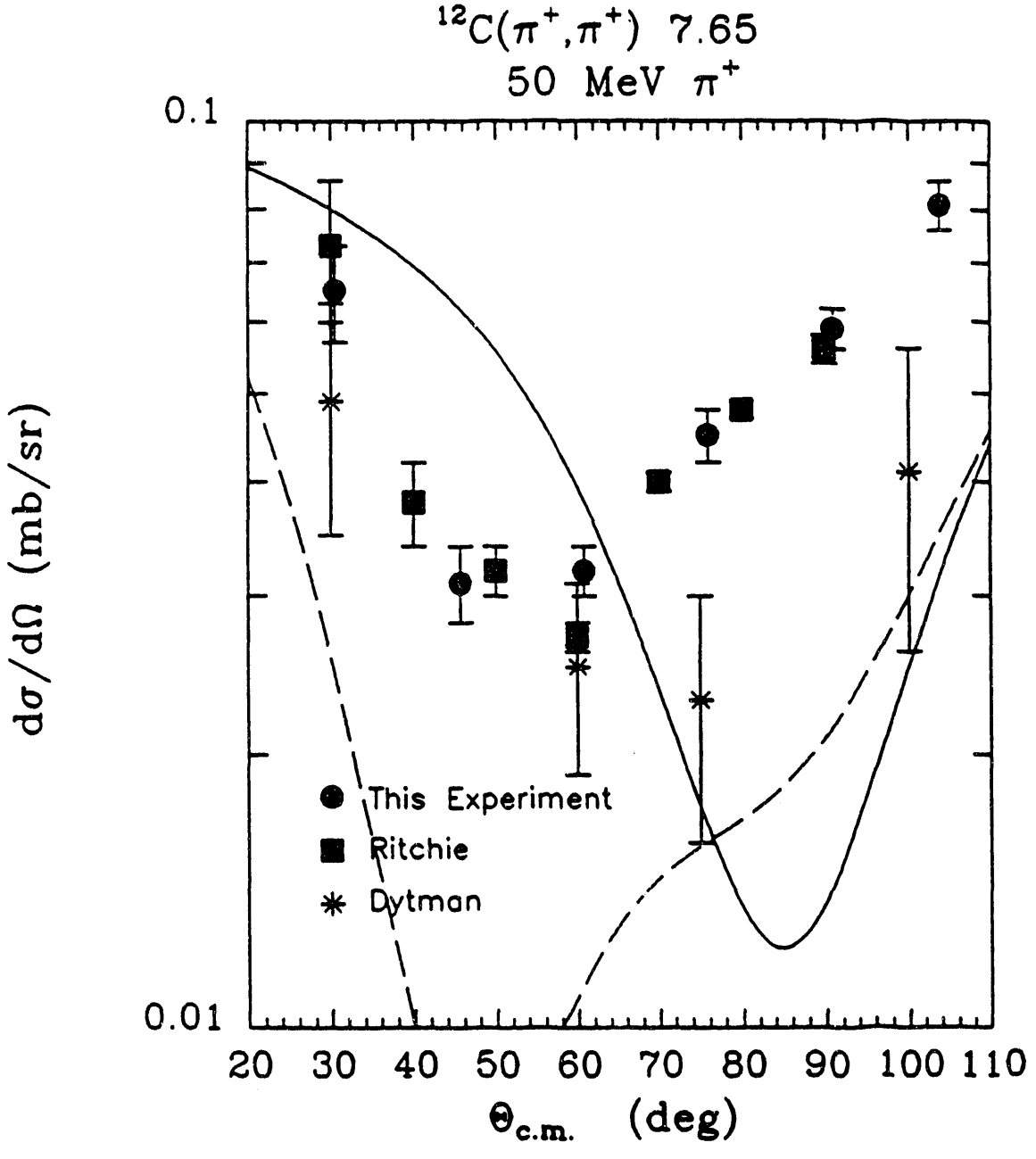

Figure 5.3: 7.65 MeV 0^+ differential cross sections for π^+ scattering from ^{12}C at 50 MeV. Data are from this work, Dytman *et al.* [Dyt 79] and Ritchie *et al.* [Rit 90]. The solid line indicates the result of a one-step calculation, and the dotted line indicates the results of a coupled-channels calculation, both of which are explained in detail in Ritchie *et al.*

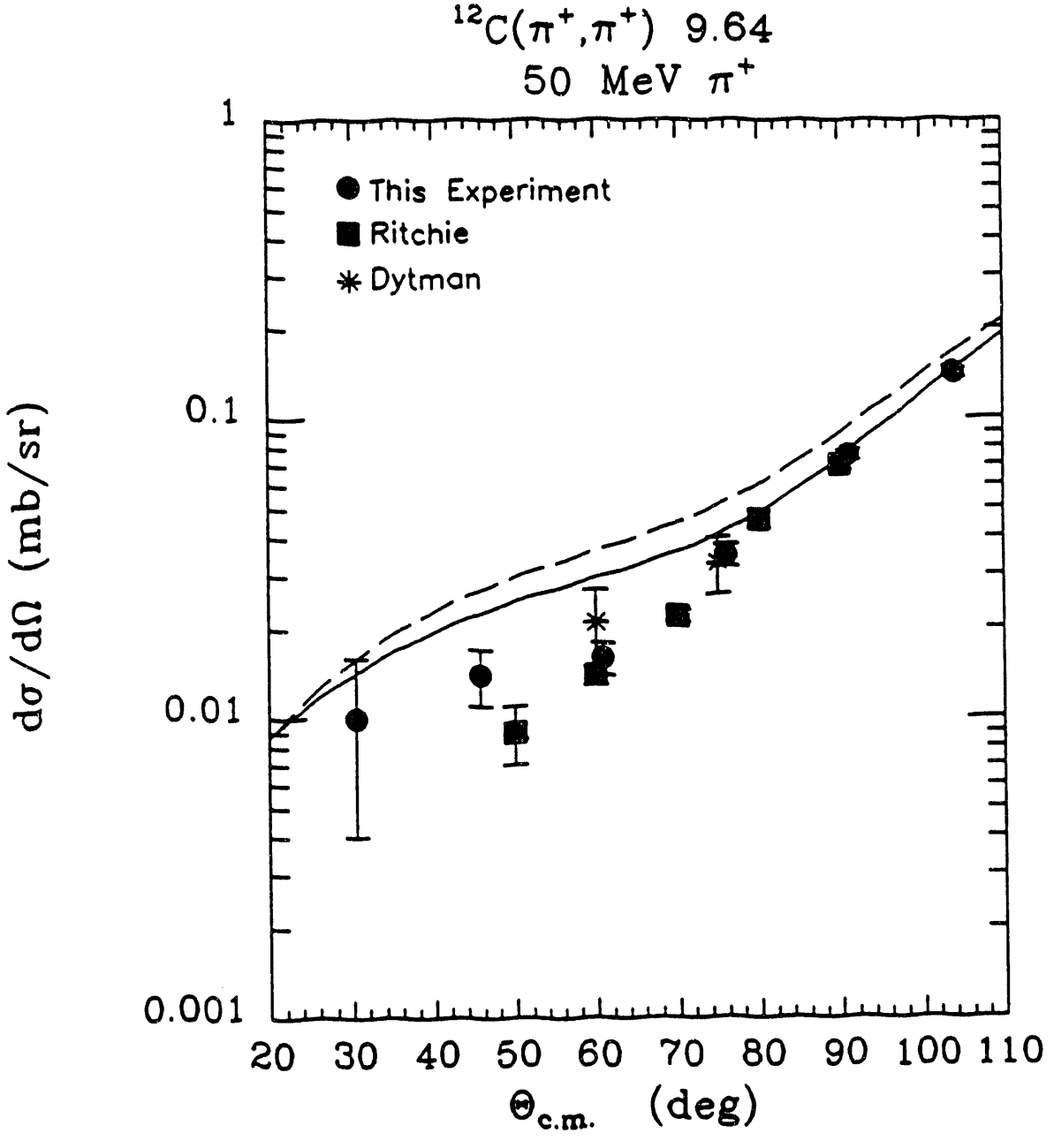

Figure 5.4: 9.64 MeV 3^- differential cross sections for π^+ scattering from ^{12}C at 50 MeV. Data are from this work, Dytman *et al.* [Dyt 79] and Ritchie *et al.* [Rit 90]. The solid line indicates the result of the one-step calculation, and the dotted line indicates the results of the coupled-channels calculation, both of which are explained in detail in Ritchie *et al.*

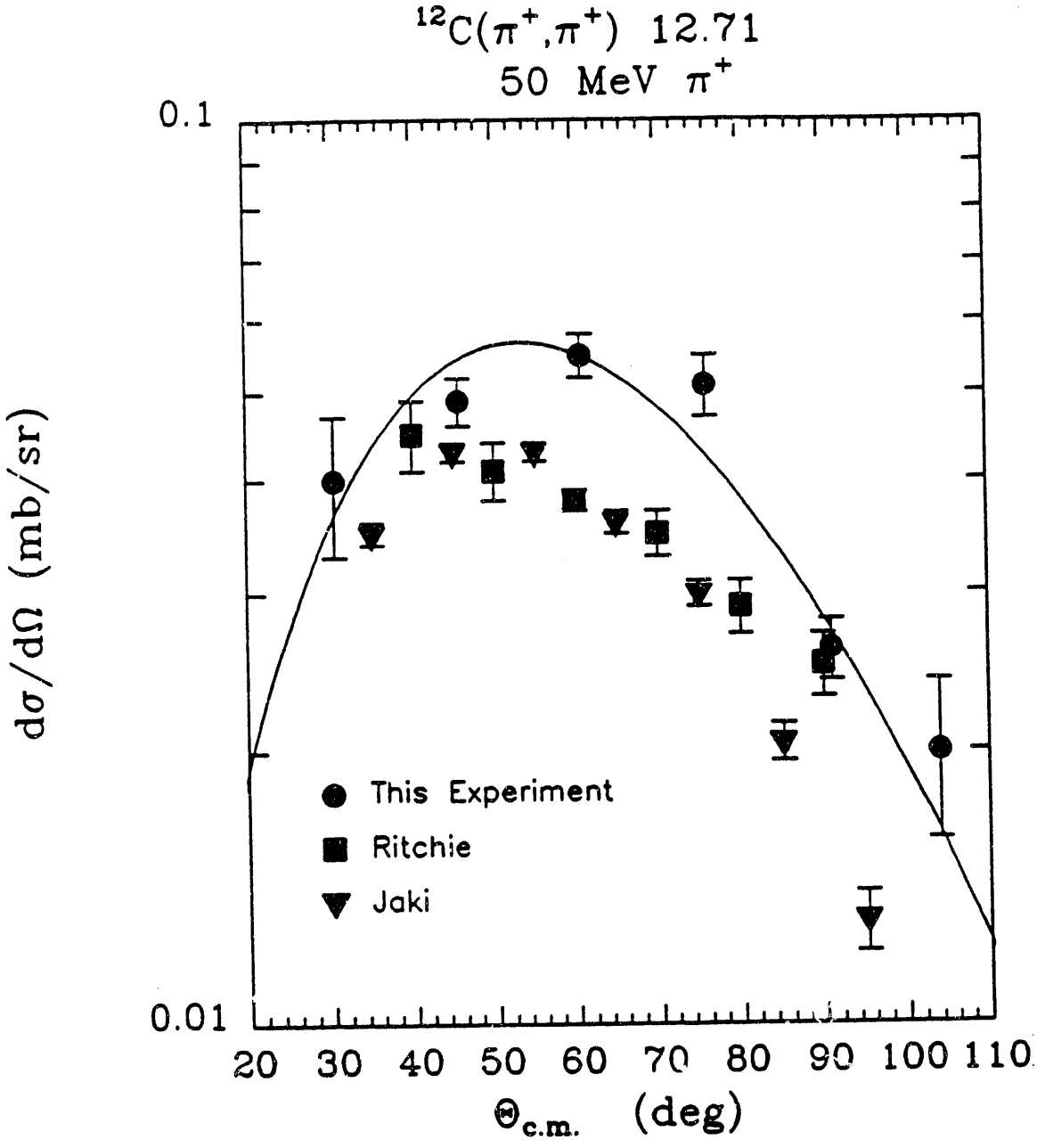

Figure 5.5: 12.71 MeV 1^+ differential cross sections for π^+ scattering from ^{12}C at 50 MeV. Data are from this work and that of Jaki *et al.* [Jak 90] and Ritchie *et al.* [Rit 90]. The solid line indicates the result of the ALLWORLD calculation explained in the text.

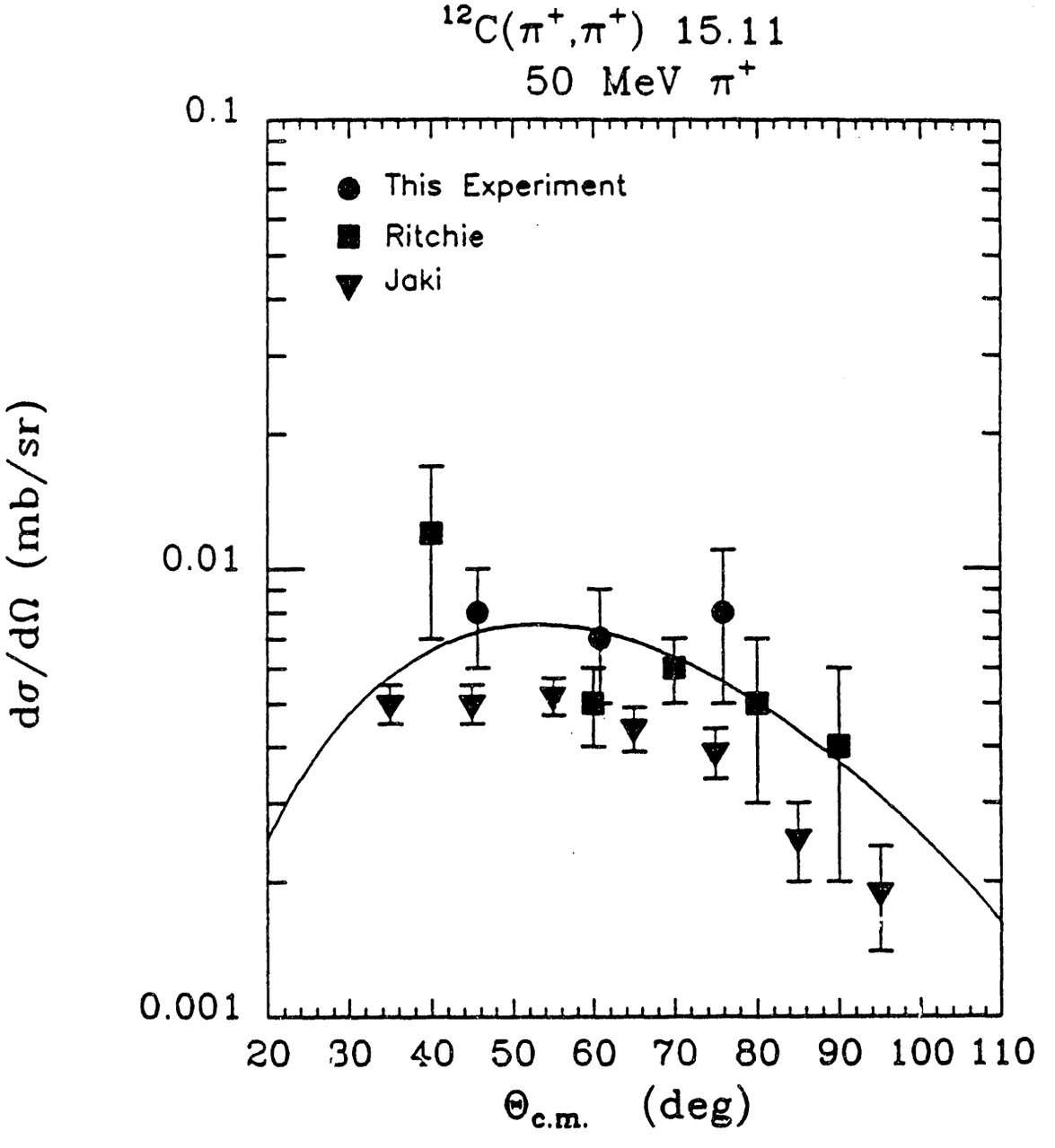

Figure 5.6: 15.11 MeV 1^+ differential cross sections for π^+ scattering from ^{12}C at 50 MeV. Data are from this work and that of Jaki *et al.* [Jak 90] and Ritchie *et al.* [Rit 90]. The solid line indicates the result of the ALLWORLD calculation explained in the text.

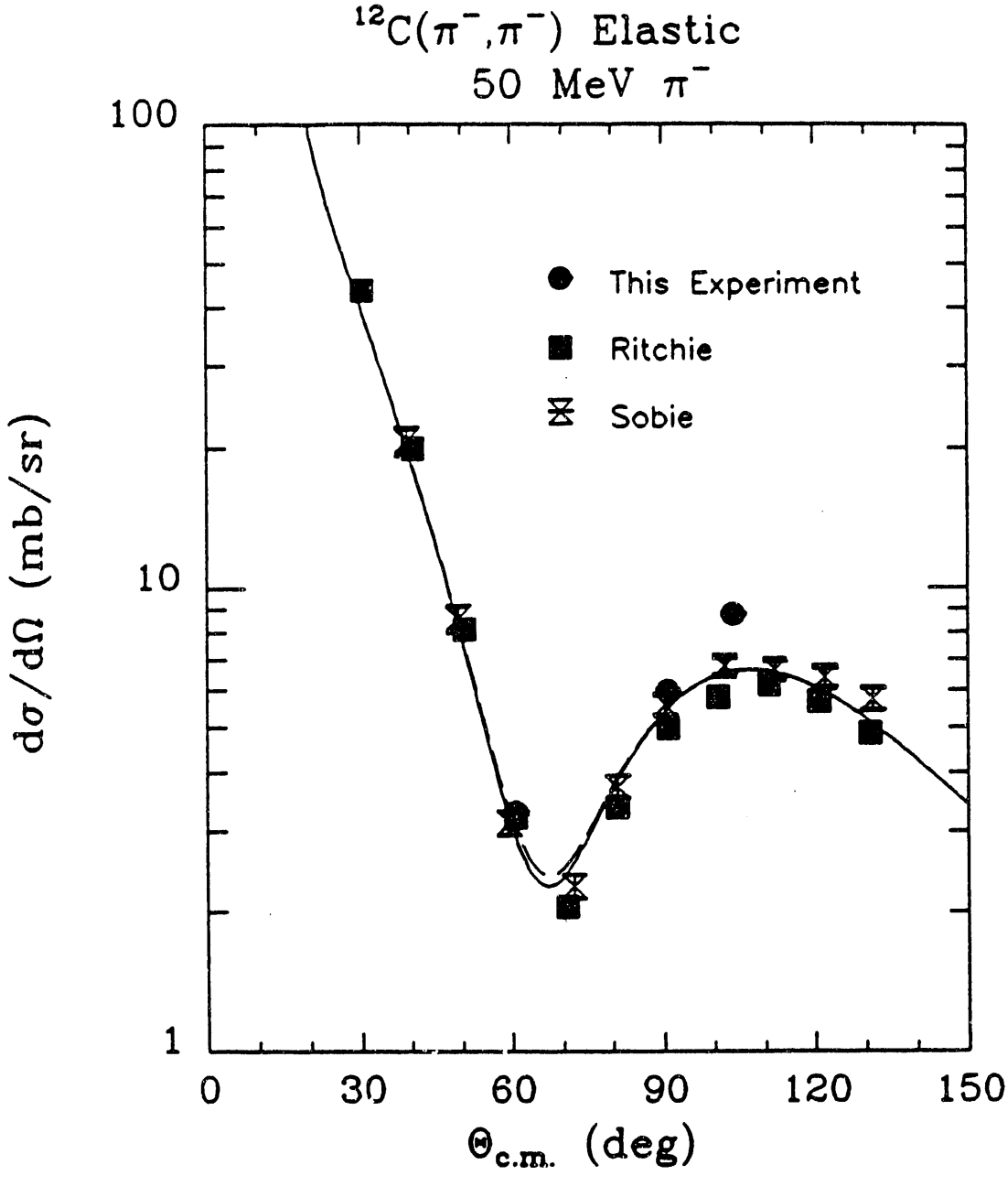

Figure 5.7: π^- scattering elastic differential cross sections for ^{12}C at 50 MeV. Data are from this work and that of Ritchie *et al.* [Rit 90] and Sobie *et al.* [Sob 84]. The solid line indicates the result of a one-step calculation, which is indistinguishable from the coupled-channels calculation, both of which are explained in detail in Ritchie *et al.*

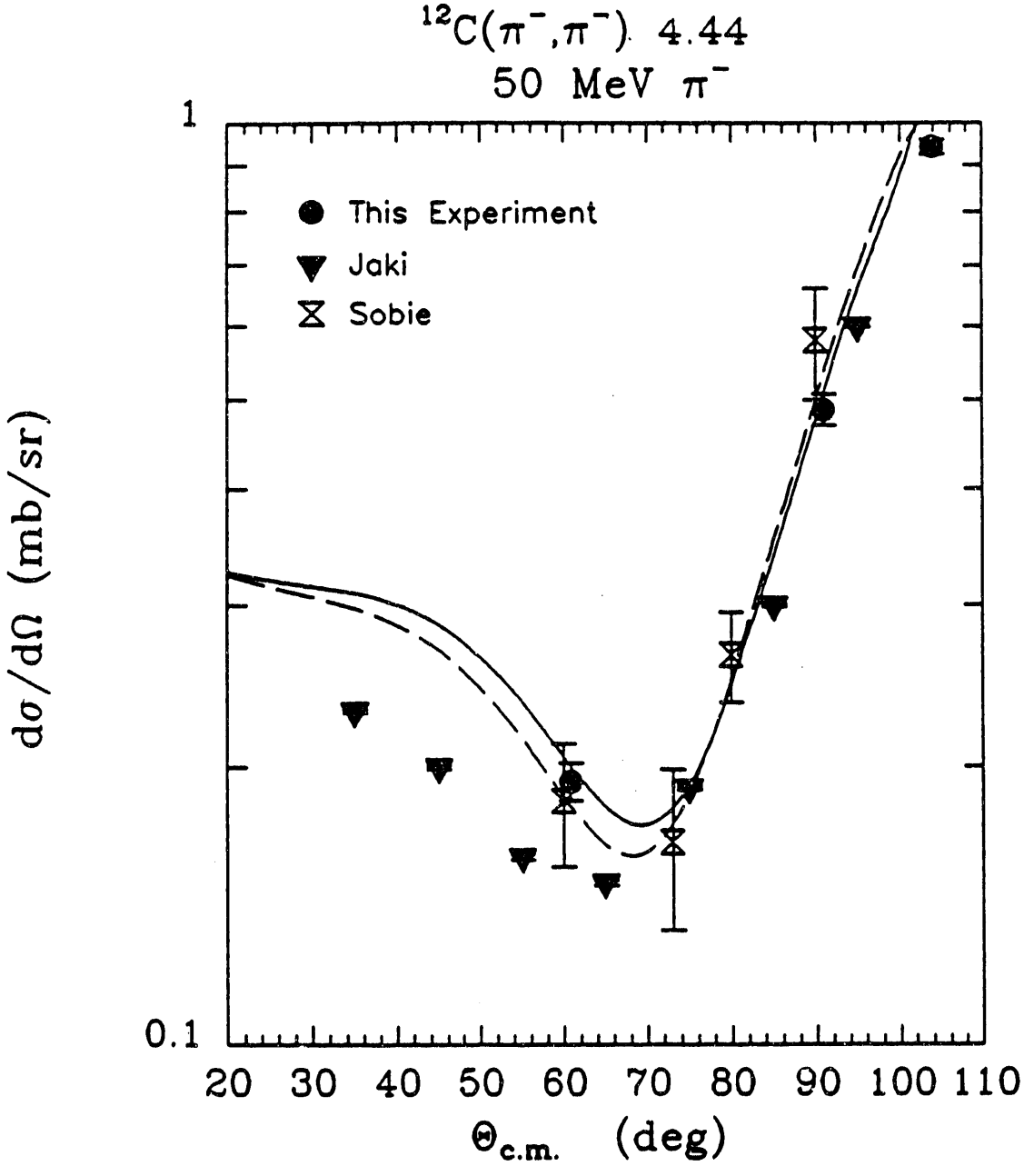

Figure 5.8: 4.44 MeV 2^+ differential cross sections for π^- scattering from ^{12}C at 50 MeV. Data are from this work and that of Sobie *et al.* [Sob 84] and Jaki *et al.* [Jak 90]. The solid line indicates the result of the one-step calculation, and the dotted line indicates the results of the coupled-channels calculation, both of which are explained in detail in Ritchie *et al.* [Rit 90].

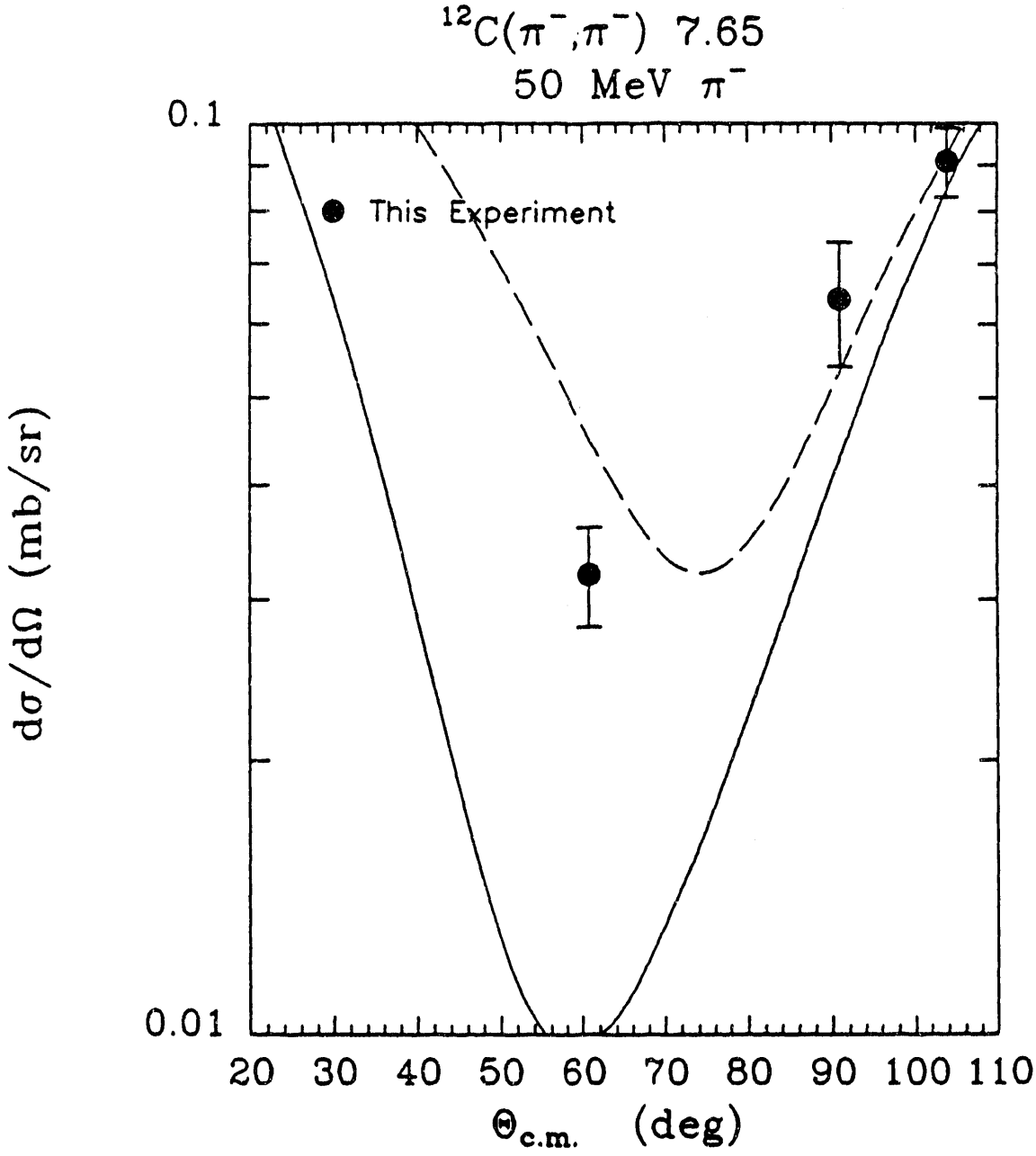

Figure 5.9: 7.65 MeV 0^+ differential cross sections for π^- scattering from ^{12}C at 50 MeV. Data are from this work. The solid line indicates the result of the one-step calculation, and the dotted line indicates the results of the coupled-channels calculation, both of which are explained in detail in Ritchie *et al.* [Rit 90].

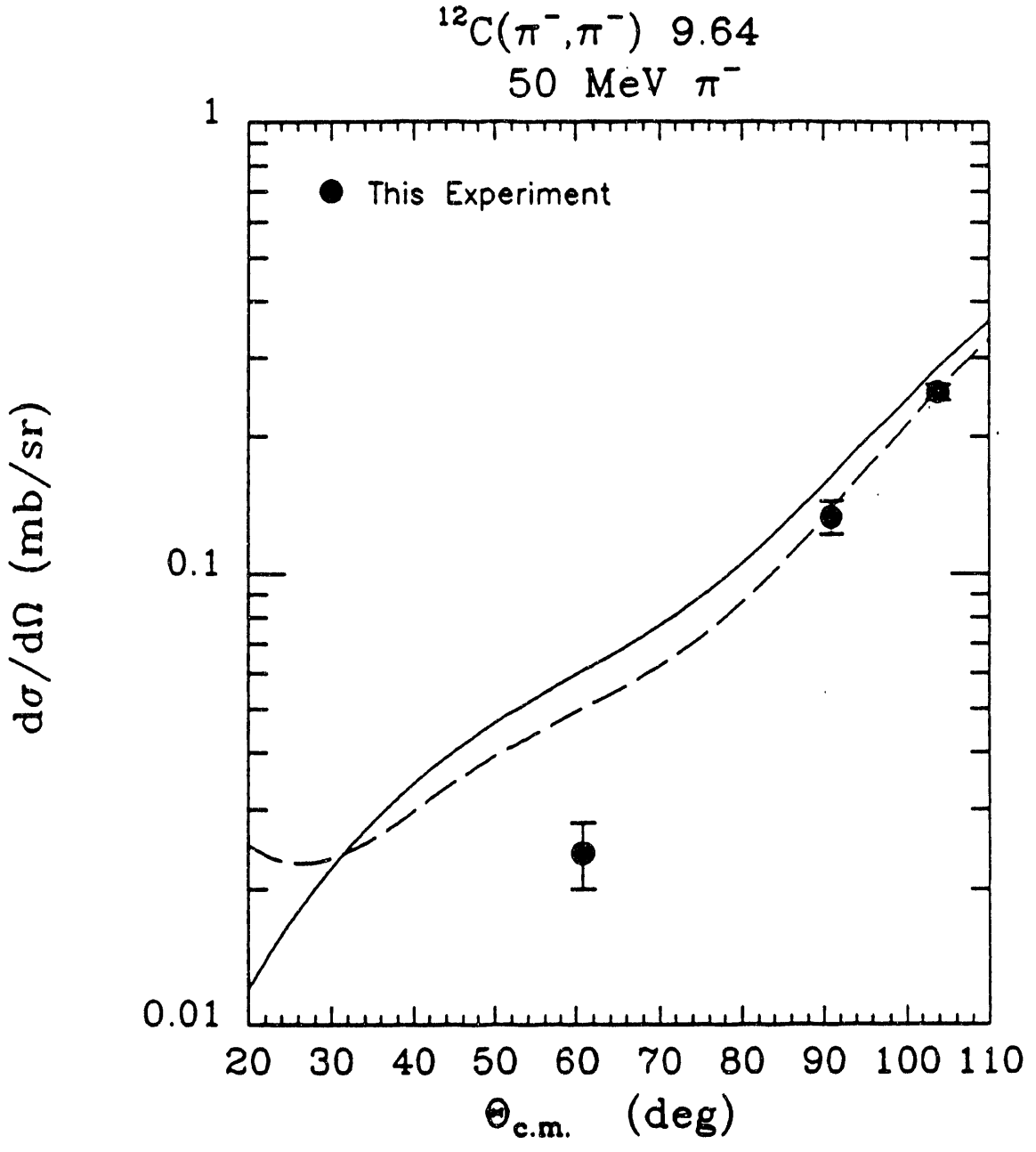

Figure 5.10: 9.64 MeV 3^- differential cross sections for π^- scattering from ^{12}C at 50 MeV. Data are from this work. The solid line indicates the result of the one-step calculation, and the dotted line indicates the results of the coupled-channels calculation, both of which are explained in detail in Ritchie *et al.* [Rit 90].

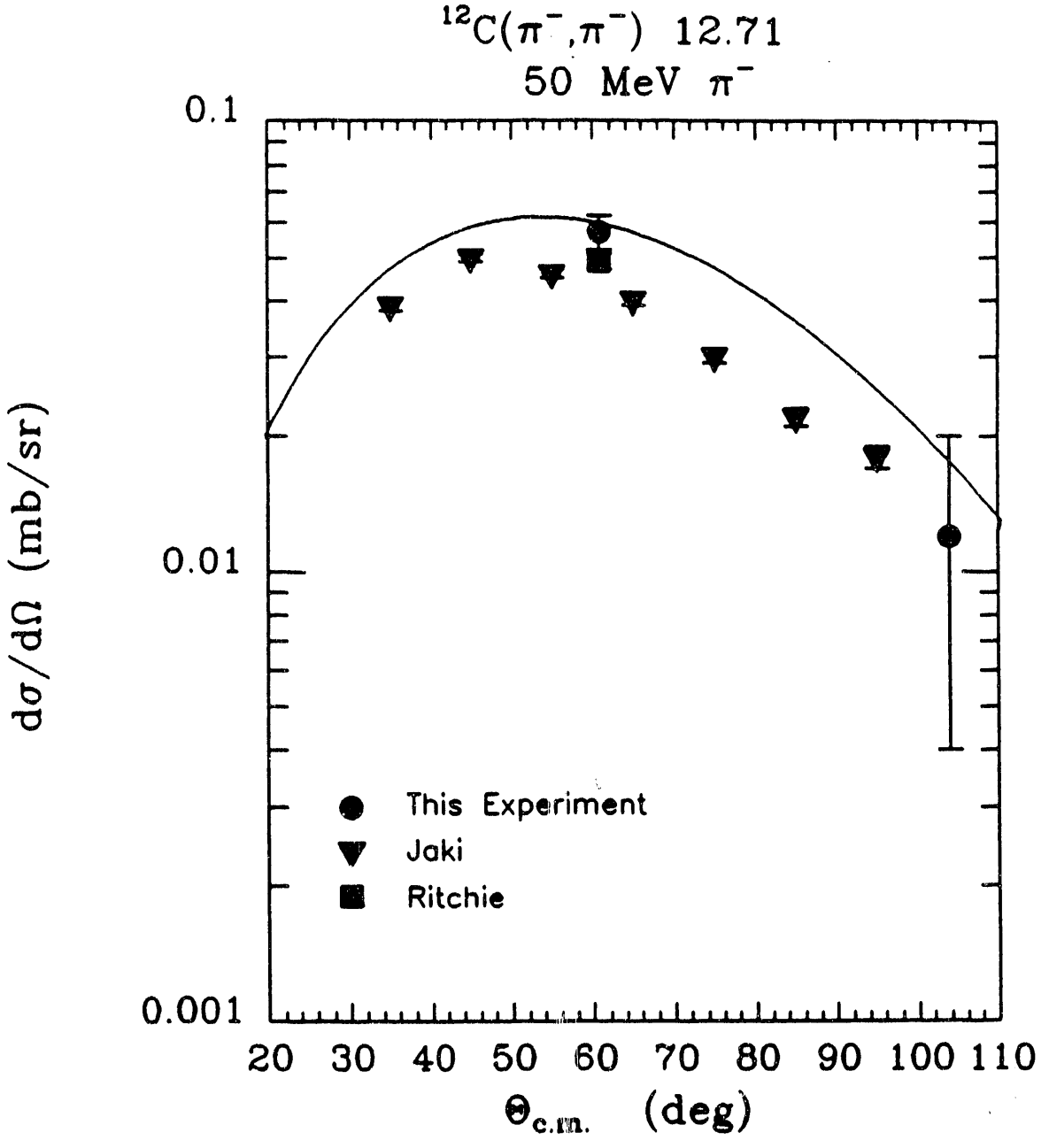

Figure 5.11: 12.71 MeV 1^+ differential cross sections for π^- scattering from ^{12}C at 50 MeV. Data are from this work and that of Jaki *et al.* [Jak 90] and Ritchie *et al.* [Rit 88]. The solid line indicates the result of the ALLWORLD calculation explained in the text.

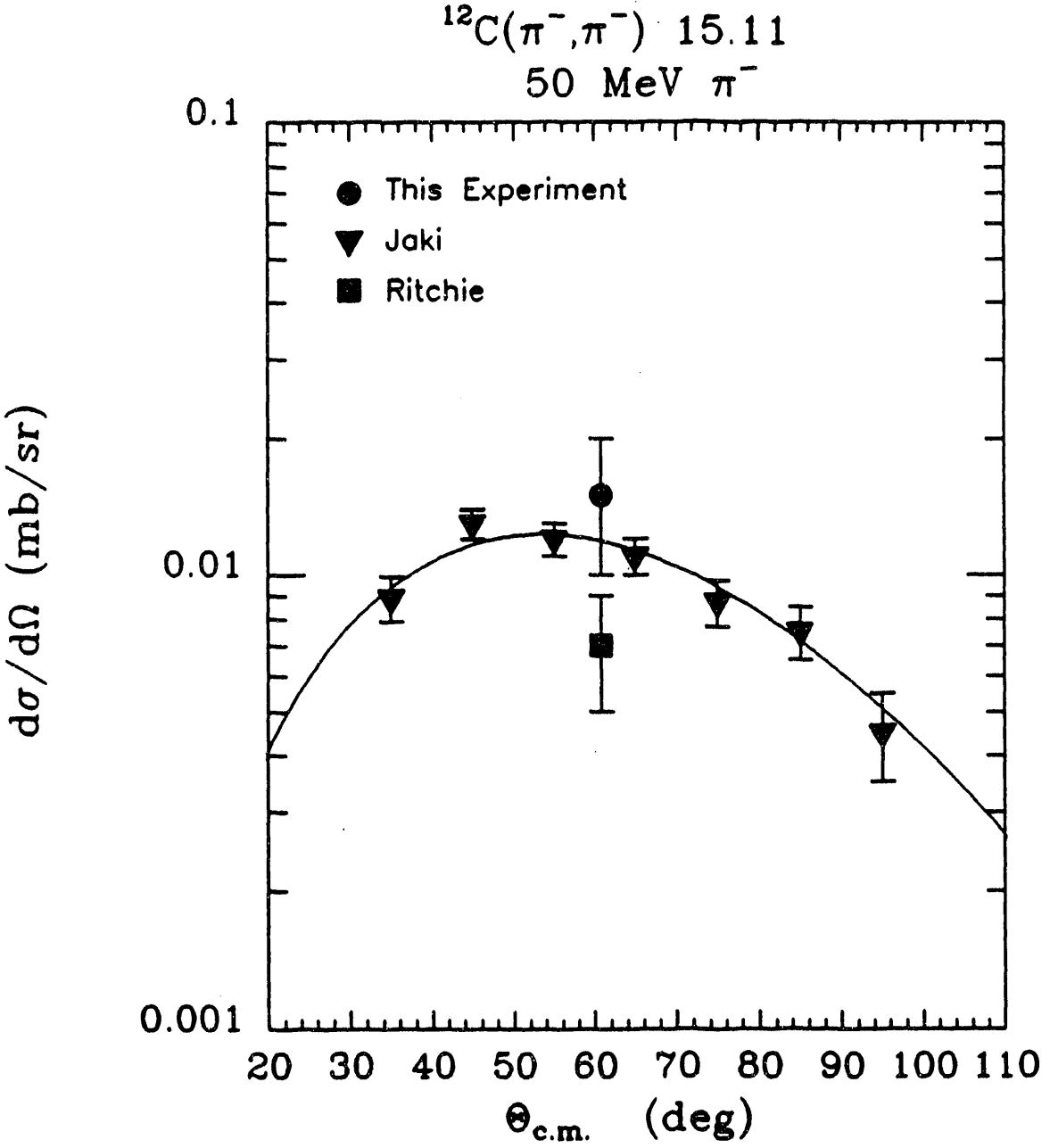

Figure 5.12: 15.11 MeV 1^+ differential cross sections for π^- scattering from ^{12}C at 50 MeV. Data are from this work and that of Jaki *et al.* [Jak 90] and Ritchie *et al.* [Rit 88]. The solid line indicates the result of the ALLWORLD calculation explained in the text.

consistent with the one suggested by the data of this experiment. Neither calculated theoretical trend for this state coincides with any of the experimental data, possibly due to pronounced effects of coupling through the first excited state [Whi 89].

For excitation of the 9.65 MeV level, as shown in Figure 5.4, the data from this experiment are in agreement with that of Ritchie *et al.* for back angles, and slightly higher for forward angles. The Ritchie *et al.* data suggests a slightly different angular dependence than that of this experiment, while the shape suggested by the data from this experiment follows closely that of the theoretical curves.

For 50 MeV π^- elastic scattering, as shown in Figure 5.7, the data from this experiment is in agreement with Ritchie *et al.* and Sobie *et al.* except for this 103° point, which is about 30% high. These data generally follow the trend of the theoretical curve, as do those of Ritchie *et al.* and Sobie *et al.*

For 50 MeV π^- scattering exciting the 2^+ level at 4.44 Mev, as shown in Figure 5.8, the data from this experiment are generally in agreement with Jaki *et al.*, but higher for 60°. The data from this experiment are also in agreement with data taken by Sobie *et al.*, as expected because of the absolute normalization to previous 4.44 MeV state cross sections. The data from this experiment follows the shape of the theoretical curve, as does that Sobie *et al.* The trend suggested by the data of Jaki *et al.* is steeper at forward angles than the theoretical curve.

This experiment was the first to determine cross sections for π^- scattering exciting the 0^+ state at 7.65 MeV. As shown in Figure 5.9, neither theoretical curve describes the data for this state, as was the case for π^+, though the CC calculation approximates the data better than the OS calculation.

The data obtained here for the 9.64 MeV state are in general agreement with the CC theoretical curve for excitation by π^- scattering, as shown in Figure 5.10.

5.3 Results for the 1^+ Doublet in ^{12}C

For 50 MeV π^+ scattering exciting the 1^+ level at 12.71 MeV, as shown in Figure 5.5, the data from this experiment are generally higher than those of Ritchie *et al.* and Jaki *et al.*, especially at spectrometer angles of 60° and 75°, which are high by about 80%. The shapes depicted by the Jaki *et al.* and Ritchie *et al.* data are not as steep as that suggested by these data or the theoretical curve. However, data from this experiment are in reasonable agreement with the normalized theoretical curve.

For 50 MeV π^+ scattering exciting the 1^+ level at 15.11 MeV, as shown in Figure 5.6, the data from this experiment are again higher than that of Jaki *et al.*, though in agreement within uncertainties with that of Ritchie *et al.* Data from Jaki *et al.* follow the shape of the theoretical curve, as does the data from this experiment and Ritchie *et al.*

For 50 MeV π^- scattering exciting the 1^+ levels at 12.71 MeV, as shown in Figure 5.11, the data from this experiment are in agreement with that of Jaki *et al.* and Ritchie *et al.* [Rit 88] and both sets of data agree with the theoretical curves.

For 50 MeV π^- scattering exciting the 1^+ level at 15.11 MeV, as shown in Figure 5.12, the data from this experiment agree with that of Jaki *et al.*, though higher than that of Ritchie *et al.* Data from Jaki *et al.* follow the shape of the theoretical curve as does the data from this experiment.

5.4 Determination of the Isospin Mixing Matrix Element

Using the present data, for π^+ reactions the ratios R^+ of 12.71 to 15.11 MeV cross sections were obtained for 45°, 60° and 75°. The R^+ values are $6.1 \pm 1.9, 7.4 \pm 1.8$ and 6.4 ± 2.7, respectively. A weighted average of these three ratios gives an average

Ratio	This Experiment	Jaki *et al.*	Ritchie *et al.*
R^+	6.8(13)	7.9(13)	7.5(15)
R^-	3.9(14)	3.8(7)	6.6(15)
R^2	1.7(7)	2.1(4)	1.1(3)

Table 5.3: Calculated cross section ratios (as discussed in the text) from this work, Jaki *et al.* [Jak 90] and Ritchie *et al.* [Rit 90].

R^+ of 6.8 ± 1.3. For π^- reactions the ratio R^- could only be calculated for 60°, and is 3.9 ± 1.4. In the notation of the theory chapter, $R^+ = \sigma_A^{\pi^+}/\sigma_B^{\pi^+}$ and $R^- = \sigma_A^{\pi^-}/\sigma_B^{\pi^-}$. The ratio $R^2 = R^+/R^-$ was found to be 1.7 ± 0.7. Table 5.3 compares values of R^+, R^- and R^2 with those of Jaki *et al.* and Ritchie *et al.*

Since we have three equations ($\alpha^2 + \beta^2 = 1$ and Equations 2.6 and 2.7) with three unknowns (χ, α, and β) we can solve numerically for χ without having to make an approximation. In this manner, the Statistical Package for Social Sciences for the Personal Computer (SPSS/PC) was used to find χ [SPS 89]; a value for χ of 2.60 ± 0.11 was obtained. This value of χ yields values of 0.9988 ± 0.2797 and 0.0497 ± 0.0139 for α and β, respectively. Ritchie *et al.* previously numerically obtained a value for χ of $2.21 \pm .16$ for 50 MeV π^+ and π^-.

Using the SAID formalism [Arn 85] and Equation 2.5, we can obtain theoretical values for the phase shift amplitudes in the impulse approximation and thus for χ, and find that χ should be 2.85, which is in good agreement with the experimental value obtained numerically.

The isospin mixing matrix element was found in terms of α and β in Equation 2.8. Using E_A=12.71 MeV, E_B=15.11 MeV and the values of α and β obtained from the numerical solution,

$$\mathcal{H}_{01} = 119 \pm 40 \text{ keV}.$$

Experiment	β	$\mathcal{H}_{01}$ (keV)
This Experiment	0.050(13)	119(40)
Morris *et al.*	0.062(12)	148(29)
Ritchie *et al.*	0.010(23)	25(58)
Jaki *et al.*	0.065(15)	157(35)

Table 5.4: Values of $\mathcal{H}_{01}$ deduced from pion scattering experiments. Results include this work and those of Morris *et al.* [Mor 81], Jaki *et al.* [Jak 90] and Ritchie *at al.* [Rit 90].

Experimental values of $\mathcal{H}_{01}$ and β for this and other experiments are given in Table 5.4. The value from this experiment is in good agreement with that of Morris *et al.* and Jaki *et al.*, and disagrees with that of Ritchie *et al.*, though overlapping the latter value with its large uncertainty.

Measurements of $\mathcal{H}_{01}$ with hadronic probes other than pions are generally inconsistent with each other, with values of 110 ± 30 keV [Ade 77], 179 ± 75 keV [Lin 77], 250 keV [Bra 72] and 250-450 keV [Rei 70]. However, electromagnetic probe measurements are generally consistent and with the exception of Ritchie *et al.*, pion scattering measurements are consistent with electromagnetic probe measurements. The experimental values of $\mathcal{H}_{01}$ and β can be compared with those obtained in an experiment using electron scattering [Fla 79]. Theoretical values of $\mathcal{H}_{01}$ determined with different models are given in Table 5.5. The results from this experiment are in agreement within uncertainties with the electron scattering results for all models.

Model	$\beta(\gamma+(e,e'))$	$\mathcal{H}_{01}$ (keV)
CK (8-16) POT	.056(16)	134(66)
CK (8-16) 2BME	.054(15)	130(62)
CK (6-16) 2BME	.057(16)	136(66)
FULL $2\hbar\omega$ (MK)	.069(18)	165(74)
FULL $2\hbar\omega$ (G)	.059(16)	141(66)

Table 5.5: Values of $\mathcal{H}_{01}$ deduced from electron scattering data of Flanz *et al.* [Fla 79]. Various theoretical models are discussed in Flanz *at al.*

Chapter 6

Conclusion

Cross sections for the 1^+ doublet in ^{12}C excited by 50 MeV pions were found, and ratios of the cross sections were taken of these two states at 12.71 and 15.11 MeV for both incident beams of π^+ and π^-.

The cross section measurements were obtained using the Clamshell spectrometer, developed to have the capability of distinguishing these weakly excited states from nearby strongly excited states. The Clamshell's large solid angle combined with the LEP's short channel length make measurements with pions of this low energy possible. The resolution of the experiment was greatly improved by using the Scruncher, a super-conducting RF cavity designed to improve beam resolution while increasing beam flux.

The ratio of 12.71 MeV to 15.11 MeV cross sections for a π^+ incident beam was 6.9 ± 1.3, and for a π^- incident beam this ratio was found to be 3.9 ± 1.4. These values are in agreement with those previously determined by Jaki *et al.* [Jak 90] and in partial agreement with those determined by Ritchie *et al.* [Rit 90].

An experimental value for the isospin mixing matrix element, $\mathcal{H}_{01}$, was found to be 119 ± 40 keV, in good agreement with an average value of 123 ± 26 keV from previous pion scattering data. A formalism was developed where the ratio of $\pi^+ + p$ to $\pi^- + p$ cross sections, called χ, could be determined both experimentally and theoretically. The experimental value of χ was 2.60 ± 0.11 and the theoretical value was 2.85. This agreement suggests that the theory discussed successfully describes the pion-nucleon interaction and the structure of the states involved, and that the

impulse approximation is valid at 50 MeV.

The ^{12}C elastic, $0^+, 2^+$, and the 3^- cross sections were also measured and these cross sections were generally in agreement with theory and previous data, except for the 0^+ excitation. For this state, the cross sections for scattering by pions of both charges did not agreed with theory. This experiment was the first measure cross sections for excitation by π^- scattering for the 0^+ and 3^- states.

References

[Ade 77] F.G. Adelberger, *et al.*, Phys. Rev. **C15**, 484 (1977).

[Ajz 85] F. Ajzenburg-Selove, Nucl. Phys. **A433**, 1 (1985).

[Arn 85] R.A. Arndt and L.D. Roper, Program SAID.

[Bra 72] W.J. Braithwaite, *et al.*, Phys. Rev. Lett. **29**, 376 (1972).

[Car 81] J.A. Carr, *et al.*, scattering computer code ALLWRLD, unpublished.

[DeV 87] H. De Vries, *et al.*, Atom. Data & Nucl. Data Tables **36**, 495 (1987).

[Dyt 79] S.A. Dytman, *et al.*, Phys. Rev. **C19**, 971 (1979).

[Eis 80] J.M Eisenberg and D. Koltun, *Theory of Meson Interactions with Nuclei* (John Wiley and Sons Inc., New York, New York, 1980).

[Esc 89] J. Escalante, Ph. D. Thesis, University of South Carolina, 1989.

[Fla 79] J.B. Flanz, *et al.*, Phys. Rev. Lett. **43**, 1922 (1979).

[Gas 66] S. Gasiorowitz, *Elementary Particle Physics* (John Wiley and Sons Inc., New York, New York, 1966)

[Gri 87] D. Griffiths, *Introduction to Elementary Particles* (John Wiley and Sons Inc., New York, New York, 1987).

[Hey 90] K.L.G. Heyde, *The Nuclear Shell Model* (Springer-Verlag, New York, New York, 1990).

[Hik 92] K.Hikasa, *et al.*, Phys. Rev. **D45**, 1 (1992).

[Jak 90] J. Jaki, *et al.*, Phys. Lett. **B238**, 36 (1990).

[Kol 71] D. Koltun, *Advances in Nuclear Physics*, Vol. 3, eds. M. Baranger and E. Vogt (Plenum Press, New York, New York, 1971).

[Leo 87] W.R. Leo, *Techniques for Nuclear and Particle Physics Experiments* (Springer-Verlag, New York, New York, 1987).

[Lin 77] J.M. Lind, *et al.*, Nucl. Phys. **A276**, 25 (1977).

[LUH 84] LAMPF Users Handbook, Los Alamos National Laboratory Report MP-DO-3-UHB (Rev. 1984), unpublished.

[Mit 87] J.H. Mitchell, Ph. D. Thesis, University of Colorado, LA-10941-T, 1987.

[Mor 81] C.L. Morris, *et al.*, Phys. Lett. **99B**, 387 (1981).

[Mor 90] C.L. Morris, private communication, 1990.

[Mor 92] C.L. Morris, private communication, 1992.

[O'Do 92] J.M. O'Donnell, *et al.*, accepted for publication in Nuclear Instrumentation and Methods.

[Rit 88] B.G. Ritchie, *et al.*, Phys. Rev. **C37**, 1347 (1988).

[Rei 70] F.D. Reisman, *et al.*, Nucl. Phys. **A153**, 244 (1970).

[Rit 90] B.G. Ritchie, *et al.*, Phys. Rev. **C41**, 1668 (1990).

[Row 78] G. Rowe, *et al.*, Phys. Rev. **C18**, 584 (1978).

[Sob 84] R.J. Sobie, *et al.*, Phys. Rev. **C30**, 1612 (1984).

[SPS 89] SPSS/PC+^{TM} Update for V3.0 and V3.1 (SPSS Inc., Chicago, Illinois, 1989).

[Whi 89] C.S. Whisnant, *et al.*, Phys. Rev. **C35**, 1935 (1989).

APPENDIX A

DERIVATION OF $\mathcal{H}_{01}$

Appendix A

Derivation of $\mathcal{H}_{01}$

Equations 2.1 and 2.2 define two states $| A\rangle$ and $| B\rangle$ such that

$$| A\rangle = \alpha | 0\rangle + \beta | 1\rangle$$

and

$$| B\rangle = \alpha | 1\rangle - \beta | 0\rangle.$$

Manipulating these equations, $| 1\rangle$ can be expressed as

$$\frac{1}{\beta} | A\rangle - \frac{\alpha}{\beta} | 0\rangle = | 1\rangle \tag{A.1}$$

and

$$\frac{1}{\alpha} | B\rangle - \frac{\beta}{\alpha} | 0\rangle = | 1\rangle. \tag{A.2}$$

Subtracting Equation A.2 from Equation A.1 yields

$$\frac{1}{\beta} | A\rangle - \frac{1}{\alpha} | B\rangle - \frac{\alpha}{\beta} | 0\rangle - \frac{\beta}{\alpha} | 0\rangle = 0.$$

Multiply through by $\alpha\beta$, such that

$$\alpha | A\rangle - \beta | B\rangle - \alpha\beta(\frac{\alpha}{\beta} + \frac{\beta}{\alpha}) | 0\rangle = 0,$$

which can be simplified to

$$\alpha | A\rangle - \beta | B\rangle - (\alpha^2 + \beta^2) | 0\rangle.$$

Since $\alpha^2 + \beta^2 = 1$, $\mid 0\rangle$ can be expressed as

$$\mid 0\rangle = \alpha \mid A\rangle - \beta \mid B\rangle. \tag{A.3}$$

Inserting Equation A.3 into Equation A.1 yields

$$\frac{1}{\beta} \mid A\rangle - \frac{\alpha}{\beta}(\alpha \mid A\rangle - \beta \mid B\rangle) = \mid 1\rangle.$$

This expression can be simplified to

$$\frac{1-\alpha^2}{\beta} \mid A\rangle + \alpha \mid B\rangle = \mid 1\rangle.$$

Since $1 - \alpha^2 = \beta^2$,

$$\mid 1\rangle = \beta \mid A\rangle + \alpha \mid B\rangle. \tag{A.4}$$

As discussed in Chapter 2, the nuclear Hamiltonian, H_N, is made up of a charge-independent piece and a charge-dependent piece, such that $H_N = H_{CI} + H_{CD}$. The isospin mixing matrix element is $\mathcal{H}_{01} = \langle 0 \mid H_{CD} \mid 1\rangle$, and $H_{CD} = H_N - H_{CI}$. Therefore

$$\mathcal{H}_{01} = \langle 0 \mid H_N \mid 1\rangle - \langle 0 \mid H_{CI} \mid 1\rangle.$$

$\langle 0 \mid H_{CI} \mid 1\rangle = E_1\langle 0 \mid 1\rangle$, which is zero since $\mid 0\rangle$ and $\mid 1\rangle$ are orthogonal states. This leaves just the $\langle 0 \mid H_N \mid 1\rangle$ piece to consider. Substituting Equations A.3 and A.4 into $\langle 0 \mid H_N \mid 1\rangle$ yields

$$\mathcal{H}_{01} = (\alpha\langle A \mid -\beta\langle B \mid)H_N(\beta \mid A\rangle + \alpha \mid B\rangle).$$

Since $H_N \mid A\rangle = E_A \mid A\rangle$ and $H_N \mid B\rangle = E_B \mid B\rangle$,

$$\mathcal{H}_{01} = (\alpha\langle A \mid -\beta\langle B \mid)(\beta E_A \mid A\rangle + \alpha E_B \mid B\rangle).$$

Expanding this expression yields

$$\mathcal{H}_{01} = \alpha\beta E_A\langle A \mid A\rangle - \beta^2 E_A\langle B \mid A\rangle + \alpha^2 E_B\langle A \mid B\rangle) - \alpha\beta E_B\langle B \mid B\rangle.$$

$| A\rangle$ and $| B\rangle$ are orthogonal states, so $\langle A \mid A\rangle = \langle B \mid B\rangle = 1$ and $\langle A \mid B\rangle = \langle B \mid A\rangle = 0$. Therefore

$$\mathcal{H}_{01} = \alpha\beta E_A - \alpha\beta E_B,$$

which simplifies to

$$\mathcal{H}_{01} = \alpha\beta(E_A - E_B),$$

the expression given in Equation 2.8.

*U.S. GOVERNMENT PRINTING OFFICE: 1993-774-036/67088

END

DATE FILMED

5/25/93